Chapter 1

Introduction

1.1 Bulk metallic glasses and their composites

Metallic glass, by definition, is a type of non-crystalline (amorphous, disordered) metallic alloy lacking long-range periodicity of the atomic arrangement. This is a liquid alloy which is cooled below its thermodynamic melting point and then fails to crystallize, but solidifies nevertheless [1]. Consequently, the forming of metallic glasses can be realized by solidification of liquid alloys at cooling rates sufficiently high to suppress the nucleation and growth of competing crystalline phases. The first metallic glass was discovered by rapid quenching of Au-Si binary metallic melts at a very high cooling rate (approximately $10^6 K\ s^{-1}$) in the early 1960's at the California Institute of Technology by Duwez and his coworkers [2, 3].

The requirement for extremely high critical cooling rates to form the amorphous structure in the alloy limited the achievable size of the so-formed metallic glass. The metallic glasses developed early were in the forms of thin sheets or ribbons of micron size, and the engineering interest in them focused mainly on their electronic and magnetic properties [4-6]. To produce glasses in larger sizes which are practical for structural applications, efforts have been made in both improving the processing technology for higher achievable cooling rates and searching for good glass forming alloy systems with lower critical cooling rates.

Good glass forming alloy systems feature low eutectic points and large supercooled liquid regimes, which result in lower cooling rates to form metallic glasses with bulk sizes [7]. In the 1970's, Chen demonstrated the casting of mm diameter rods of Pd-Cu-Si alloys by means of a "suction casting" method and a relatively low cooling rate (1000K/s), which was the first achievement of pushing the size of cast metallic glass from the micron to millimeter range [8]. Spheres of Au-Pb-Sb glass of 1 mm diameter were produced by Lee *et al.* in 1982 with the technique of cooling the melts in a drop tower [9]. Using fluxing methods, Turnbull and coworkers reported the formation of ~1cm vitrified ingots of a Pd-Ni-P alloy at cooling rates below 100K/s [10, 11], that was when the phrase "bulk metallic glass" (BMG), i.e., amorphous alloy in bulk size, came into vogue. Recently, the development of BMGs is associated with the discovery of new good glass forming compositions such as La-Al-Ni [12], Mg-Cu-Y [13], Zr-Ni-Al-Cu [14], Zr-Ti-Cu-Ni-Be [15], and Cu-Zr-Ti-Ni [16]. The Zr-Ti-Cu-Ni-Be system (Vitreloy family) is among the best glass forming alloy systems discovered thus far. One extensively studied example of this glass family is $Zr_{41.2}Ti_{13.8}Cu_{12.5}Ni_{10}Be_{22.5}$ (at. %), i.e., Vitreloy 1, which has a critical cooling rate of 1 K/s and it can be cast in rods with a diameter of up to 5 cm [15]. In 1996, Johnson [1] summarized that nearly all the discovered bulk metallic glasses can be described as pseudo ternary alloys of the form $ETM_{1-x-y}LTM_xSM_y$, where ETM stands for to early transition metal or Lanthanide group metals such as Zr, Ti, Nb and La, LTM is an abbreviation for late transition metal such as Fe, Co, Ni and Cu, and SM refers to simple metal such as Al, Be, and Mg. Almost all good bulk metallic glasses formers have the following compositional and physical features in common [1, 7, 17, 18]: (i) a composition which favors deep eutectic behavior in the phase diagram; (ii) a reduced glass transition temperature (T_g/T_m) of around 2/3 or higher; (iii) a large supercooled liquid retime of more than 80 K upon heating; and finally, (iv) significant differences in atomic sizes among the main constituent elements. For example, $Zr_{41.2}Ti_{13.8}Cu_{12.5}Ni_{10}Be_{22.5}$ (Vitreloy 1), developed by Peker and Johnson, has a low melting point of $T_m = 937K$, a T_g/T_m ratio of 0.67 ($T_g = 625K$), a supercooled liquid region of 80 K, and atomic size difference between Zr and Be of 30% [15].

The availability of metallic glasses in bulk size made them structurally useful (with the alternative name structural amorphous metals, i.e., SAMs) and generated much interest in studying the mechanical properties of this new family of materials. The new BMGs exhibited mechanical properties featuring both their metallic origin and glassy root, with promising trends such as high strength, large elastic region, and good resistance to fatigue as well as the drawbacks of limited room temperature ductility like other glasses [19-21]. The lack of ductility in metallic glasses under uniaxial compression/tension is due to strain localization in a narrow shear band resulting in catastrophic failure once the metallic glass reaches its yield point. To improve the performance of BMGs for structural applications, it thus became desirable to develop metallic glass composites which obtain enhanced room temperature ductility without sacrificing too much of their high strength.

Early efforts in fabricating metallic glass composites included the use of amorphous metal ribbons as reinforcement in polymer or glass ceramic matrix [22-24], adding ceramic particles or fibers to metallic glass ribbons produced by the melt spinning technique [25], and reinforcing the bulk metallic glass matrix with ductile metal or ceramic particles or wires [26-30]. The mechanical properties of metallic glass composites were improved because of the existence of additional phases, which facilitated the formation of multiple shear bands during deformation, thus enhancing the macroscopic plasticity of the composites [31, 32]. However, the second phase introduced in the amorphous matrix also caused problems such as debonding between the constituent phases and, consequently, poor fatigue resistance [31].

In the competition between the crystallization and the glass formation processes when a liquid at above its melting temperature is cooled to the solid stte, sometimes neither wins and there results a coexistence of dual phases, i.e., crystalline particles or clusters of varying sizes and shapes embedded in an amorphous matrix. Such partial crystallization phenomenon led to the discovery of *in-situ* ductile metallic glass composites. Among them, the one that exhibited the best processibility and mechanical properties is a zirconium based BMG composite pioneered at Caltech in 2000 by Johnson and coworkers [33]. By introducing five atomic percent (5 at. %) of niobium in the place of copper in Vitreloy 1and processing with the same arc-melting and quenching procedures, a secondary bcc crystalline dendritic β-phase was formed and stabilized in the amorphous matrix [33, 34]. The β-Vitreloy composite (also known as β-Vit) developed by

Hays *et al.* was found to have the chemical composition of $Zr_{71}Ti_{16.3}Nb_{10}Cu_{1.8}Ni_{0.9}$ (atomic percentage, at. %) in the crystalline dendrite phase, and the amorphous matrix phase was determined to have a chemical composition of $Zr_{47}Ti_{12.9}Nb_{2.8}Cu_{11}Ni_{9.6}Be_{16.7}$ (at. %) with an estimated 25% volume fraction of the dendritic β-phase [33]. The chemical composition of the amorphous matrix is close to that of Vitreloy 1, though not exactly the same [15].

With more than 40 years of scientific and engineering exploration of developing good and reliable glass forming alloys, over 30 BMG and composite families have been discovered so far [35]. Mature processing techniques and availability of good alloys provided a wide space to systematically study the physical, mechanical, and thermodynamical properties of BMGs and BMG composites to generate criteria and laws to describe their deformation mechanisms, to predict deformation and failure under different loading conditions, and to guide future alloy development and applications of metallic glasses. Some early work illustrating the various aspects is reviewed in section 1.2.

1.2 Mechanical and thermal properties of BMGs and their composites

Like in other amorphous materials such as polymers [36], an important phenomenon that occurs in metallic glass when the liquid is undercooled or undergoes configurational freezing to a solid is the glass transition. It is accompanied by a dramatic increase in viscosity and a drastic drop in atomic mobility, while the material changes from a more rubber like state to a more solid "glassy" state. The onset temperature when the "glassy" to "rubbery" transition starts is defined as the glass transition temperature, even though the glass transition is a kinetic process which occurs over a temperature range depending on the heating or cooling rate, rather than at a well-defined temperature. Chen and Turnbull were the first ones to report the observation of glass transition in metallic glass [37]. Since the glass transition is considered to be associated with so called "free volume" change in general amorphous materials [38], the free volume concept was also adopted and related to the glass transition in metallic glasses [39], which will be discussed in detail later. The temperature range between the glass transition temperature and the crystallization temperature is called the "super-cooled liquid regime" of an amorphous alloy, and the alloy at this temperature range is in its super-cooled liquid state. The glass transition temperature is not only an important thermodynamics parameter but also has an important effect on the deformation mechanisms of BMGs and their composites.

It has been found that the deformation of metallic glasses is very sensitive to testing temperatures and strain rates, especially when the temperature is close or above the glass transition temperature. Based on the extensive results for a wide range of alloys including Zr- based alloys [40-43] , La- based alloys [41, 44], Fe- based alloys [45, 46], and Pd- based alloys [46, 47], the deformation modes of BMGs fall into three distinctly different categories. They are: (i) at room temperature and high strain rate, BMGs deform and fail with shear localization mode, with limited plasticity and brittle failure; (ii) at moderate temperature (in the vicinity of the glass transition temperature) and intermediate strain rate, BMGs exhibit extended ductility through viscous flow with non-constant viscosity, which is referred to as the non-Newtonian flow mode. This mode features stress over- and under-shooting before the flow reaches steady state; in a stress-strain curve, stress overshooting occurs when the peak stress exceed the steady state stress, and the undershooting is the part where the stress is below the steady state value during a loading process, (iii) at even higher temperature (in the supercooled regime) and low strain rate, the viscous flow of BMGs becomes Newtonian, and the flow stress reaches a steady state right after yielding upon loading [42]. The first mode (shear localization) is an inhomogeneous flow mode and the last two (non Newtonian and Newtonian) are generally regarded as homogeneous flow modes. The deformation of BMG composites, especially in the high temperature range, has not been systematically characterized previously. Mechanical tests performed at room temperature on the newly developed β-Vit material [32, 33, 48, 49] showed enhanced ductility of about 5~6% more than its amorphous matrix, which could be attributed to the formation of multiple shear bands initiated and arrested by the crystalline dendrites.

There exist a number of theories to describe the deformation mechanism of metallic glasses. Argon and coworkers developed a model based on the idealization of two deformation modes, namely the diffuse shear transformation and the dislocation loop formation, to analyze the boundary between homogeneous and inhomogeneous flow of Pd-Si metallic glass [50-52]. Spaepen and coworkers proposed a free volume model that has been widely used, which relates the mechanical stress to the concentration of free volume in the material [53]. Khonik suggested a directional structural relaxation model, which states that each rearrangement event can be interpreted as a thermally activated shear due to local atomic structures resulting in nearly athermal viscous flow by external stress [54, 55].

Even though the free volume model and the related theories are valuable in demonstrating the physics of the deformation mechanism of BMGs, the direct measurement of free volume is not available yet. Previous study also showed the model was not capable of quantitatively capturing the flow behavior of BMGs [42]. Outside of the framework of free volume models, Langer *et al*. proposed a shear-transformation-zone model that describes the deformation of metallic glasses with a set of equations of motion analogous to the Navier-Stokes equation of fluid dynamics [56], which include those describing the evolution of the shear-transform-zone density, the deformation rate and the stress equilibrium, with an effective disorder temperature taken as the dynamic state variable. Recently, Johnson and Samwer [35] adopted the concepts of the potential energy landscape and inherent states from Stillinger [57] and proposed a cooperative shear model (CSM) as a simple scaling law to predict the temperature dependent critical shear stress of bulk metallic glasses. The CSM could be used to derive the macroscopic variables of bulk metallic glasses, such as shear viscosity and shear modulus, from the configurational energy of the atom clusters. Change in the thermodynamic state of the amorphous material will induce change in shear moduli and viscosities, which can be experimentally determined. Therefore, it is more feasible to design experiments to testify the validation of the cooperative shear model.

To testify all those models, it requires experimental data over a wide range of strain rates and temperatures. In particular, investigations on the deformation behavior of the BMGs and their composites in their supercooled liquid regions and the consequent microstructural changes would provide insight on the fundamental mechanisms and scaling laws that determine the distinct modes of the deformation.

1.3 Motivation and outline

The physical and mechanical properties of BMGs are closely related to their unique amorphous structure. Fully understanding the deformation mechanisms of BMGs and their composites requires investigation of the microstructural changes and their interaction with the mechanical behavior. The complexity of this problem lies in multiple levels. The rheology of the supercooled liquid is governed by atomic diffusion and relaxation processes in the glass. The mechanical loading under various conditions might also affect the amorphous structure and cause decomposition or nanocrystallization in the material, which could in turn change the mechanical response. In case of the composites, the stability, volume fraction, size, and shape of the crystalline inclusions should all be taken into consideration when the strengthening effect of the dendrites are studied.

The objectives of this dissertation are to explore the deformation mechanisms of a series of Vitreloy glasses and composites in depth over a wide range of strain rates and temperatures, with a focus on their supercooled liquid region. The studies were performed by combining uniaxial mechanical testing and microscopic characterization, to examine various theories of deformation of metallic glasses with experimental data and to provide models for predicting the overall mechanical performance of the BMG composites and guide future processing techniques.

Two bulk metallic glasses, Vitreloy 1 and Vitreloy 4, are chosen for study in Chapter 2. The different modes of atomic disordering upon mechanical loading in their supercooled liquid regions are investigated. Uniaxial compression tests are performed on the two alloys at a single temperature in their supercooled liquid regions and at various strain rates, followed by DSC examination. The influence of the structural changes on the mechanical behavior of the two materials is further investigated by jump-in-strain-rate tests, performed in both the non-Newtonian and Newtonian flow regions, as well as drops in strain rates from the non-Newtonian to the Newtonian flow region.

In Chapter 3, uniaxial compression tests are conducted on a newly developed Zr- based alloy at various temperatures in its supercooled liquid region and at different strain rates. A deformation map for the alloy is constructed, and the Newtonian and non-Newtonian viscosities are computed and fit with the recently developed Cooperative Shear Model (CSM) in a self-consistent manner. Acoustic (shear) wave speed measurements are performed on deformed and quenched specimens to obtain the shear modulus of the stressed material. This is the first experimental work that has adapted CSM as the underling physical mechanism accounting for the change of the thermodynamical and mechanical properties of metallic glasses. The results show that CSM is a viable and promising model that links the atomic configuration of the amorphous material to their macroscopic properties.

In Chapter 4, the plastic flow behavior of a bulk metallic glass *in-situ* composite β-Vit is investigated under uniaxial compression in the supercooled liquid regime and at various strain rates ($10^{-4} \sim 10^{-1} s^{-1}$). The *in-situ* composite contains $\sim 25\%$ volume fraction of crystalline β-phase dendrites (Zr-Ti-Nb rich) embedded in the amorphous matrix whose composition is close to that of the amorphous Vitreloy 1. The composite exhibits superplastic behavior like the amorphous Vitreloy 1 did. Significant strain hardening, which can be attributed to the coalescence of the dendrites, is observed when the material is deformed at high temperatures and low strain rates. A dual-phase composite model is employed in finite element numerical simulations to understand this hardening mechanism.

A brief summary of the dissertation and suggestions for future work are given in Chapter 5.

Reference

[1] W. L. Johnson, "Bulk metallic glasses - A new engineering material," *Current Opinion in Solid State & Materials Science*, **1**, 383-386 (1996).

[2] P. Duwez and R. H. Willens, "Rapid Quenching of Liquid Alloys," *Transactions of the Metallurgical Society of Aime*, **227**, 362-& (1963).

[3] W. Klement, R. H. Willens, and P. Duwez, "Non-Crystalline Structure in Solidified Gold-Silicon Alloys," *Nature*, **187**, 869-870 (1960).

[4] B. S. Berry and W. C. Pritchet, "Magnetic Annealing and Directional Ordering of an Amorphous Ferromagnetic Alloy," *Physical Review Letters*, **34**, 1022-1025 (1975).

[5] H. S. Chen, S. D. Ferris, E. M. Gyorgy, H. J. Leamy, and R. C. Sherwood, "Field Heat-Treatment of Ferromagnetic Metallic Glasses," *Applied Physics Letters*, **26**, 405-406 (1975).

[6] H. J. Leamy, S. D. Ferris, G. Norman, D. C. Joy, R. C. Sherwood, E. M. Gyorgy, and H. S. Chen, "Ferromagnetic Domain-Structure of Metallic Glasses," *Applied Physics Letters*, **26**, 259-260 (1975).

[7] W. L. Johnson, "Metastable Phases," *Intermetallic Compounds*, J. H. Westbrook, Fleischer, R.L., Ed. New York: Wiley, **1**, 687-709 (1994).

[8] H. S. Chen, "Thermodynamic Considerations on Formation and Stability of Metallic Glasses," *Acta Metallurgica*, **22**, 1505-1511 (1974).

[9] M. C. Lee, J. M. Kendall, and W. L. Johnson, "Spheres of the Metallic Glass $Au_{55}Pb_{22.5}Sb_{22.5}$ and Their Surface Characteristics," *Applied Physics Letters*, **40**, 382-384 (1982).

[10] A. J. Drehman, A. L. Greer, and D. Turnbull, "Bulk Formation of a Metallic-Glass Pd_{40} $Ni_{40}P_{20}$," *Applied Physics Letters*, **41**, 716-717 (1982).

[11] H. W. Kui, A. L. Greer, and D. Turnbull, "Formation of Bulk Metallic-Glass by Fluxing," *Applied Physics Letters*, **45**, 615-616 (1984).

[12] A. Inoue, T. Zhang, and T. Masumoto, "Production of Amorphous Cylinder and Sheet of $La_{55}Al_{25}Ni_{20}$ Alloy by a Metallic Mold Casting Method," *Materials Transactions Jim*, **31**, 425-428 (1990).

[13] A. Inoue, A. Kato, T. Zhang, S. G. Kim, and T. Masumoto, "Mg-Cu-Y Amorphous-Alloys with High Mechanical Strengths Produced by a Metallic Mold Casting Method," *Materials Transactions Jim*, **32**, 609-616 (1991).

[14] T. Zhang, A. Inoue, and T. Masumoto, "Amorphous Zr-Al-Tm (Tm = Co, Ni, Cu) Alloys with Significant Supercooled Liquid Region of over 100-K," *Materials Transactions Jim*, **32**, 1005-1010 (1991).

[15] A. Peker and W. L. Johnson, "A Highly Processable Metallic Glass - $Zr_{41.2}Ti_{13.8}Cu_{12.5}Ni_{10.0}Be_{22.5}$," *Applied Physics Letters*, **63**, 2342-2344 (1993).

[16] X. H. Lin and W. L. Johnson, "Formation of Ti-Zr-Cu-Ni Bulk Metallic Glasses," *Journal of Applied Physics*, **78**, 6514-6519 (1995).

[17] M. H. Cohen and D. Turnbull, "Composition Requirements for Glass Formation in Metallic and Ionic Systems," *Nature*, **189**, 131-& (1961).

[18] D. Turnbull and M. H. Cohen, "Concerning Reconstructive Transformation and Formation of Glass," *Journal of Chemical Physics*, **29**, 1049-1054 (1958).

[19] H. A. Bruck, T. Christman, A. J. Rosakis, and W. L. Johnson, "Quasi-Static Constitutive Behavior of $Zr_{41.2}Ti_{13.8}Cu_{12.5}Ni_{10.0}Be_{22.5}$ Bulk Amorphous-Alloys," *Scripta Metallurgica Et Materialia*, **30**, 429-434 (1994).

[20] H. A. Bruck, A. J. Rosakis, and W. L. Johnson, "The dynamic compressive behavior of beryllium bearing bulk metallic glasses," *Journal of Materials Research*, **11**, 503-511 (1996).

[21] W. L. Johnson, "Fundamental aspects of bulk metallic glass formation in multicomponent alloys," *Metastable, Mechanically Alloyed and Nanocrystalline Materials, Pts 1 and 2*, **225**, 35-49 (1996).

[22] R. U. Vaidya and K. N. Subramanian, "Metallic-Glass Ribbon-Reinforced Glass-Ceramic Matrix Composites," *Journal of Materials Science*, **25**, 3291-3296 (1990).

[23] R. U. Vaidya and K. N. Subramanian, "Toughening in Metallic-Glass Ribbon Reinforced Glass-Ceramic Matrix Composites," *Sampe Journal*, **29**, 26-30 (1993).

[24] S. J. Cytron, "A Metallic Glass-Metal Matrix Composite," *Journal of Materials Science Letters*, **1**, 211-213 (1982).

[25] P. G. Zielinski and D. G. Ast, "Preparation of Rapidly Solidified Ribbons with 2nd Phase Particles," *Journal of Materials Science Letters*, **2**, 495-498 (1983).

[26] H. Kato, T. Hirano, A. Matsuo, Y. Kawamura, and A. Inoue, "High strength and good ductility of $Zr_{55}Al_{10}Ni_5Cu_{30}$ bulk glass containing ZRC particles," *Scripta Materialia*, **43**, 503-507 (2000).

[27] C. P. Kim, R. Busch, A. Masuhr, H. Choi-Yim, and W. L. Johnson, "Processing of carbon-fiber-reinforced $Zr_{41.2}Ti_{13.8}Cu_{12.5}Ni_{10.0}Be_{22.5}$ bulk metallic glass composites," *Applied Physics Letters*, **79**, 1456-1458 (2001).

[28] H. Choi-Yim, R. D. Conner, F. Szuecs, and W. L. Johnson, "Processing, microstructure and properties of ductile metal particulate reinforced $Zr_{57}Nb_5Al_{10}Cu_{15.4}Ni_{12.6}$ bulk metallic glass composites," *Acta Materialia*, **50**, 2737-2745 (2002).

[29] H. Choi-Yim, R. Busch, U. Koster, and W. L. Johnson, "Synthesis and characterization of particulate reinforced $Zr_{57}Nb_5Al_{10}Cu_{15.4}Ni_{12.6}$ bulk metallic glass composites," *Acta Materialia*, **47**, 2455-2462 (1999).

[30] H. Choi-Yim and W. L. Johnson, "Bulk metallic glass matrix composites," *Applied Physics Letters*, **71**, 3808-3810 (1997).

[31] K. M. Flores, W. L. Johnson, and R. H. Dauskardt, "Fracture and fatigue behavior of a Zr-Ti-Nb ductile phase reinforced bulk metallic glass matrix composite," *Scripta Materialia*, **49**, 1181-1187 (2003).

[32] R. D. Conner, H. Choi-Yim, and W. L. Johnson, "Mechanical properties of $Zr_{57}Nb_5Al_{10}Cu_{15.4}Ni_{12.6}$ metallic glass matrix particulate composites," *Journal of Materials Research*, **14**, 3292-3297 (1999).

[33] C. C. Hays, C. P. Kim, and W. L. Johnson, "Microstructure controlled shear band pattern formation and enhanced plasticity of bulk metallic glasses containing in situ formed ductile phase dendrite dispersions," *Physical Review Letters*, **84**, 2901-2904 (2000).

[34] C. C. Hays, C. P. Kim, and W. L. Johnson, "Enhanced plasticity of bulk metallic glasses containing ductile phase dendrite dispersions," *Metastable, Mechanically Alloyed and Nanocrystalline Materials, Pts 1 and 2*, **343-3**, 191-196 (2000).

[35] W. L. Johnson and K. Samwer, "A universal criterion for plastic yielding of metallic glasses with a (T/T-g)$^{(2/3)}$ temperature dependence," *Physical Review Letters*, **95**, 195501 (2005).

[36] S. Matsuka, *Relaxation phenomena in polymers*. New York: Oxford University Press, (1992).

[37] H. S. Chen and D. Turnbull, "Thermal properties of gold-silicon binary alloy near eutectic composition," *Journal of applied physics*, **38**, 3646 (1967).

[38] D. Turnbull and M. H. Cohen, "Free-volume model of amorphous phase- Glass transition," *Journal of Chemical Physics*, **34**, 120 (1961).

[39] M. H. Cohen and G. S. Grest, "Liquid-glass transition, a free-volume model approach," *Physical Review B*, **20**, 1077-1098 (1979).

[40] T. G. Nieh, J. Wadsworth, C. T. Liu, T. Ohkubo, and Y. Hirotsu, "Plasticity and structural instability in a bulk metallic glass deformed in the supercooled liquid region," *Acta Materialia*, **49**, 2887-2896 (2001).

[41] T. G. Nieh, C. Schuh, J. Wadsworth, and Y. Li, "Strain rate-dependent deformation in bulk metallic glasses," *Intermetallics*, **10**, 1177-1182 (2002).

[42] J. Lu, G. Ravichandran, and W. L. Johnson, "Deformation behavior of the $Zr_{41.2}Ti_{13.8}CU_{12.5}Ni_{10}Be_{22.5}$ bulk metallic glass over a wide range of strain-rates and temperatures," *Acta Materialia*, **51**, 3429-3443 (2003).

[43] Y. Kawamura, T. Shibata, A. Inoue, and T. Masumoto, "Deformation behavior of $Zr_{65}Al_{10}Ni_{10}Cu_{15}$ glassy alloy with wide supercooled liquid region," *Applied Physics Letters*, **69**, 1208-1210 (1996).

[44] B. van Aken, P. de Hey, and J. Sietsma, "Structural relaxation and plastic flow in amorphous $La_{50}Al_{25}Ni_{25}$," *Materials Science and Engineering a-Structural Materials Properties Microstructure and Processing*, **278**, 247-254 (2000).

[45] D. Lee, "Localized Vs Homogeneous Deformation in $Fe_{82}B1_{5}Si_{3}$ Amorphous Alloy," *Metallurgical Transactions a-Physical Metallurgy and Materials Science*, **12**, d419-424 (1981).

[46] Y. Kawamura, T. Nakamura, and A. Inoue, "Superplasticity in $Pd_{40}Ni_{40}P_{20}$ metallic glass," *Scripta Materialia*, **39**, 301-306 (1998).

[47] P. de Hey, J. Sietsma, and A. Van den Beukel, "Structural disordering in amorphous $Pd_{40}Ni_{40}P_{20}$ induced by high temperature deformation," *Acta Materialia*, **46**, 5873-5882 (1998).

[48] C. C. Hays, C. P. Kim, and W. L. Johnson, "Improved mechanical behavior of bulk metallic glasses containing in situ formed ductile phase dendrite dispersions," *Materials Science and Engineering a-Structural Materials Properties Microstructure and Processing*, **304**, 650-655 (2001).

[49] J. C. Lee, Y. C. Kim, J. P. Ahn, and H. S. Kim, "Enhanced plasticity in a bulk amorphous matrix composite: macroscopic and microscopic viewpoint studies," *Acta Materialia*, **53**, 129-139 (2005).

[50] A. S. Argon, "Plastic-Deformation in Metallic Glasses," *Acta Metallurgica*, **27**, 47-58, (1979).

[51] A. S. Argon and L. T. Shi, "Development of Visco-Plastic Deformation in Metallic Glasses," *Acta Metallurgica*, **31**, 499-507 (1983).

[52] J. Megusar, A. S. Argon, and N. J. Grant, "Plastic-Flow and Fracture in $Pd_{80}Si_{20}$ near Tg," *Materials Science and Engineering*, **38**, 63-72 (1979).

[53] F. Spaepen and D. Turnbull, "Mechanism for Flow and Fracture of Metallic Glasses," *Scripta Metallurgica*, **8**, 563-568 (1974).

[54] V. A. Khonik, "The kinetics of irreversible structural relaxation and homogeneous plastic flow of metallic glasses," *Physica Status Solidi a-Applied Research*, **177**, 173-189 (2000).

[55] V. A. Khonik, "Mechanical relaxations in metallic glasses," *Mechanical Spectroscopy Ii, Proceedings*, **89**, 67-92 (2003).

[56] J. S. Langer and L. Pechenik, "Dynamics of shear-transformation zones in amorphous plasticity: Energetic constraints in a minimal theory," *Physical Review E*, **68**, 061504 (2003).

[57] F. H. Stillinger, "A Topographic View of Supercooled Liquids and Glass-Formation," *Science*, **267**, 1935-1939 (1995).

Chapter 2

Deformation Mechanisms of Zr- Based Amorphous Alloys in Supercooled Liquid State

Abstract

Deformation of bulk metallic glasses (BMGs) in supercooled liquid state is a complex problem since it is associated with the structural relaxation of the materials induced by both thermal and mechanical processes. The purpose of this study is to experimentally investigate the interaction of inelastic deformation and microstructural changes such as decomposition and nanocrystallization of two Zr-based amorphous alloys. High temperature uniaxial compression tests were used to investigate the deformation mechanisms of BMGs in supercooled liquid state. Compression tests were performed on the two Zr-alloys at a single temperature in their supercooled liquid regime at various strain rates, followed by characterization using differential scanning calorimetry (DSC). Two distinct modes of atomic disordering in the two alloys induced by mechanical stress were discovered. In Vitreloy 1, phase separation and nanocrystallization dominated during the plastic deformation at high temperature. In Vitreloy 4, no evidence of crystallization was found, but DSC showed active decomposition and change in free volume due to coupled thermo-mechanical effects. The influence of the structural changes on the mechanical behavior of the two materials was further investigated by jump-in-strain-rate tests performed in both the non-Newtonian and Newtonian flow regions as well as drop-in-strain-rate from non-Newtonian to Newtonian flow region. It was found that the Vitreloy 4 possessed considerable stress softening after the strain rate drop.

Keywords: Bulk metallic glasses; Glass transition; Supercooled liquid; Newtonian and non-Newtonian flow; Phase separation; Crystallization; Decomposition; Softening

2.1 Introduction

Bulk metallic glasses, which are produced by rapid quenching of favorable alloy melts to suppress the nucleation of crystallites during cooling [1, 2], have been studied extensively in recent years due to their unique thermal and mechanical properties [3, 4]. The amorphous structure in BMGs is in a metastable state at room temperature, and its evolution towards the equilibrium phase is suppressed by a high kinetic barrier such that the metastable phase appears "stable" at room temperature for any practical timescale, i.e., the structure is frozen [5]. The process of evolution of the metastable phase towards equilibrium is generally referred to as structural relaxation [6]. Structural relaxation is inevitable for a non-equilibrium system such as metallic glasses or other amorphous materials. It has a significant influence on physical properties such as mechanical strength [7], magnetic susceptibility [8], electrical receptivity [9], and others. For potential application of BMGs as structural materials, the mechanical properties of metallic glasses and how they interact with the microstructural changes in the material are of significant interest. Both thermal and mechanical processes can accelerate the structural relaxation or even trigger phase changes in the amorphous structure [10]. Therefore, the deformation mechanism of amorphous alloys at high temperatures, especially in their super cooled liquid regimes where deformation is viscous in nature, becomes extremely complicated. The microstructural changes due to coupled thermo-mechanical effects during deformation can affect the mechanical response of the material. One of the critical parameters in determining the deformation characteristics of BMGs is the time rate of the strain or deformation, since the time history in viscous flow plays an important role on the structural relaxation process.

A flow map of most metallic glasses can be experimentally constructed via constant strain rate deformation at different temperatures and strain rates. Based on extensive results for a wide range of metallic glasses including Zr- based alloys [11-14] , La- based alloys [12, 15], Fe- based alloys [16, 17], and Pd- based alloys [17, 18], the deformation modes fall into three distinctly different categories. They are: (i) at room temperature and high strain rate, BMGs deform and fail by a shear localization mode, which features limited plasticity accumulated in localized thin shear bands with the material failing in a brittle manner; (ii) at some moderate temperature (in the vicinity of the glass transition temperature) and intermediate strain rate, BMGs exhibit extended ductility through viscous flow with non-linear viscosity, which is referred to as the non-Newtonian flow mode. This mode features stress over- and under-shooting, namely a peak stress higher than the steady state stress followed by a stress minima that is lower than the steady state stress; (iii) at even higher temperature (above glass transition temperature and below crystallization temperature, i.e., in the supercooled liquid regime) and lower strain rate, the viscous flow of BMGs becomes Newtonian. Upon loading, the flow stress reaches the steady state right after yielding starts [13]. The first mode (shear localization) is an inhomogeneous flow mode, and the last two (non Newtonian and Newtonian) are homogeneous flow modes. Most studies on structural relaxation are focused on the homogeneous flow region.

There exist a number of theories to describe the deformation mechanism of metallic glasses. Argon and coworkers developed a model based on the idealization of two deformation modes, namely the diffuse shear transformation and the dislocation loop formation, to analyze the boundary between homogeneous and inhomogeneous flow of a Pd-Si metallic glass [19-21]. Spaepen and coworkers proposed a free volume model that has been widely used which relates the mechanical stress to the concentration of free volume in the material [22-24]. Duine used the free volume based viscosity and defect evolution assumption by Spaepen to analyze the kinetic process of defects and their steady state concentration [25]. de Hey *et al*. applied the same idea to temperature induced structural evolution of some metallic glasses, leading to the conclusion that additional free volume is created as compared with thermal equilibrium due to plastic deformation [15, 18, 26]. Khonik suggested a directional structural relaxation model, which states that each rearrangement event can be interpreted as a thermally activated shear due to local atomic structures resulting in nearly athermal viscous flow by external stress [27, 28]. Outside of the framework of free volume model, Langer *et al*. proposed a shear-transformation-zone model that describes the deformation of metallic glasses with a set of equations of motion analogous to the Navier-Stokes equation of fluid dynamics [29]. The equations of motion include those describing the evolution of the shear-transformation-zone density, the deformation rate, and the stress equilibrium. In this model, an effective disorder temperature is taken as the dynamic state variable. Recently, Johnson and Samwer [30] adopted the concepts of potential energy landscape and inherent states from Stillinger [31] and proposed a cooperative shear model (CSM) in the form of a simple scaling law to predict the temperature dependent critical shear stress of bulk metallic glasses. The application of CSM in understanding the viscous flow of metallic glasses will be discussed at length in Chapter 3.

The recent developments in technology have provided advanced tools to experimentally study the complicated phenomena associated with structural relaxation at the microstructural level. Decomposition and crystallization at the nanometer scale were discovered to be two interesting aspects of the structural changes in the amorphous alloys. There have been extensive investigations using various experimental tools to study the effect of thermal history such as annealing or aging on crystallization in BMGs. Waniuk *et al.* studied a series of bulk Zr-Ti-Ni-Cu-Be amorphous alloys using DSC and X-ray diffraction to understand how changes in isothermal annealing temperature and annealing time affected the volume fraction of crystallization and shift in glass transition temperature, T_g [32]. Transmission electron microscopy and small-angle neutron scattering techniques were applied to study in detail the crystallite microstructure formed in Zr- based BMGs during annealing [33].

Along with the thermal effect, mechanically induced phase disordering and transformation is another important aspect in the deformation of metallic glasses. However, the fundamental mechanism of strain induced disordering is still under debate. Wright *et al.* [34] predicted free volume accumulation and void formation in the shear bands within the framework of the free volume model proposed by Spaepen [23]. Li *et al.* observed nanometer-scale defects in shear bands using high resolution transmission electron microscopy [35]. After Chen *et al.* [36] first reported the formation of nanocrystallites in the shear bands of amorphous Al- based alloys observed with transmission electron microscopy, there has been much experimental evidence for nano-scale crystallites formed in the vicinity of shear bands, fracture surfaces, nano-indentation, and in tensile and bending tests at room temperature or below [37-39]. In the homogeneous flow region, de Hey *et al.* further associated the glass transition behavior in the DSC trace of the deformed specimen with the amount of free volume and used it to explain the deformation behavior of Pd- and La- based alloys [18, 25, 26]. Heggen *et al.* used compression creep testing at constant stress and during jump stress to study the structural relaxation and disordering during the high temperature deformation of a Pd-Ni-Cu-P alloy [40, 41]. Based on Spaepen's free volume model, the activation volume of the process was computed with data at different temperatures and stress levels [23]. Nieh *et al.* [42] suggested nanocrystallization in the amorphous structure during the homogeneous deformation based on X-ray diffraction [43] and transmission electron microscopic [11] examinations of the superplastically deformed specimens. In some cases, spinodal decomposition or phase separation was suspected to precede nanocrystallization [44-46].

The deformation mechanisms of amorphous alloys are thus associated with structural changes which are affected by both thermal and mechanical effects. Spaepen's free volume model [23] provided expressions for flow stress and strain rate as a function of defect concentration and temperature. Kato *et al.* adopted a fictive stress model which modified the relaxation time in a simple Maxwell relaxation model with the concept of "fictive stress" [47, 48] and simulated the experimental data on a Pd-Ni-Cu-P glass fairly well [49]. In the case of isolated or aggregate nanocrystals in an amorphous structure, Nieh *et al.* [11, 50] proposed a mixed phase model that approximates the deformation rate depending on the volume fraction of crystallization and the order of crystallite concentration.

The purpose of this study is to experimentally investigate the interaction of inelastic (plastic) deformation and the microstructural changes such as decomposition and nanocrystallization of two Zr-based amorphous alloys using high temperature compression tests and to further understand the fundamental deformation mechanisms of the BMGs in their supercooled liquid regions.

Two structural amorphous alloys, $Zr_{41.25}Ti_{13.75}Cu_{12.5}Ni_{10}Be_{22.5}$ (Vitreloy 1™) and $Zr_{46.75}Ti_{8.25}Cu_{7.5}Ni_{10}Be_{27.5}$ (Vitreloy 4™), were chosen for this study. Though both materials have similar glass forming ability and mechanical properties, they exhibit distinctly different thermal properties as shown by their DSC traces. One of the characteristics of the DSC curve of Vitreloy 1 (with heating rate of 20 $K \cdot min^{-1}$) is that the crystallization event occurs in two steps: an initial portion (which is referred to as a spinode) indicating phase separation before primary crystallization, followed by the primary crystallization. This feature is not found in the DSC curve of Vitreloy 4. Instead, it exhibits two clearly separated crystallization events, with a smaller event following the major one. Among the best glass forming alloys and BMGs with most promising structural application, the two Vitreloy alloys have been well studied in both their mechanical and thermal properties. After Vitreloy 1 was first discovered in 1993 at Caltech [3], extensive studies have been carried out to reveal the thermodynamic and rheological properties of the material [45, 51]. The deformation behavior of Vitreloy 1 across a wide range of temperatures and strain rates has been studied by Lu *et al.* using compression testing [13]. The viscosity of Vitreloy 4 over the range between 10^5 and $10^9 \, Pa \cdot s$ has been measured by Busch *et al.* using parallel plate rheometry and three-point beam bending [52]. Previous research on the crystallization and decomposition behaviors of these two alloys and alloys of similar composition mostly focused on the thermal effects. However, there have not been any studies on the mechanical properties of Vitreloy 4, and little is known about the interplay between the microstructural changes and the mechanical properties of the two alloys, which seems important in understanding the deformation mechanisms for the purpose of analyzing and designing thermomechanical processes and structural applications of these materials.

Uniaxial compression tests were performed on the two alloys at a fixed temperature in their supercooled liquid region at various strain rates, followed by characterization using DSC. Two distinct modes of atomic disordering in the two alloys induced by stress were discovered. In Vitreloy 1, phase separation and nanocrystallization dominated during the inelastic deformation at high temperature. In Vitreloy 4, no evidence of crystallization was found, but DSC showed active decomposition and change in the amount of free volume due to coupled thermomechanical effects. The influence of the structural change on the mechanical behavior of the two amorphous alloys is studied using jump-in-strain-rate tests, performed independently in their non-Newtonian and Newtonian flow regions, and drop-in-strain-rate from non-Newtonian to Newtonian flow region. It was found that Vitreloy 4 has more pronounced stress softening after the rate drop.

2.2 Experimental

2.2.1 Material and specimen preparation

The bulk metallic glasses $Zr_{41.25}Ti_{13.75}Cu_{12.5}Ni_{10}Be_{22.5}$ (Vitreloy 1) and $Zr_{46.75}Ti_{8.25}Cu_{7.5}Ni_{10}Be_{27.5}$ (Vitreloy 4) were originally developed in the Keck Materials Research Laboratories at the California Institute of Technology. The processing and physical properties of the two materials are well documented in the literature, see for example, [32, 45, 51-56].

A cast Vitreloy 1 plate obtained from the Liquid Metal Technologies, Inc., Lake Forest, CA, was electrical discharge machined into rectangular compression specimens with the dimensions $2.9 \times 2.9 \times 5.8\ mm$. DSC of the as-received material revealed that the onset of its glass transition temperature (T_g) was $623\ K$ and the onset of its crystallization temperature (T_x) was $712\ K$ when subjected to a constant heating rate of 20 K·min^{-1}. The glass transition can be detected to take place at where the slope of the heat flow curve (DSC trace) has a sudden rise, and the intersection of the slopes of the curve before and after the rising is determined by the calorimeter as T_g. Similarly, T_x is determined at the intersection of the slopes of the DSC trace before and after it starts to drop when crystallization takes place.

The Vitreloy 4 samples were prepared from the mixture of the elemental metals of purity ranging from 99.9 to 99.999% by vacuum induction melting in a water cooled copper hearth in the Keck lab at Caltech, followed by vacuum casting to form glassy rods of 3 mm in diameter and 25 mm in length. The rods are cut into specimens of 6 mm in length, with ends ground and polished perpendicular to the specimen axis. T_g and T_x of the as-cast material were measured using DSC to be $617\,K$ and $740.5\,K$, respectively.

The top and bottom surfaces of all specimens were polished with 600-grit sandpaper. During the compression tests, high temperature Bentone-Clay semi-synthetic grease was applied on both surfaces to reduce the effect of friction.

Compression testing was performed at $T = 643\,K$, a constant temperature within the supercooled liquid region of both materials ($T_g < T < T_x$). According to a previous study on the thermodynamic and kinetic properties of the two alloys [32], their time-temperature-transformation diagrams show that Vitreloy 1 has a time window of more than 3,000 seconds before crystallization, while Vitreloy 4 requires more than 10,000 seconds to crystallize at this temperature, which provides ample time for the materials to reach steady state under compressional loading without initiating crystallization from pure thermal effect.

2.2.2 High temperature compression test

Quasi-static uniaxial compression tests were carried out using a servo-hydraulic Materials Testing System (MTS 358 series) with multiple 5-kip/20-kip/50-kip load cartridges and a 5-inch embedded linear variable differential transducer (LVDT) for displacement measurements. The compression test fixture was adopted from the design by Lu [57], including a loading frame with features to accommodate a split electric furnace, an LVDT and its conditioner, and a set of furnaces with a temperature feedback/control system. For a detailed design of the apparatus, the reader is referred to Figure 1 in Chapter 2 of Lu [57]. Small modifications, such as increasing the thickness of the plates that connect the extension rods and filling insulating materials into the furnace chamber, were made on the apparatus to improve the insulation and to minimize thermal flux during the tests.

The displacement measurement was carried out by recording the relative motion of the end surfaces of the two push rods, between which the specimen was sandwiched for loading, using a Schaevitz model # 100-MHR transducer along with a Schaevitz ATA 2001 signal conditioner, which gave an adjustable output resolution of 2~3 mV/micron. The cross-head displacement of the whole fixture, including both specimen displacement and fixture compliance, was also recorded by the MTS machine. The machine compliance was measured by performing tests under the same temperature and strain rate condition without the specimen in the fixture. By subtracting the compliance from the crosshead displacement measurement, the specimen displacement was obtained. The displacements were measured with both techniques during a test to verify each other. Normally, the two values were close to each other namely, with a discrepancy of less than 1%.

The temperature control system consisted of: (1) two pieces of half-cylindrical electrical furnaces, each with 75 mm in diameter and 150 mm in length (model# 5010-1057-00A, Lunaire, WI); (2) a temperature controller (series CN77000, Omega Engineering) working at proportional-integral-derivative (PID) control mode [58]; (3) two solid state relays (series SSR240DC25, Omega Engineering); and (4) a K type thermocouple. The thermocouple was spot welded to the center of the specimen surface and then connected to the temperature controller to ensure an accurate reading of the specimen temperature during the duration of the test. The controller used the thermocouple reading as input and directed the two solid state relays to switch on and off with an adjustable cycling time of a few milliseconds, which proved to be sufficient for the requisite temperature control of the heating apparatus. Thus, the electric furnaces were regulated as the output of the controller were switched on and off accordingly to adjust the specified specimen temperature. A heating rate of $20\,K/\min$ was employed with the ramp heating function of the controller, up until 20 degrees below the desired temperature. At this point, the control was switched to manual tuning to bring the temperature from the set-point to the desired testing temperature. Any temperature increase was performed with caution to avoid overshooting. Once the desired temperature was reached, the control was reverted to the PID auto control mode for the rest of the duration of the test. For different desired temperatures, testing materials and sizes of the specimens, the PID parameters can be changed to achieve optimized performance. In general, it was found that the proportional band (P) should be adjusted within the range of 2 ~ 10 *K*, the parameter for the integral function (I) worked best in the range of 200 ~ 500 seconds, and the parameter for the derivative function (D) fell in the range of 2 ~ 15 seconds. The specimen was held at the testing temperature for 3 to 5 minutes to establish thermal equilibrium throughout the specimen before the loading started. The thermal diffusivity of Vitreloy 1 in the supercooled liquid state was measured to be $5\times10^{-6}\,m^2s^{-1}$ [59], measurement on another Zr- based amorphous alloy showed similar result [60], so the time to establish thermal equilibrium in a cylindrical specimen with a diameter of 5mm could be estimated to be within a few seconds. Therefore, 3 to 5 minutes was sufficient enough to establish thermal equilibrium in the entire body for the specimens with variant sizes and materials. Displacement controlled compressive loading was performed, and the tested specimens were quenched in water right after the loading was completed. The temperature fluctuation during the course of loading was controlled to within $\pm 0.5\,K$ of the desired temperature. Prior to testing the amorphous alloys, a 6-mm tall dummy specimen with two thermocouples, one welded close to its top surface and the other one close to its bottom surface, was heated in the temperature range of $573 \sim 673\,K$. With careful insulation, the difference between the readings of the two thermocouples was within $0.5\,K$, thus defining the uniformity of the temperature throughout the specimen during the tests.

Compression tests at three constant strain rates on the order of 10^{-2}, 10^{-3}, and $10^{-4} s^{-1}$ were performed on both the alloys. Two sets of jump-in-strain-rate tests were also conducted on each alloy. The first set consisted of single-rate-drop tests in which the strain rate dropped from a high strain rate $\dot{\varepsilon}_h$ to a low strain rate $\dot{\varepsilon}_l$ ($\dot{\varepsilon}_l / \dot{\varepsilon}_h < 0.01$) and changed the flow from non-Newtonian mode to Newtonian mode. The results of the constant-strain-rate tests at $\dot{\varepsilon}_l$ and $\dot{\varepsilon}_h$ were compared with the results of the jump-in-strain-rate tests. The second set consisted of compression tests performed with multiple strain-rate-dropping within the non-Newtonian regime and within the Newtonian region, independently. In the non-Newtonian strain rate jump test, attention was paid to ensure that the flow reached steady state at each step before jumping to a lower strain rate.

2.2.3 DSC characterization

All constant-strain-rate tests were performed in the homogeneous flow region for both materials, and hence a small piece of material (~ 15mg) cut from each specimen for DSC examination was assumable able to represent the thermal properties of the entire specimen. Control samples of Vitreloy 1 and Vitreloy 4 were prepared with the same thermal history as those specimens that underwent the longest testing time, i.e., a heating time of ~25 minutes and holding time of ~20 minutes at the desired testing temperature. Thus, by comparing the DSC results of the deformed (tested) specimen and the control sample, the effect of mechanical deformation on the decomposition and nano-crystallization of the alloy could be distinguished from the changes caused by the thermal effect alone. A Netzsch 401 DSC analyzer in the Keck Materials Research Laboratory of Caltech was used in the current investigation. The sample material was placed in the insulated graphite holder of the DSC analyzer and heated at a constant heating rate of $20K \cdot \min^{-1}$ till its melting temperature. The heat releasing history during the process was recorded and a heat flow curve (DSC trace) was constructed. Another DSC run was directly carried out without changing the experimental conditions after the melted sample was cooled down slowly, to construct a baseline for each specimen. The baseline was deducted from the heat flow curve of the first run to obtain the desired measurement.

2.3 Results

2.3.1 Stress-strain response

The true stress-strain curves obtained in uniaxial compression for Vitreloy 1 and Vitreloy 4 deformed at $T = 643\,K$ are shown in Fig. 2.1 for a variety of constant strain rates.

As illustrated in Fig. 2.1 (a) and (b), the stress-strain behaviors of Vitreloy 1 and Vitreloy 4 are highly strain-rate sensitive at 643 *K*, and a trend from non-Newtonian to Newtonian flow mode can be observed with decreasing strain rate. The non-Newtonian flow features of stress overshoot and undershoot are observed in the Vitreloy 1 tests at $\dot{\varepsilon} = 0.04\,s^{-1}$ and $\dot{\varepsilon} = 0.003\,s^{-1}$, as well as in the Vitreloy 4 tests at $\dot{\varepsilon} = 0.05\,s^{-1}$ and $\dot{\varepsilon} = 0.004\,s^{-1}$. The Vitreloy 1 specimen tested at $\dot{\varepsilon} = 3\times10^{-4}\ s^{-1}$and the Vitreloy 4 specimen tested at $\dot{\varepsilon} = 5\times10^{-4}\ s^{-1}$ are at Newtonian flow mode, reaching steady state flow without either over or undershooting and. Slight hardening is observed in both Vitreloy 1 and Vitreloy 4 specimens in the Newtonian flow regime, i.e., Vitreloy 1 at $\dot{\varepsilon} = 3\times10^{-4}\ s^{-1}$ and Vitreloy 4 at $\dot{\varepsilon} = 5\times10^{-4}\ s^{-1}$. Such hardening behavior was also reported by Bletry *et al.* in compression tests of Zr-Al-Ti-Cu-Ni alloys in supercooled state and was considered to result from crystallization in the amorphous alloys during deformation [61]. Nieh *et al.* suggested the formation of a mixed nanocrystalline-amorphous structure during tensile testing of a supercooled Zr-Al-Ti-Cu-Ni alloy [11]. The hardening observed here can be viewed as evidence of partial crystallization in the material during the deformation.

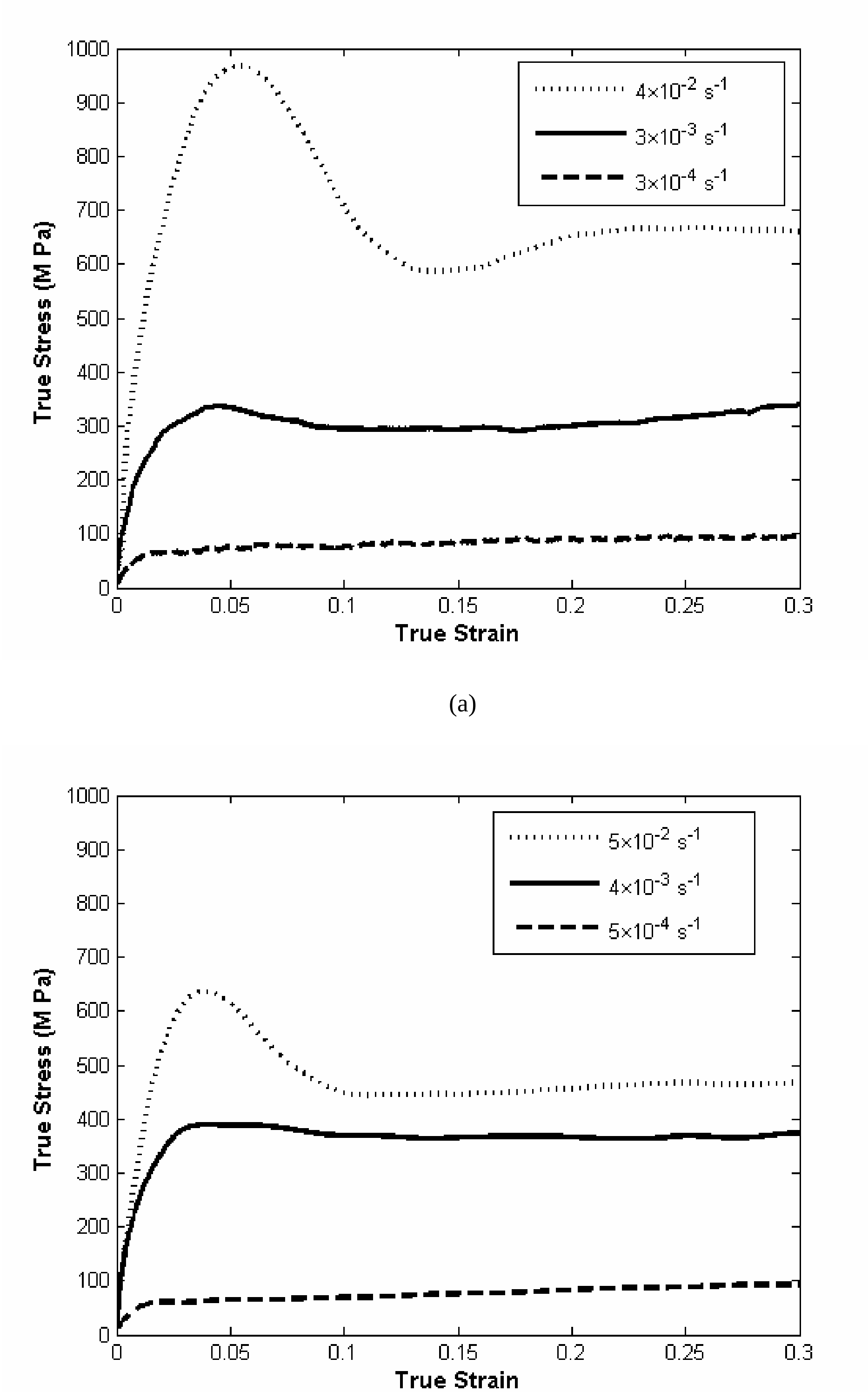

(a)

(b)

Fig. 2.1 True stress-strain curves from compression tests performed at 643 *K* and various strain rates: (a) Vitreloy 1, $\dot{\varepsilon} = 0.04s^{-1}$, $\dot{\varepsilon} = 0.003s^{-1}$ and $\dot{\varepsilon} = 3\times10^{-4}s^{-1}$; (b) Vitreloy 4, $\dot{\varepsilon} = 0.05s^{-1}$, $\dot{\varepsilon} = 0.004s^{-1}$ and $\dot{\varepsilon} = 5\times10^{-4}s^{-1}$.

Jump-in-strain-rate tests were performed on Vit 1 and Vit 4 by dropping the rate to the Newtonian regime after having reached the steady state flow in the non-Newtonian flow regime. The strain rate of the Vit 1 specimen was dropped abruptly from $\dot{\varepsilon} = 0.04\, s^{-1}$ to $\dot{\varepsilon} = 3\times10^{-4}\ s^{-1}$ at a strain of 0.15. The strain rate of Vit 4 was dropped abruptly from $\dot{\varepsilon} = 0.05\, s^{-1}$ to $\dot{\varepsilon} = 5\times10^{-4}\ s^{-1}$ at a strain of 0.25. The true stress-strain curves are compared with those of the corresponding constant strain rate tests in Fig. 2.2. The two alloys exhibit distinct differences in terms of their flow strength after the strain rate drop. For Vitreloy 1, as reported in the literature [13, 61], the final steady state flow stress in the rate jump is the same as that in the constant low rate test (Fig. 2.2.(a)). However, for Vitreloy 4, the flow stress after the rate drop is observed to be less than one third of that of the constant rate test at the corresponding low strain rate (see Fig. 2.2 (b)).

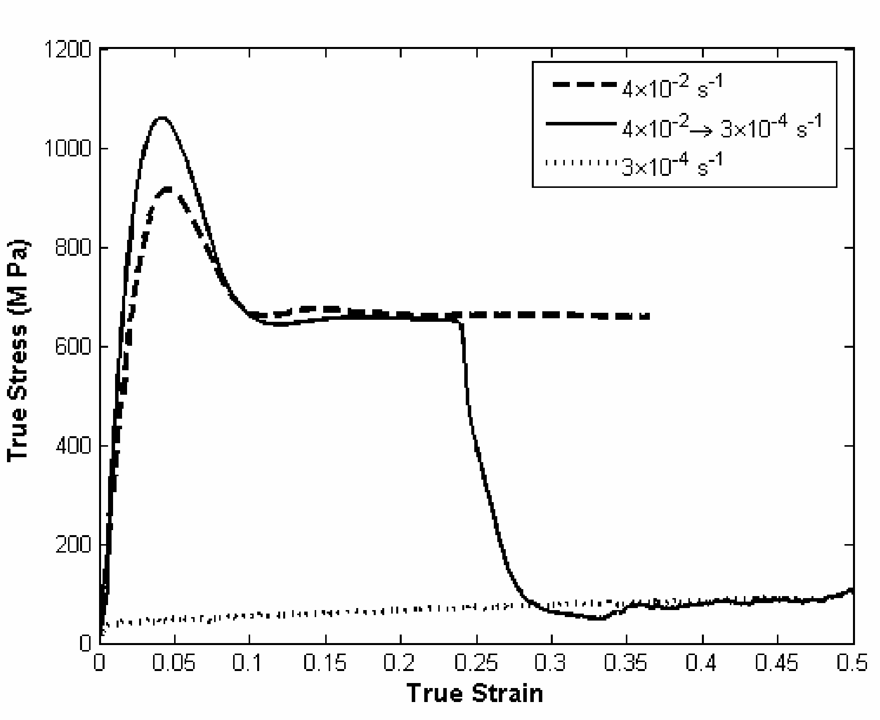

(a)

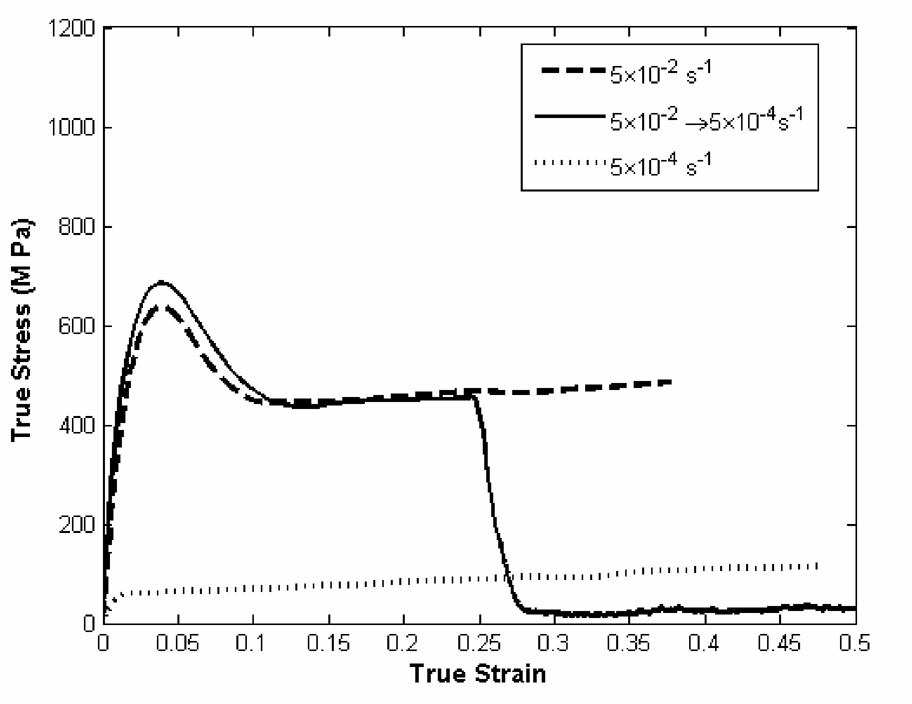

(b)

Fig 2.2 True stress-strain curves from compression tests performed at 643 K at two constant strain rates (one in the non-Newtonian regime and another in the Newtonian regime) and jump (drop) in strain rate with mode of deformation going from non-Newtonian to Newtonian regime: (a)Vitreloy 1, $\dot{\varepsilon} = 0.04 s^{-1}$, $\dot{\varepsilon} = 3\times10^{-4} s^{-1}$ and $\dot{\varepsilon} = 0.04 \rightarrow 3\times10^{-4} s^{-1}$; (b) Vitreloy 4, $\dot{\varepsilon} = 0.05 s^{-1}$, $\dot{\varepsilon} = 5\times10^{-4} s^{-1}$ and $\dot{\varepsilon} = 0.05 \rightarrow 5\times10^{-4} s^{-1}$.

2.3.2 DSC results

The specimens deformed in compression at different strain rates and jump in strain rate from non-Newtonian to Newtonian region were examined along with the two control samples described earlier by DSC at a constant heating rate of $20\,K\,\min^{-1}$. The following important features on the DSC curves of these specimens were examined: 1) the shift in the onset of the glass transition temperature, T_g, and the change in the supercooled liquid region, $\Delta T = T_x - T_g$; 2) the change in the specific heat capacity, c_p, at the glass transition temperature; 3) enthalpy change during the crystallization event(s), i.e., $\Delta \mathrm{H}_{cryl} = \int \Delta c_p dT$, where the subscript *cryl* designates crystallization; and 4) the characteristics of the crystallization event(s). Lower T_g and larger ΔT are believed to be associated with increased thermal stability and better glass formability [32]. The specific heat change at the glass transition region has been considered an important feature in the studies of the thermophysical properties of amorphous materials. Some investigators assume it to be a direct evidence of free volume concentration in the material at the beginning of the DSC scans [18, 25, 26]. Such an assumption provided a good explanation for the present results, which will be discussed later. By comparing the enthalpy change during the crystallization process of the deformed (designated by the subscript *def*) samples and that of the as-cast (designated by the subscript *a-c*) sample, the fraction of crystallization in the materials can be estimated as $f_{cryl} = (\Delta H_{cryl}^{a-c} - \Delta H_{cryl}^{def}) / \Delta H_{cryl}^{a-c}$. The change in the shape of the initial portion of the crystallization curve (spinode) for Vitreloy 1 before the primary crystallization is an indication of intrinsic phase-separation that serves as the nucleation source for subsequent crystallization. A difference in the secondary crystallization of the deformed and the as-cast sample was also noticed.

DSC traces of the as-received sample and a control sample of Vitreloy 1 are shown in Fig. 2.3. The control sample was prepared by being heated up to $643\,K$ at a constant heating rate of approximately 20 *K*/min and holding it at that temperature for 1200 seconds, which was the longest time for the compression tests. The two curves are almost identical. Since the control sample was prepared by applying the same thermal history as the compression specimen with the longest testing time, the effect of heating alone on the phase change can thus be excluded from all the Vitreloy 1 specimens in this investigation that are tested at temperature $T = 643\,K$ within the specified time range.

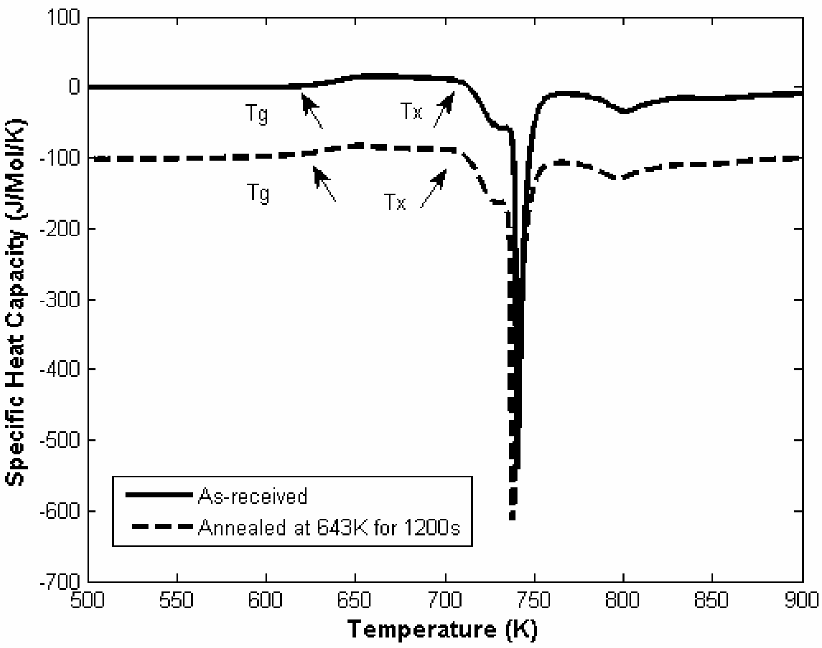

Fig. 2.3 DSC traces of Vitreloy 1 control test sample compared to that of the as-received sample. The annealing time for the control sample represented the longest testing time of Vitreloy 1 in this investigation. The DSC curves are shifted relative to one another along the ordinate for display purposes.

DSC traces of Vitreloy 1 specimens deformed at constant strain rates are shown in Fig. 2.4, and the results are summarized in Table 2.1. With decreasing strain rate, T_g and crystallization ratio f_{cryl} increase, while the span of super-cooled liquid region ΔT decreases (see Table 2.1). This indicates that the material after being mechanically deformed becomes thermally less stable in the super-cooled region than the as received material. Lower strain rate, and therefore longer testing time, is associated with more crystallization and less thermal stability. Another major observation related to the deformation of Vitreloy 1 is that the amplitude of the peak corresponding to the spinodal phase separation nearly doubles in the deformed material in comparison to that of the as-received material and the control sample, which are nearly identical. This implies crystal formation during the thermo-mechanical loading in the high temperature compression test. The crystals that form at the spinode serve as nuclei for further crystallization, and a larger fraction of material is crystallized during tests at the lower strain rates.

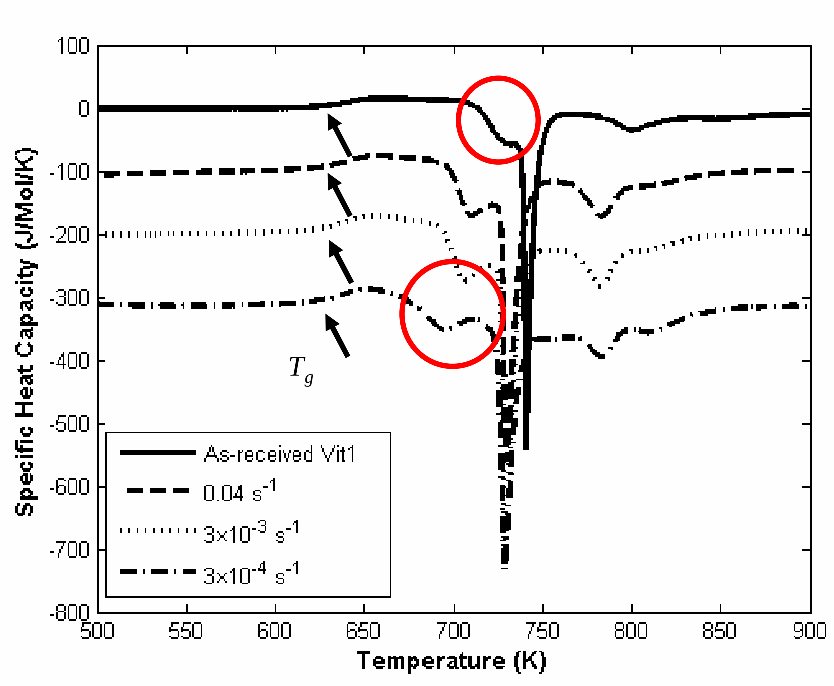

Fig. 2.4 DSC traces of deformed Vitreloy 1 specimens compared to that of the as-received sample. The DSC curves are shifted relative to each other along the ordinate for display purposes. The amplitude of phase-separation spinode (circled in red) increases after mechanical deformation.

Table 2.1 Summary of the DSC results for Vitreloy 1

	As-received Sample	Control Sample	$\dot{\varepsilon} = 0.04\, s^{-1}$	$\dot{\varepsilon} = 0.003 s^{-1}$	$\dot{\varepsilon} = 3\times10^{-4}\, s^{-1}$
T_g (K)	622.8	622.8	622.6	620.0	619.8
$\Delta T = T_x - T_g$ (K)	89.6	88.7	74.4	73.1	65.2
f_{cryl}	-	0	~17%	~20%	~25%
Spinodal phase separation	-	Advanced by ~6 K; almost no change in peak amplitude and shape	Advanced by 15.7 K; peak increased by about twice in amplitude	Advanced by 19.3 K; peak increased by about twice in amplitude	Advanced by 27.4 K; peak increased by about twice in amplitude

The DSC results for Vitreloy 4 are shown in Fig. 2.5 and Fig. 2.6, and the associated values inferred from the traces are tabulated in Table 2.2. As in the case of Vitreloy 1, the control sample was prepared by heating up to $643\,K$ at a constant heating rate of approximately 20 K/min and holding it at that temperature for 1200 seconds, which was the longest time during the compression tests. From its DSC trace (Fig. 2.5), the computed integrated area of the specific heat capacity over the temperature duration of the crystallization event(s) remained almost the same as that of the as-received Vitreloy 4 material; therefore, $f_{cryl} \approx 0$, and the material remained amorphous after the annealing. However, instead of crystallizing in two separate events like the as-received material, the control sample, subjected to pure thermal loading, crystallized in one single event at a lower T_x . The phenomenon of the merging of the two separate crystallization events into one was also observed in isothermal crystallization of other alloys in the Vitreloy family at higher temperatures, which was attributed to the kinetic nature of nucleation [32].

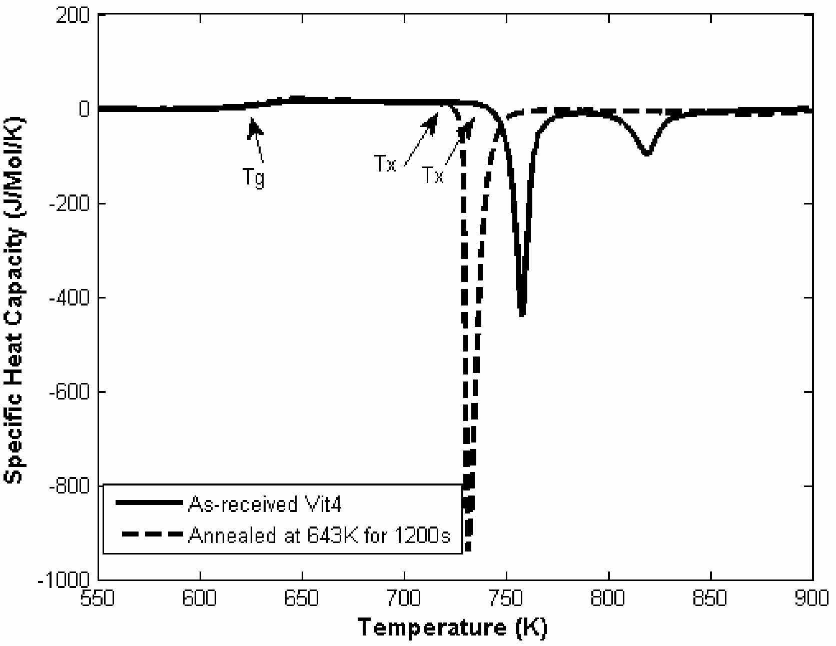

Fig. 2.5 DSC traces of Vitreloy 4 control test sample compared to that of the as-received material. The annealing time of the control sample represented the longest testing time of Vitreloy 4 during compressive loading.

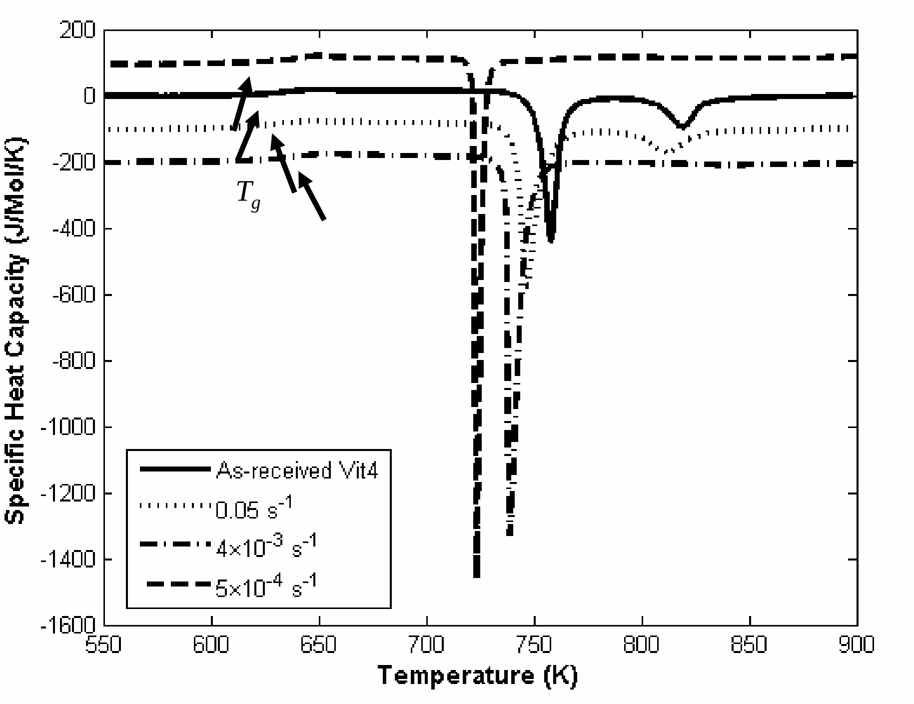

Fig. 2.6 DSC traces of the deformed Vitreloy 4 specimens compared to that of the as-received material. The DSC curves are shifted relative to each other along the ordinate for display purposes.

As shown in Fig. 2.6, the secondary crystallization event for compression samples disappears for all Vitreloy 4 specimens except for the one deformed at $\dot{\varepsilon} = 0.05\ s^{-1}$, which still shows a small secondary crystallization event. The onset of the glass transition temperature T_g decreases with lower strain rate and longer testing time. Also, the onset temperature of rapid primary crystallization also has a tendency of decreasing with lower strain rate, e.g., T_x of the specimen after testing at $\dot{\varepsilon} = 5 \times 10^{-4} s^{-1}$ is approximately 10 *K* lower than that of the as-received material. It is worth noting that the crystallization peak is sharper for samples deformed at lower strain rates. However, the total amount of enthalpy release during crystallization does not change much in different specimens as compared to that of the as-received material, which means the specimens were still amorphous prior to the DSC scanning as discussed previously. The change in kinetic behavior of crystallization during the DSC scanning may be explained by different local decomposition from different thermo-mechanical loading conditions. Such strain-rate induced composition fluctuation is usually too small to be detectable with microprobe techniques [62], but may lend itself to study using techniques with higher resolution, such as small-angle neutron scattering [33].

Table 2.2 Summary of the DSC results for Vitreloy 4

	As-received Sample	Control Sample	$\dot{\varepsilon} = 0.05s^{-1}$	$\dot{\varepsilon} = 0.004s^{-1}$	$\dot{\varepsilon} = 5\times10^{-4}s^{-1}$
T_g (K)	616.9	616.5	611.3	621.1	631.3
$\Delta T = T_x - T_g$ (K)	123.6	105.5	133.7	106.6	96.2
f_{cryl}	-	~ 0	~ 0	~ 0	~ 0
Secondary Crystallization	Yes	No	Yes	No	No

The specimens deformed by jump-in-strain-rate compression from the non-Newtonian regime to the Newtonian regime were also subjected to DSC examination, and the corresponding traces are shown in Fig. 2.7 (a) and (b) for Vitreloy 1 and Vitreloy 4, respectively.

The DSC curve of Vitreloy 1 sample that had been subjected to jump in strain rate possesses similar features as the specimens deformed at constant strain rate, with increasing amplitude and advancing temperature of the peak associated with the spinodal phase-separation before the major crystallization event (Fig. 2.7(a)). Coincidently, the flow stress of Vitreloy 1 after the jump in strain rate remains the same as that of the constant low strain rate deformation. This suggests that there is no substantive structural disordering in the Vitreloy 1 specimens during the jump-in-strain-rate test.

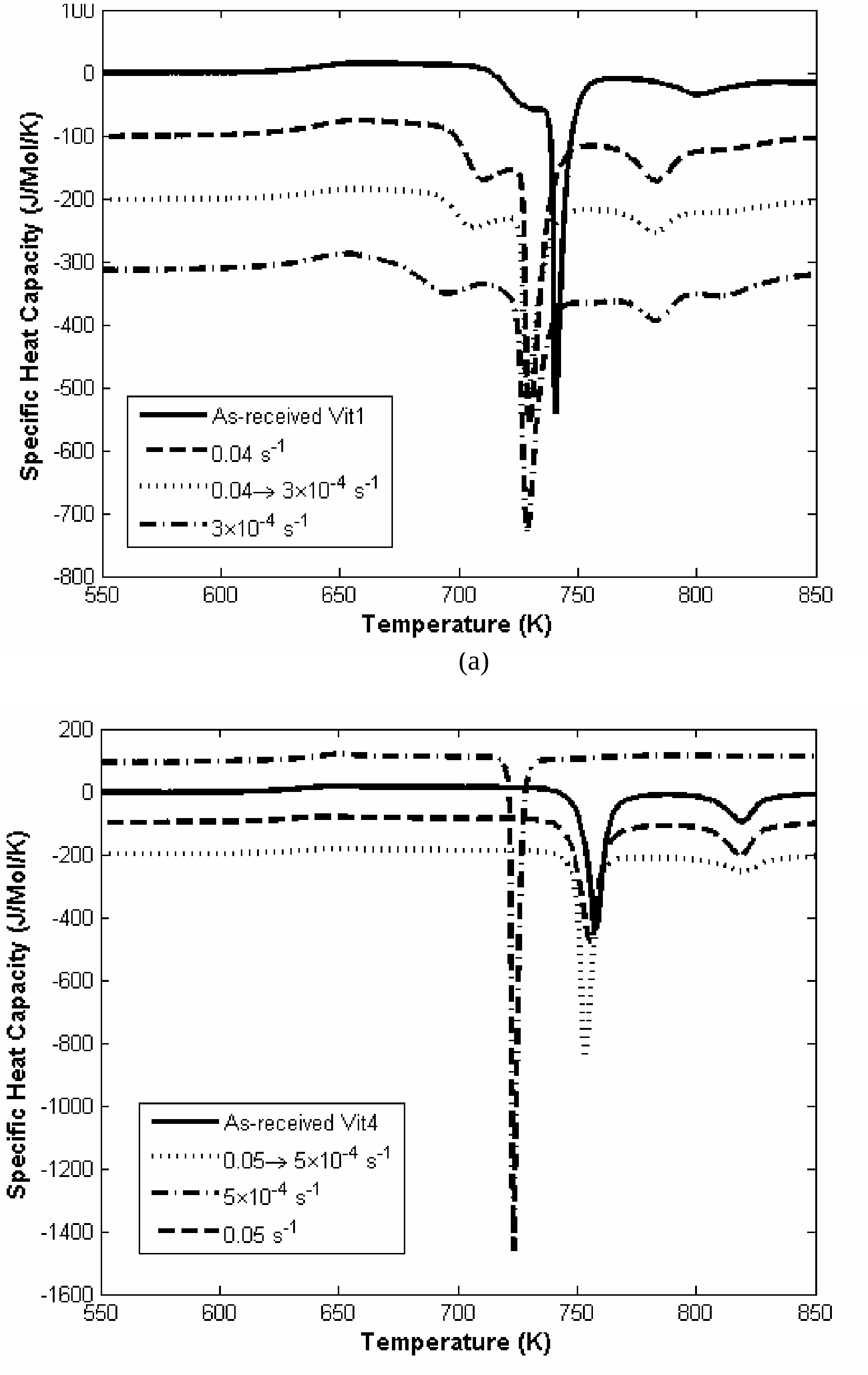

(a)

(b)

Fig. 2.7 DSC traces of specimens subjected to jump in strain rate compared to that of the as-received sample and specimens deformed at constant strain rates: (a) Vitreloy 1 and (b) Vitreloy 4. The DSC curves are shifted relative to each other along the ordinate for display purposes.

The DSC curves of Vitreloy 4 (Fig. 2.7(b)) show a more complicated picture. The DSC trace of the as-received material features a secondary crystallization event after the major crystallization. After being deformed at a low strain rate, the secondary crystallization disappears and the whole crystallization process during DSC scanning becomes a single sharp peak, even though the material prior to the DSC scan remains amorphous. It can be inferred that massive chemical reordering at the atomic level occurs as a result of inelastic deformation and annealing during the high temperature deformation. For Vitreloy 1, the structural relaxation during the high temperature deformation was mostly an effect of strain rate, since the same high temperature history did not introduce discernable change in the DSC curve (Fig. 2.3 and Fig. 2.4). In this set of experiments on Vitreloy 4, the coupling between thermal history (annealing) and mechanical (deformation) effects can not be clearly separated.

By closely examining the supercooled liquid regime in the DSC trace (Fig. 2.8, as part of Fig. 2.7), one can better understand the change in atomic mobility in the two alloys tested under various conditions. Following the model proposed by van den Beukel and Sietsma [25, 63], Δc_p at the glass transition region (the specific heat capacity change from the peak of the glass transition to the equilibrium state as marked in Fig.2.8(b)) is taken as a direct measure of the free volume in the material before the DSC scan. The larger the Δc_p is, the more free volumes are annealed out before the DSC scanning, or in other words, less free volumes are preserved in the material. In the DSC traces of Vitreloy 1 specimens deformed at the low strain rate, high strain rate, and jump-in-strain-rate, it is difficult to get a clear Δc_p measurement, because the structural change is dominated by the spinodal phase separation following right after the glass transition, leaving no time for the glassy state to reach equilibrium (Fig. 2.8(a)). The difference of Δc_p in the DSC traces of Vitreloy 4 specimens is more evident. Δc_p of the specimen deformed at $\dot{\varepsilon} = 5 \times 10^{-4}\ s^{-1}$ is about three times higher than that of the specimens tested at high strain rate and jump in strain rate, suggesting a much smaller amount of free volume in the specimen deformed at a low strain rate.

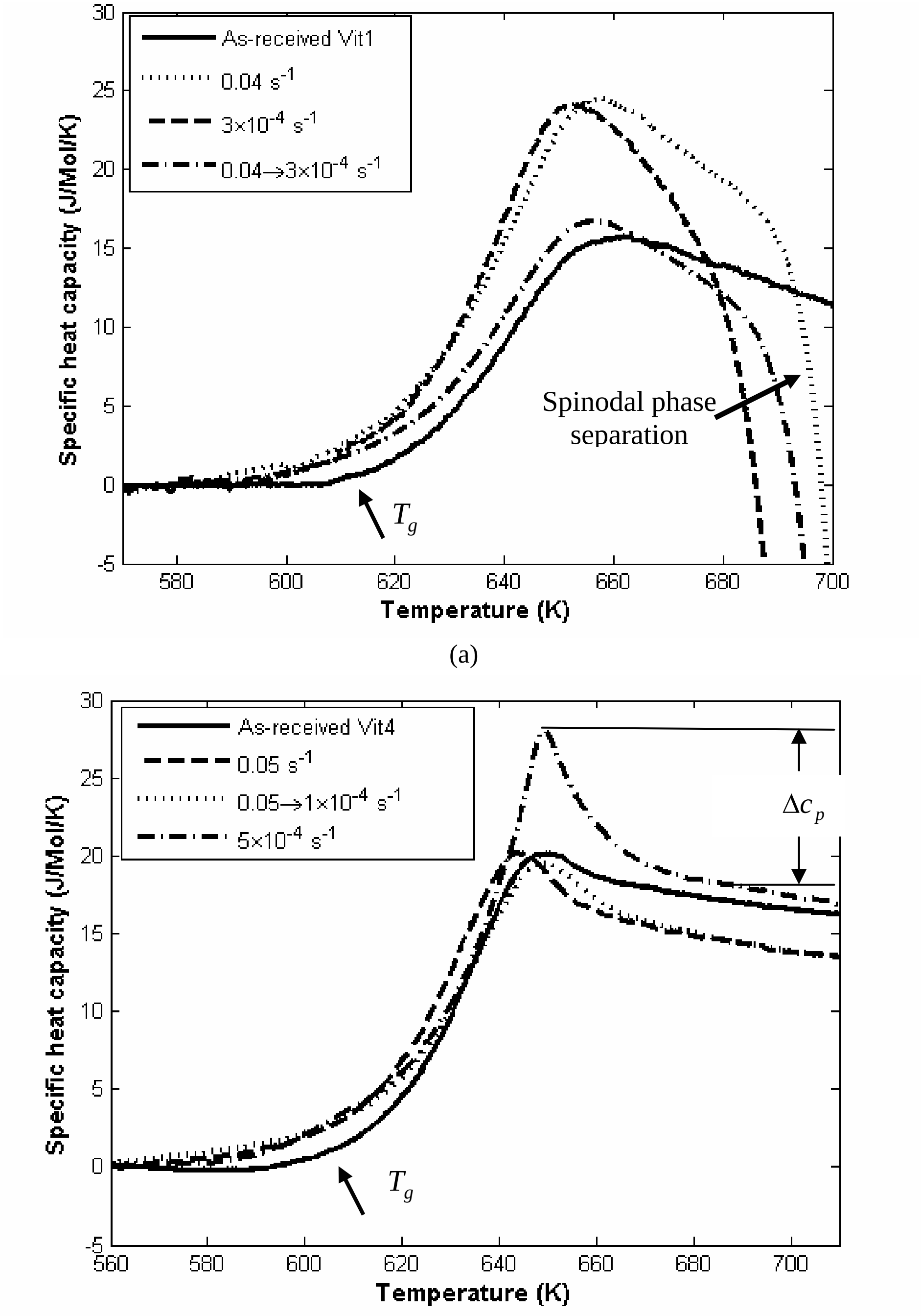

(a)

(b)

Fig 2.8 Glass transition point on the DSC traces of (a) Vitreloy 1 and (b) Vitreloy 4. The Δc_p labeled in (b) is taken as an indication of the free volume stored in the material. Larger Δc_p means less free volume in the material before the DSC scan.

2.3.3Multiple jump-in-strain-rate tests

In order to understand the influence of the structural changes on the mechanical behavior of the two alloys, multiple jump-in-strain-rate tests were performed independently in the non-Newtonian flow region and the Newtonian flow region of both Vitreloy 1 and Vitreloy 4. In a non-Newtonian jump in strain rate test, caution was taken to ensure that the flow had reached steady state at each step before jumping to a lower strain rate. The true stress-strain curves for the successive jump in strain rate tests are plotted in Figs. 2.9(a) and (b) for Vitreloy 1 and Vitreloy 4, respectively. As expected, drops in flow stress were observed at each strain rate drop. The dependence of the steady state flow stress on the strain rate in each test is plotted in Figs. 2.10 (a)-(d) along with predictions from the free volume model discussed in the next section.

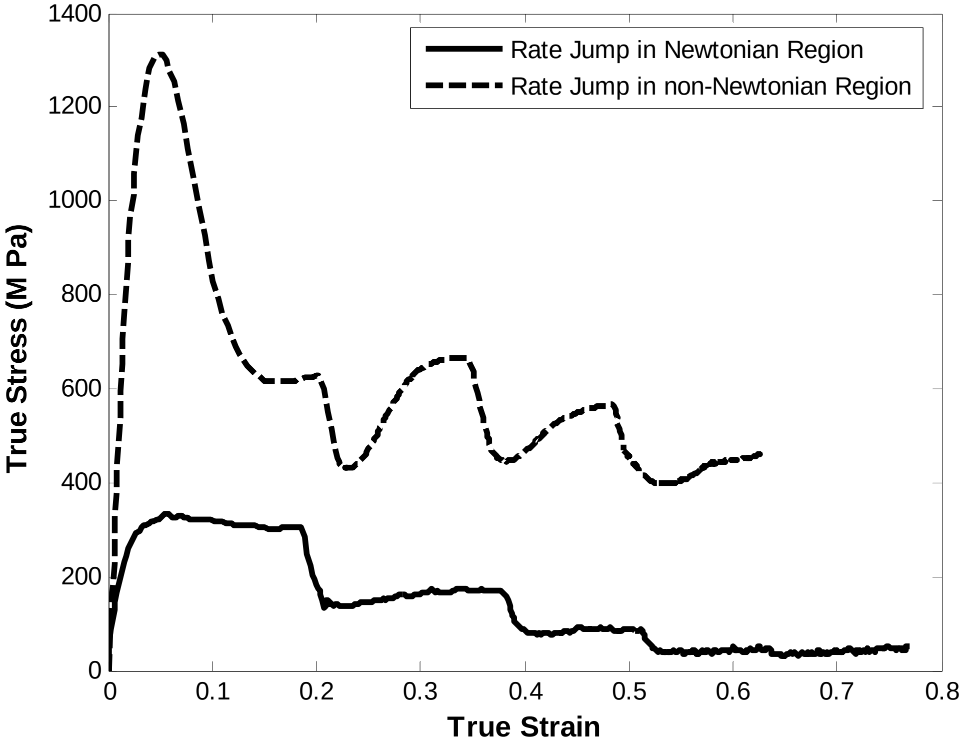

(a)

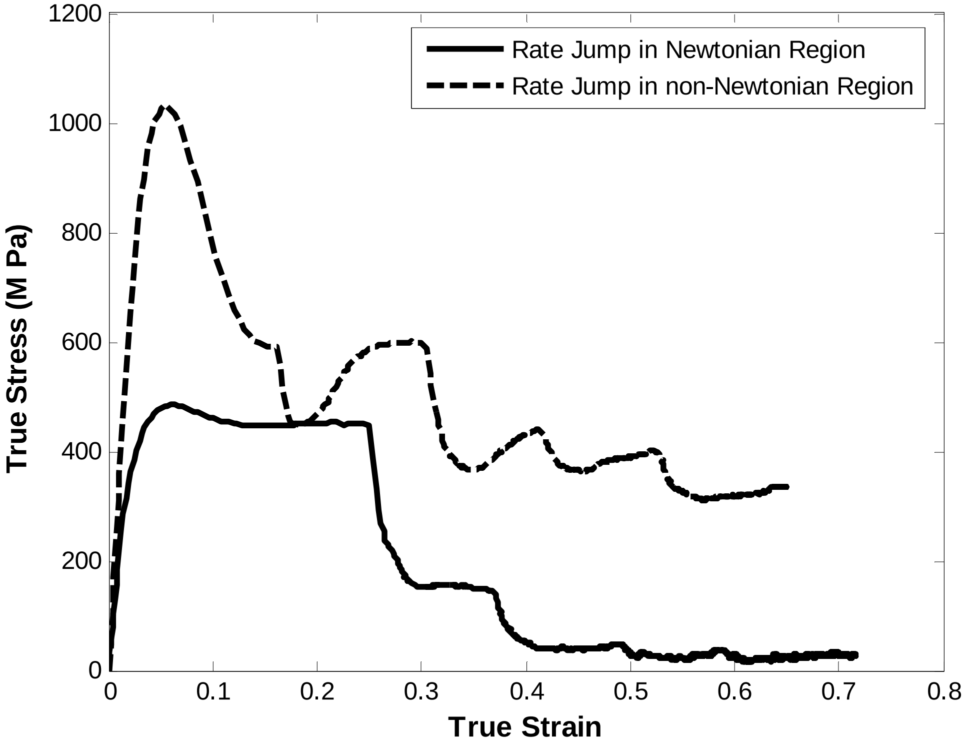

(b)

Fig 2.9 True stress-strain curves for successive jump in strain rate tests of: (a) Vitreloy 1 deformed in the non-Newtonian flow region (solid line) with the strain rate history of $\dot{\varepsilon} = 7.4\times10^{-2} \rightarrow 2.6\times10^{-2} \rightarrow 1.2\times10^{-2} \rightarrow 6.0\times10^{-3} s^{-1}$, deformed in the Newtonian flow region (dashed line) with the strain rate history of $\dot{\varepsilon} = 2.6\times10^{-3} \rightarrow 1.2\times10^{-3} \rightarrow 6.2\times10^{-4} \rightarrow 2.4\times10^{-4} \rightarrow 1.3\times10^{-4}\ s^{-1}$; (b) Vitreloy 4, deformed in the non-Newtonian flow region (solid line) with the strain rate history of $\dot{\varepsilon} = 6.8\times10^{-2} \rightarrow 3.4\times10^{-2} \rightarrow 1.2\times10^{-2} \rightarrow 8.9\times10^{-3} \rightarrow 6\times10^{-3} s^{-1}$, deformed in the Newtonian flow region (dashed line) with the strain rate history of $\dot{\varepsilon} = 1.7\times10^{-2} \rightarrow 3.5\times10^{-3} \rightarrow 1.3\times10^{-3} \rightarrow 4.3\times10^{-4} \rightarrow 1.9\times10^{-4} s^{-1}$.

2.4 Discussion

2.4.1 Deformation induced relaxation phenomena

Even though Vitreloy 1 ($Zr_{41.2}Ti_{13.8}Cu_{12.5}Ni_{10}Be_{22.5}$) and Vitreloy 4 ($Zr_{46.8}Ti_{8.2}Cu_{7.5}Ni_{10}Be_{27.5}$) have close chemical compositions and both exhibit good glass formability and mechanical properties at room temperature, their high temperature deformation properties are quite different, which can be attributed to the different relaxation mechanisms in the two non-equilibrium alloy systems.

DSC examination of the specimens following the compressive deformation in their supercooled liquid regions suggests that the types of phase changes that dominate the relaxation process are quite different in Vitreloy 1 and Vitreloy 4. For the as-received Vitreloy 1 material, the DSC trace at a constant heating rate of 20 K/min features a spinodal portion immediately after the glass transition and before the primary heat release, which indicates the existence of an initial crystallization process prior to the major crystallization event. The so formed crystallites serve as the nuclei for further crystallization. In a study on annealed Vitreloy 1 conducted by Gao et al. [64], it was observed that even at temperatures below the onset crystallization temperature T_x, the spinodal portion started to appear at temperatures above 793 K and increased in magnitude and advanced in the incubation time with higher temperatures. They called this sequence a “multi-stage crystallization” and reported the formation of different phases during the different crystallization stages in a TEM study. In the first spinodal stage, TEM images showed that some nanocrystals precipitated from the amorphous matrix and stabilized the rest of the amorphous phase. As the crystallization proceeded, the nanocrystals precipitated in the first stage grew gradually and other crystals also started to form from the amorphous matrix. Finally, the amorphous alloy fully crystallized with longer annealing times. *In-situ* Small-angle-neutron-scanning performed by Loffler and Johnson [65] also supported the same conclusion that in the relaxation of Vitreloy 1, there is a phase separation at the nano-scale preceding the major crystallization event. In the present study, mechanical loading acting on the supercooled liquid resulted in a similar effect on the structural relaxation process of Vitreloy 1. DSC examination of the specimens after compressive deformation also shows increase in the amplitude of the spinode signal and advancement of the spinodal event. Annealing without mechanical loading at 643 K for the duration of the longest testing time (1200 s) does not show any discernable effect on the phase changes in the alloy. The control sample has an almost identical DSC trace as the as-received material. This suggests that phase separation and nano-crystallization similar to the observation of Gao *et al.* [64] are triggered by the coupled thermal and mechanical driving forces.

For Vitreloy 4, the DSC trace of the as-received material features two crystallization events, with a smaller secondary event following the primary one. It does not have the spinodal phase-separation as observed in Vitreloy 1. The supercooled liquid regime of Vitreloy 4 (ΔT =123 K) is also than that of Vitreloy 1 (ΔT =89 K). Therefore, it can be concluded that the thermal stability of Vitreloy 4 is better than that of Vitreloy 1 [32]. Indeed, no crystallization was found in the mechanically deformed Vitreloy 4 specimens. The most evident phenomenon in the DSC traces of the deformed Vitreloy 4 specimens is that after the coupled thermal and mechanical loading, the two crystallization events converged to become a single sharp and abrupt peak. After the compressive deformation at a relatively high strain rate ($\dot{\varepsilon} = 0.05\, s^{-1}$, testing time 10 *s*), the secondary crystallization decreased but did not totally disappear from the DSC trace. With lower strain rates and longer testing time, the second crystallization has a tendency to disappear; and after the relatively very low strain rate testing (strain rate $\dot{\varepsilon} = 5 \times 10^{-4}\, s^{-1}$, testing time 1200 *s*), the peak of the specific heat released at the major crystallization is more than 3 times higher than that of the primary crystallization of the as-received material. The control specimen which was subjected to the same thermal history as the specimen tested at low strain rate (linearly heated to $643\, K$ at a constant heating rate of $20\, K \cdot \min^{-1}$ and held at $643\, K$ for 1200 *s*) shows a similarly single major crystallization event in the DSC trace, but the crystallization peak is not as abrupt as those found after mechanical deformation. The crystallization peak of the DSC trace of the mechanically deformed specimen is more than twice as high as and much narrower than the corresponding thermal control specimen. This suggests that the relaxation process in Vitreloy 4 is driven by both mechanical and thermal effects. The integrated areas of the crystallization event(s), i.e., enthalpy released during the crystallization(s) remain the same in all specimens, which suggests that the specimens are still entirely amorphous despite the change in character of the DSC traces. A similar phenomenon of merging of crystallization events was also observed by other researchers in isothermal calorimetrical study on Vitreloy 4 [32]. Such a phenomenon is associated with the change of atomic mobility in the alloy system. Upon thermo-mechanical relaxation, the atoms in Vitreloy 4 decompose into clusters with local atomic density fluctuation. Both the time scale of the decomposition process and the composition difference between the decomposed phases and the nominal composition of the as-received material affect the sequence and extent of the crystallization event(s). It was proposed by Waniuk *et al.* [32] on isothermal annealing study of the Vitreloy 1~Vitreloy 4 alloy family that the decomposition process acts as a precursor to crystallization in the case of low-temperature annealing where both primary and secondary crystallizations exist, while it does not influence high temperature crystallization where only one abrupt crystallization event exists. It was also proposed that the alloy with the largest composition difference between the primary quasi-crystalline phase and the nominal composition should have the most sluggish crystallization kinetics [32].

In the present study, experiments were performed at the same temperature $T = 643\,K$ but at different strain rates. An analogy can be made, namely, that during the high strain rate testing, the decomposition process which facilitates the formation of both first and secondary crystallization is accelerated by the mechanical driving force, while during the low strain rate testing, the material has more time to relax to a state with less composition fluctuation, and hence the secondary crystallization disappears. The appearance of two slower crystallization events is associated with higher compositional fluctuation, which was the case of the high strain rate deformation in this investigation. Therefore, during the high temperature deformation of Vitreloy 4, mechanical loading at different strain rates introduced structural relaxation in the material and caused different decomposition configurations without necessarily introducing phase-separation or nano-crystallization.

2.4.2 Free volume change during jumps in strain rate experiments

The hypothesis on the existence of free volume in glassy materials was first proposed by Cohen and Turnbull [2] and was subsequently adapted for metallic glasses by Spaepen [22]. Metallic glasses are formed by rapidly quenching metallic melts (liquids) at certain rates to restrict their atomic movements and suppress crystallization. Therefore, a certain amount of "holes" or "voids" of various sizes are quenched into the atom clusters that form the amorphous structure. Such "holes" or "voids" are referred to as "free volume", which is suggested to be the key to allow the atomic motion for the diffusive arrangement or ordering of atoms. The possibility of an atom jumping into adjacent holes (free volumes) depends on the relative size of the atoms and the holes. The creation and annihilation of free volume during structural relaxation of amorphous alloys is both a kinetic and a thermodynamic process.

As shown in Fig. 2.8(a), the amount change of the free volumes in the glass transition region of deformed Vitreloy 1 is suppressed or obscured by the dominant spinodal phase separation and crystallization event. Specimen that was subjected to strain-rate-drop deformation has almost the same amount of free volume as its constant strain rate test counterpart. In Vitreloy 4, specimens deformed at different strain rates and strain-rate-drop exhibited clear differences in terms of the amount of free volumes in the material. The one tested at the lowest strain rate has the least amount of free volume. The specimen subjected to jump in strain rate retains almost the same amount of free volume as the one deformed at high strain rate, even though the time subjected to deformation in the jump test is much longer than the constant strain rate test. This is possibly due to the fact that Vitreloy 4 has different relaxation mechanisms during deformation at low strain rate and high strain rate, as discussed above. At low strain rate, Vitreloy 4 has enough time to relax to a stable state, which is less influenced by decomposition, and the free volume is annealed out during the process. During the high strain rate deformation, the structural relaxation process is dominated by decomposition, which gives more room for creation of holes and voids during the rearrangement of atoms and atom clusters, or in other words, more free volume is created. In the jump-in-strain-rate test, a certain amount of free volume has already created and accumulated during the first portion of the deformation before the strain rate drops. The free volume is preserved during the latter stages of the deformation.

With the assumption that the heat release rate of an amorphous material is proportional to the rate of creation of free volume, a group of researchers [18, 25, 26] studied the free volume evolution during high temperature deformation and concluded that the free volume increases with strain rate and strain until steady state flow occurs, which agreed with the experimental observations in this investigation.

2.4.3 Effect of free volume on the flow stress

. In Spaepen's free volume model [22], a correlation between the strain rate, the concentration of flow defects, and the flow stress was proposed as

$$\dot{\varepsilon} = 2c_f k_f \frac{\varepsilon_o v_o}{\Omega} \sinh\left(\frac{\sigma \varepsilon_o v_o}{2k_B T}\right), \qquad (2.1)$$

where $\dot{\varepsilon}$ is the strain rate, σ is the uniaxial stress, c_f is the concentration of flow defects, k_f is a rate factor, Ω is the atomic volume, k_B is the Boltzmann's constant, and T is the ambient temperature. The product $\varepsilon_o v_o$ is the activation volume of the process (V_a), which will be calculated for both alloys in section 2.4.4. In Spaepen's model, the concentration of flow induced defects results in the accumulation of the excess free volume in the material. It can be inferred from Eq. (2.1) that the sinh of the flow stress is correlated with the defect concentration in an inverse manner at a constant strain rate.

Such a correlation can be used to explain the differences in mechanical behavior of Vitreloy 1 and Vitreloy 4 in terms of the flow stress in the jump-in-strain-rate-tests. From Fig. 2.8(a), no obvious difference in the amount of free volume retained in the low strain rate and jump in strain rate tests of Vitreloy 1 could be discerned. So the steady state flow stress in the jump in strain rate test is almost identical to the flow stress in the corresponding constant strain rate test as shown in Fig. 2.2(a). However, in Vitreloy 4, Fig. 2.8(b) showed less amount of free volume in the specimen deformed at the low strain rate, and that made the material stronger than the specimen that was subjected to jump-in-strain-rate, as shown in Fig. 2.2(b).

2.4.4 Activation volume in the non-Newtonian and Newtonian flows

The results from the successive jump in strain rate tests independently in Newtonian and non-Newtonian regions (Figs. 2.9(a) and (b)) are used to fit the activation volume $\varepsilon_o v_o$ in Eq. (2.1). The best fits from the free volume model are shown in Figs. 2.10 (a)-(d) for Vitreloy 1 and Vitreloy 4, both in the non-Newtonian regime (Fig. 2.10 (a) and (c)) and in the Newtonian regime (Fig. 2.10 (b) and (d)). The experimental data are shown as solid squares and the fits of data with Eq. (1) are shown with solid lines. The activation volume $\varepsilon_o v_o$ (V_a) and the pre-factor $2k_f c_f \varepsilon_o v_o \Omega^{-1}$ are taken as fitting parameters. The best fitting parameters are calculated for each set of data and are shown in Table 2.3. For both Vitreloy 1 and Vitreloy 4, the activation volume V_a is much smaller in the Newtonian regime (~ 70 Å^3) than in the non-Newtonian regime (~ 120 Å^3), which is reasonable because the supercooled liquids are expected to possess more atomic mobility in the Newtonian flow regime. It is also noticed that the model prediction of the flow stress in the very last step of the Newtonian jump tests was lower than the experimentally obtained flow stress for both materials, especially for Vitreloy 1, which could be attributed to the fact that the nanocrystals accumulated during the deformation contributed to the strength of the materials.

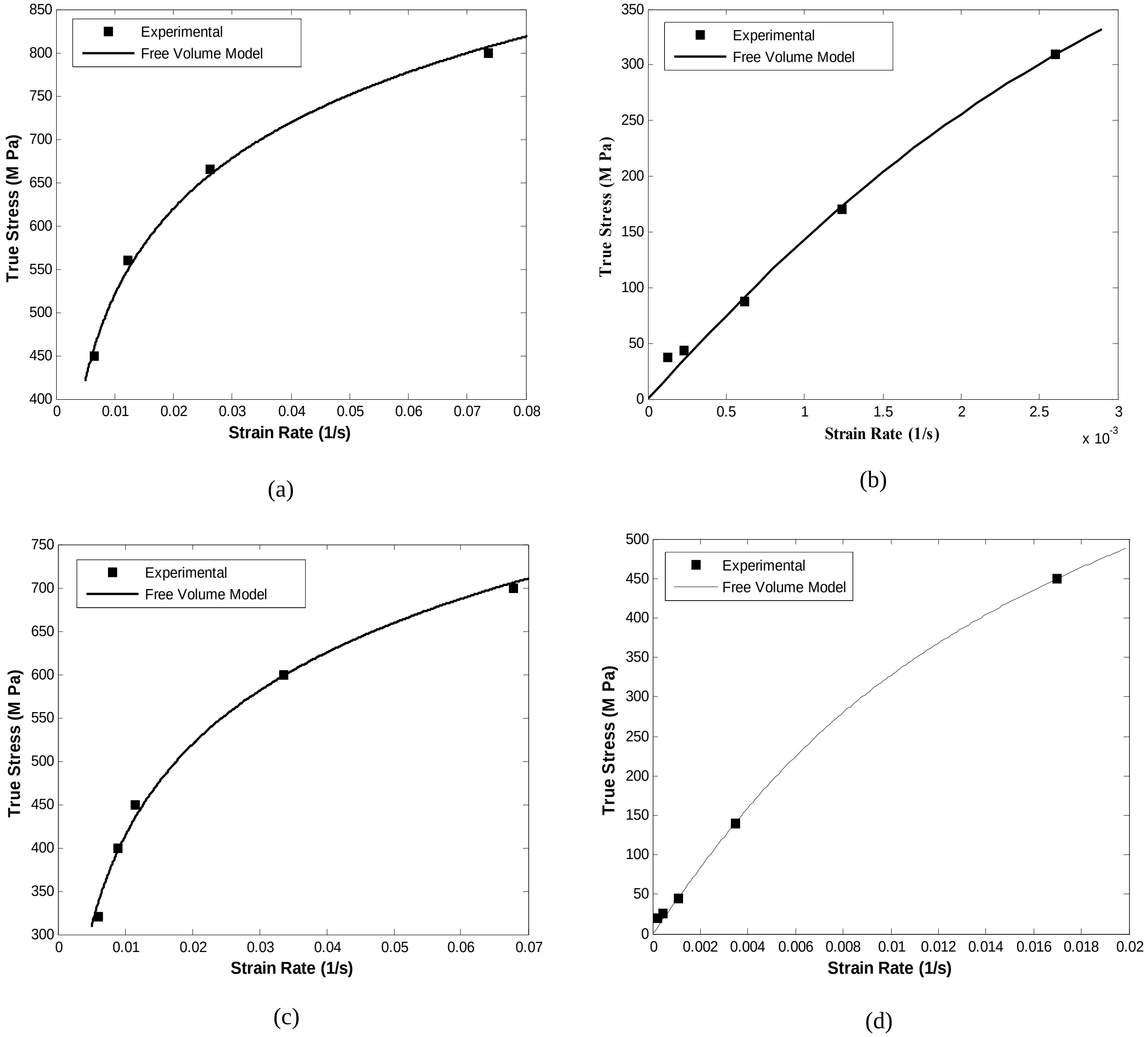

(a)

(b)

(c)

(d)

Fig. 2.10 Experimental and predicted strain rate dependence of flow stress from multiple jump-in-strain-rate tests at 643 *K*. For Vitreloy 1: (a) in the non-Newtonian flow region and (b) in the Newtonian flow region. For Vitreloy 4: (c) in the non-Newtonian flow region and (d) in the Newtonian flow region. The solid lines are model predictions using Eq. (1). See Table 2.3 for the model fitting parameters in each case.

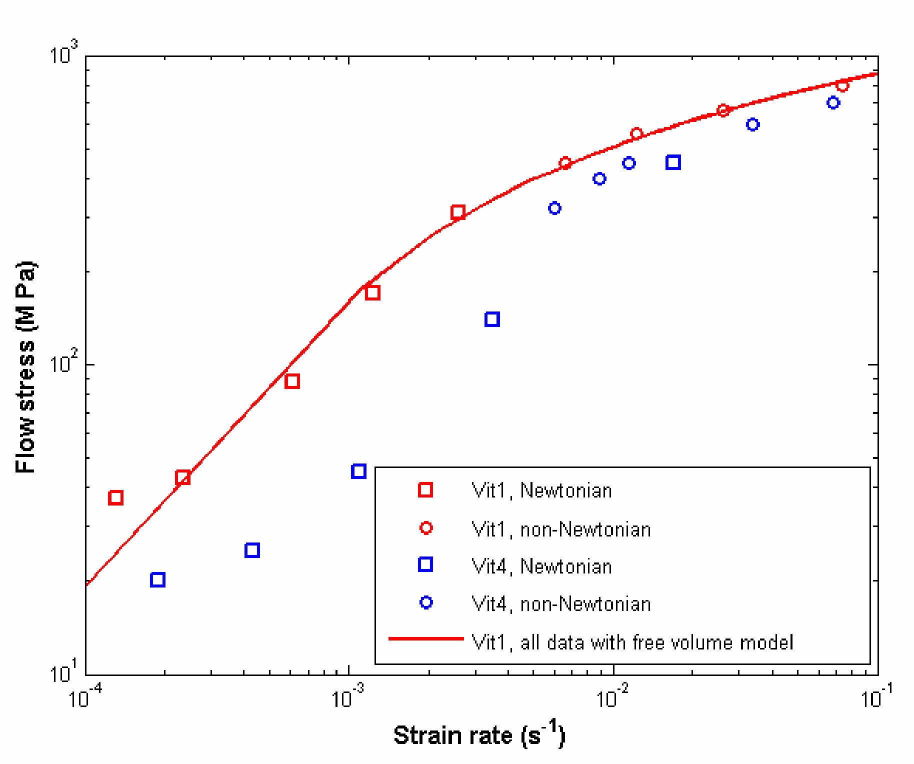

Fig. 2.11 Strain rate and flow stress relation of all data points from successive jump in strain rate tests for Vit 1 and Vit 4. The Vit 1 data (red ones) from non-Newtonian and Newtonian regions fall on a master curve and could be fit using Eq. (1) (solid line), while the non-Newtonian and Newtonian data of Vit 4 (blue ones) do not form a master curve.

Table 2.3Fitting parameters for the free volume model (Eq. (2.1)) from the multiple strain rate jump tests

Material	$V_a = \varepsilon_o v_o \quad (\dot{A}^3)$	$2k_f c_f \varepsilon_o v_o \Omega^{-1} \quad (s^{-1})$
Vit 1, non-Newtonian	123.7	5.34e-4
Vit 1, Newtonian	70.5	1.67e-3
Vit 1, both	111.7	8.30e-4
Vit 4, non-Newtonian	115.8	1.36e-3
Vit 4, Newtonian	69.6	6.01e-3

Data from all the tests are combined together and plotted on a logarithmic scale in Fig. 2.11. Consistent with the discussion in section 2.4.3, the rate jump does not have a strong influence on the flow stress of Vitreloy 1. The non-Newtonian and Newtonian results from Vitreloy 1 fall into two master curves and can also be approximated by one with the free volume model (shown as the red solid line in Fig. 2.11). The activation volume and pre-factor are also calculated for the combined set of data and the values are listed in Table 1. However, for Vitreloy 4, there is a clear discrepancy in the data from the non-Newtonian regime and the Newtonian regime. The flow stress of Vitreloy 4 decreases after dropping in the strain rate in the Newtonian regime (blue open squares in Fig. 2.11), while such a drop is not observed for the test in the non-Newtonian regime (blue open circles in Fig. 2.11).

2.5 Conclusions

The high temperature deformation mechanisms of two amorphous alloys, $Zr_{41.2}Ti_{13.8}Cu_{12.5}Ni_{10}Be_{22.5}$ (Vitreloy 1 or Vit 1) and $Zr_{46.8}Ti_{8.2}Cu_{7.5}Ni_{10}Be_{27.5}$ (Vitreloy 4 or Vit 4), were studied under uniaxial compression combined with DSC examination. The following conclusions can be drawn from this investigation:

(i) DSC examination on Vit 1 and Vit 4 specimens deformed at 643 *K* and different strain rates revealed structural different relaxation mechanisms in the two material systems. In Vit1, mechanical loading increases the extent of the spinodal phase-separation and accelerates it to occur at lower temperature. This phase-separation is responsible for nucleating nano-crystallites during the low strain rate tests. In Vit 4, no such phase separation is discerned from the DSC traces. Decomposition in the form of local chemical composition fluctuation dominates and has a strong influence in the deformation tests performed at relatively high strain rates. Such influence is small when the material is compressed at a much lower strain rate since the material has enough time to relax to a more stable configuration.

(ii) Because of the different relaxation mechanisms in Vit 1 and Vit 4, the change of amount of free volumes in the material after deformation is different in Vit 1 and Vit 4. The amount of free volume in Vit 1 does not show noticeable change after either constant strain rate or jump in strain rate deformations. For Vit 4, the specimen tested at very low strain rate has more free volume annealed out during the process. The specimen subjected to jump in strain rate accumulated certain amount of free volume during the high strain rate portion of the deformation. Due to the correlation that more free volume is associated with lower flow stress at the same strain rate (Eq. (2.1)), the Vit 4 specimen subjected to jump in strain rate test loses two thirds of its flow stress (strength) compared to the one deformed at a corresponding constant strain rate. Vit 1 specimen subjected to jump in strain rate has almost identical flow stress after the drop in strain rate as the one subjected to corresponding constant strain rate.

(iii) The activation volumes of non-Newtonian flow and Newtonian flow for Vit 1 and Vit4 are calculated from the results of successive strain rate jump tests. The Vit 1 data from both Newtonian and non-Newtonian flow regimes can be fitted with a single activation volume.

References

[1] W. Klement, R. H. Willens, and P. Duwez, "Non-Crystalline Structure in Solidified Gold-Silicon Alloys," *Nature*, **187**, 869-870 (1960).

[2] D. Turnbull, "On free-volume model of liquid-glass transition," *The Journal of chemical physics*, **52**, 3038 (1970).

[3] A. Peker and W. L. Johnson, "A Highly Processable Metallic-Glass - $Zr_{41.2}Ti_{13.8}Cu_{12.5}Ni_{10.0}Be_{22.5}$," *Applied Physics Letters*, **63**, 2342-2344 (1993).

[4] A. Inoue, T. Nakamura, N. Nishiyama, and T. Masumoto, "Mg-Cu-Y Bulk Amorphous-Alloys with High-Tensile Strength Produced by a High-Pressure Die-Casting Method," *Materials Transactions Jim*, **33**, 937-945 (1992).

[5] W. L. Johnson, "Metastable Phases," in *Intermetallic Compounds*, vol. 1, J. H. Westbrook, Fleischer, R.L., Ed. New York: Wiley, 687-709, (1994).

[6] Narayana.OS, "Model of Structural Relaxation in Glass," *Journal of the American Ceramic Society*, **54**, 491-& (1971).

[7] M. Scott, Staffan, "Short-range ordering during structural relaxation of the metallic-glass $Fe_{40}Ni_{40}B_{20}$," *Acta metallurgica*, **30**, 853-860 (1982).

[8] T. Jagielinski and T. Egami, "Reversibility of the Structural Relaxation in Amorphous-Alloys," *Journal of Applied Physics*, **55**, 1811-1813 (1984).

[9] K. F. Kelton and F. Spaepen, "Kinetics of Structural Relaxation in Several Metallic Glasses Observed by Changes in Electrical-Resistivity," *Physical Review B*, **30**, 5516-5524 (1984).

[10] S. Schneider, U. Geyer, P. Thiyagarajan, R. Busch, R. Schulz, K. Samwer, and W. L. Johnson, "Phase separation and crystallization in the bulk amorphous $Zr_{41.2}Ti_{13.8}Cu_{12.5}Ni_{10.0}Be_{22.5}$ alloy," *Metastable, Mechanically Alloyed and Nanocrystalline Materials, Pts 1 and 2*, **225**, 59-64 (1996).

[11] T. G. Nieh, J. Wadsworth, C. T. Liu, T. Ohkubo, and Y. Hirotsu, "Plasticity and structural instability in a bulk metallic glass deformed in the supercooled liquid region," *Acta Materialia*, **49**, 2887-2896 (2001).

[12] T. G. Nieh, C. Schuh, J. Wadsworth, and Y. Li, "Strain rate-dependent deformation in bulk metallic glasses," *Intermetallics*, **10**, 1177-1182 (2002).

[13] J. Lu, G. Ravichandran, and W. L. Johnson, "Deformation behavior of the $Zr_{41.2}Ti_{13.8}Cu_{12.5}Ni_{10.0}Be_{22.5}$ bulk metallic glass over a wide range of strain-rates and temperatures," *Acta Materialia*, **51**, 3429-3443 (2003).

[14] Y. Kawamura, T. Shibata, A. Inoue, and T. Masumoto, "Deformation behavior of $Zr_{65}Al_{10}Ni_{10}Cu_{15}$ glassy alloy with wide supercooled liquid region," *Applied Physics Letters*, **69**, 1208-1210 (1996).

[15] B. van Aken, P. de Hey, and J. Sietsma, "Structural relaxation and plastic flow in amorphous $La_{50}Al_{25}Ni_{25}$," *Materials Science and Engineering a-Structural Materials Properties Microstructure and Processing*, **278**, 247-254 (2000).

[16] D. Lee, "Localized Vs Homogeneous Deformation in $Fe_{82}B_{15}Si_3$ Amorphous Alloy," *Metallurgical Transactions a-Physical Metallurgy and Materials Science*, **12**, 419-424 (1981).

[17] Y. Kawamura, T. Nakamura, and A. Inoue, "Superplasticity in $Pd_{40}Ni_{40}P_{20}$ metallic glass," *Scripta Materialia*, **39**, 301-306 (1998).

[18] P. de Hey, J. Sietsma, and A. Van den Beukel, "Structural disordering in amorphous $Pd_{40}Ni_{40}P_{20}$ induced by high temperature deformation," *Acta Materialia*, **46**, 5873-5882 (1998).

[19] A. S. Argon, "Plastic-Deformation in Metallic Glasses," *Acta Metallurgica*, **27**, 47-58 (1979).

[20] A. S. Argon and L. T. Shi, "Development of Visco-Plastic Deformation in Metallic Glasses," *Acta Metallurgica*, **31**, 499-507 (1983).

[21] J. Megusar, A. S. Argon, and N. J. Grant, "Plastic-Flow and Fracture in $Pd_{80}Si_{20}$ near Tg," *Materials Science and Engineering*, **38**, 63-72 (1979).

[22] F. Spaepen, "Microscopic Mechanism for Steady-State Inhomogeneous Flow in Metallic Glasses," *Acta Metallurgica*, **25**, 407-415 (1977).

[23] F. Spaepen and D. Turnbull, "Mechanism for Flow and Fracture of Metallic Glasses," *Scripta Metallurgica*, **8**, 563-568 (1974).

[24] P. S. Steif, F. Spaepen, and J. W. Hutchinson, "Strain Localization in Amorphous Metals," *Acta Metallurgica*, **30**, 447-455 (1982).

[25] P. A. Duine, J. Sietsma, and A. Vandenbeukel, "Defect Production and Annihilation near Equilibrium in Amorphous Pd40ni40p20 Investigated from Viscosity Data," *Acta Metallurgica Et Materialia*, vol. 40, pp. 743-751, 1992.

[26] P. de Hey, J. Sietsma, and A. vandenBeukel, "Creation of free volume in amorphous $Pd_{40}Ni_{40}P_{20}$ during high temperature deformation," *Materials Science and Engineering a-Structural Materials Properties Microstructure and Processing*, **226**, 336-340 (1997).

[27] V. A. Khonik, "The kinetics of irreversible structural relaxation and homogeneous plastic flow of metallic glasses," *Physica Status Solidi a-Applied Research*, **177**, 173-189 (2000).

[28] V. A. Khonik, "Mechanical relaxations in metallic glasses," *Mechanical Spectroscopy Ii, Proceedings*, **89**, 67-92 (2003).

[29] J. S. Langer and L. Pechenik, "Dynamics of shear-transformation zones in amorphous plasticity: Energetic constraints in a minimal theory," *Physical Review E*, **68**, 061504 (2003).

[30] W. L. Johnson and K. Samwer, "A universal criterion for plastic yielding of metallic glasses with a $(T/T\text{-}g)^{(2/3)}$ temperature dependence," *Physical Review Letters*, **95**, 195501 (2005).

[31] F. H. Stillinger, "A Topographic View of Supercooled Liquids and Glass-Formation," *Science*, **267**, 1935-1939 (1995).

[32] T. Waniuk, J. Schroers, and W. L. Johnson, "Timescales of crystallization and viscous flow of the bulk glass-forming Zr-Ti-Ni-Cu-Be alloys," *Physical Review B*, **67**, 184203, 2003.

[33] E. Pekarskaya, J. F. Loffler, and W. L. Johnson, "Microstructural studies of crystallization of a Zr-based bulk metallic glass," *Acta Materialia*, **51**, 4045-4057 (2003).

[34] W. J. Wright, T. C. Hufnagel, and W. D. Nix, "Free volume coalescence and void formation in shear bands in metallic glass," *Journal of Applied Physics*, **93**, 1432-1437 (2003).

[35] J. Li, F. Spaepen, and T. C. Hufnagel, "Nanometre-scale defects in shear bands in a metallic glass," *Philosophical Magazine a-Physics of Condensed Matter Structure Defects and Mechanical Properties*, **82**, 2623-2630 (2002).

[36] H. Chen, Y. He, G. J. Shiflet, and S. J. Poon, "Deformation-Induced Nanocrystal Formation in Shear Bands of Amorphous-Alloys," *Nature*, **367**, 541-543 (1994).

[37] M. C. Gao, R. E. Hackenberg, and G. J. Shiflet, "Deformation-induced nanocrystal precipitation in Al-base metallic glasses," *Materials Transactions*, **42**, 1741-1747 (2001).

[38] J. J. Kim, Y. Choi, S. Suresh, and A. S. Argon, "Nanocrystallization during nanoindentation of a bulk amorphous metal alloy at room temperature," *Science*, **295**, 654-657 (2002).

[39] W. H. Jiang, F. E. Pinkerton, and M. Atzmon, "Deformation-induced nanocrystallization in an Al-based amorphous alloy at a subambient temperature," *Scripta Materialia*, **48**, 1195-1200 (2003).

[40] M. Heggen, F. Spaepen, and M. Feuerbacher, "Plastic deformation of $Pd_{41}Ni_{10}Cu_{29}P_{20}$ bulk metallic glass," *Materials Science and Engineering a-Structural Materials Properties Microstructure and Processing*, **375-77**, 1186-1190 (2004).

[41] M. Heggen, F. Spaepen, and M. Feuerbacher, "Creation and annihilation of free volume during homogeneous flow of a metallic glass," *Journal of Applied Physics*, **97**, 033506, (2005).

[42] T. G. Nieh, T. Mukai, C. T. Liu, and J. Wadsworth, "Superplastic behavior of a $Zr_{10}Al_5Ti_{17.9}Cu_{14.6}Ni_{52.5}$ metallic glass in the supercooled liquid region," *Scripta Materialia*, **40**, 1021-1027 (1999).

[43] T. G. Nieh, J. Wadsworth, C. T. Liu, G. E. Ice, and K. S. Chung, "Extended plasticity in the supercooled liquid region of bulk metallic glasses," *Materials Transactions*, **42**, 613-618 (2001).

[44] S. Schneider, P. Thiyagarajan, and W. L. Johnson, "Formation of nanocrystals based on decomposition in the amorphous $Zr_{41.2}Ti_{13.8}Cu_{12.5}Ni_{10.0}Be_{22.5}$ alloy," *Applied Physics Letters*, **68**, 493-495 (1996).

[45] R. Busch, S. Schneider, A. Peker, and W. L. Johnson, "Decomposition and Primary Crystallization in Undercooled $Zr_{41.2}Ti_{13.8}Cu_{12.5}Ni_{10.0}Be_{22.5}$ Melts," *Applied Physics Letters*, **67**, 1544-1546 (1995).

[46] K. F. Kelton, T. K. Croat, A. K. Gangopadhyay, L. Q. Xing, A. L. Greer, M. Weyland, X. Li, and K. Rajan, "Mechanisms for nanocrystal formations in metallic glasses," *Journal of Non-Crystalline Solids*, **317**, 71-77 (2003).

[47] H. Kato, Y. Kawamura, H. S. Chen, and A. Inoue, "A fictive stress model calculation of nonlinear viscoelastic behaviors in a Zr-based glassy alloy: Stress growth and relaxation," *Japanese Journal of Applied Physics Part 1-Regular Papers Short Notes & Review Papers*, **39**, 5184-5187 (2000).

[48] H. S. Chen, H. Kato, and A. Inoue, "A fictive stress model calculation of stress-overshoot: A nonlinear viscoelastic behavior in metallic glass," *Japanese Journal of Applied Physics Part 1-Regular Papers Short Notes & Review Papers*, **39**, 1808-1811 (2000).

[49] H. Kato, Y. Kawamura, A. Inoue, and H. S. Chen, "Newtonian to non-Newtonian master flow curves of a bulk glass alloy Pd40Ni10Cu30P20," *Applied Physics Letters*, **73**, 3665-3667 (1998).

[50] T. G. Nieh and J. Wadsworth, "Homogeneous deformation of bulk metallic glasses," *Scripta Materialia*, **54**, 387-392 (2006).

[51] R. Busch, Y. J. Kim, and W. L. Johnson, "Thermodynamics and Kinetics of the Undercooled Liquid and the Glass-Transition of the $Zr_{41.2}Ti_{13.8}Cu_{12.5}Ni_{10.0}Be_{22.5}$ Alloy," *Journal of Applied Physics*, **77**, 4039-4043 (1995).

[52] R. Busch, E. Bakke, and W. L. Johnson, "Viscosity of the supercooled liquid and relaxation at the glass transition of the $Zr_{46.75}Ti_{8.25}Cu_{7.5}Ni_{10}Be_{27.5}$ bulk metallic glass forming alloy," *Acta Materialia*, **46**, 4725-4732 (1998).

[53] Y. J. Kim, R. Busch, W. L. Johnson, A. J. Rulison, and W. K. Rhim, "Experimental determination of a time-temperature-transformation diagram of the undercooled $Zr_{41.2}Ti_{13.8}Cu_{12.5}Ni_{10.0}Be_{22.5}$ alloy using the containerless electrostatic levitation processing technique," *Applied Physics Letters*, **68**, 1057-1059 (1996).

[54] R. Busch and W. L. Johnson, "The kinetic glass transition of the Zr46.75Ti8.25Cu7.5Ni10Be27.5 bulk metallic glass former-supercooled liquids on a long time scale," *Applied Physics Letters*, **72**, 2695-2697 (1998).

[55] E. Bakke, R. Busch, and W. L. Johnson, "The Viscosity of the $Zr_{46.75}Ti_{8.25}Cu_{7.5}Ni_{10}Be_{27.5}$ Bulk Metallic-Glass Forming Alloy in the Supercooled Liquid," *Applied Physics Letters*, **67**, 3260-3262 (1995).

[56] A. Masuhr, R. Busch, and W. L. Johnson, "Thermodynamics and kinetics of the $Zr_{41.2}Ti_{13.8}Cu_{12.5}Ni_{10.0}Be_{22.5}$ bulk metallic glass forming liquid: glass formation from a strong," *Journal of Non-Crystalline Solids*, **252**, 566-571 (1999).

[57] J. Lu, "Mechanical behavior of a bulk metallic glass and its composite over a wide range of strain rates and temperatures," *Ph.D Thesis*. Pasadena: California Institute of Technology (2002).

[58] J. Markus and V. Zuluff, *Handbook of industrial electronic control circuits*, 1st ed. ed. New York: McGraw-Hill (1959).

[59] M. Yamasaki, S. Kagao, Y. Kawamura, and Y. K., "Thermal diffusivity and conductivity of supercooled liquid in $Zr_{41.2}Ti_{13.8}Cu_{12.5}Ni_{10.0}Be_{22.5}$ metallic glass," *Applied physics letters*, **84**, 4653-4655 (2004).

[60] M. Yamasaki, S. Kagao, and Y. Kawamura, "Thermal diffusivity and conductivity of $Zr_{55}Al_{10}Ni_5Cu_{30}$ bulk metallic glass," *Scripta materialia*, **53**, 63-67 (2005).

[61] M. Bletry, P. Guyot, Y. Brechet, J. J. Blandin, and J. L. Soubeyroux, "Homogeneous deformation of bulk metallic glasses in the super-cooled liquid state," *Materials Science and Engineering a-Structural Materials Properties Microstructure and Processing*, **387-89**, 1005-1011 (2004).

[62] K. Samwer, R. Busch, and W. L. Johnson, "Change of compressibility at the glass transition and Prigogine-Defay ratio in Zr-Ti-Cu-Ni-Be alloys," *Physical Review Letters*, **82**, 580-583 (1999).

[63] A. van den Beukel and J. Sietsma, "The Glass-Transition as a Free-Volume Related Kinetic Phenomenon," *Acta Metallurgica Et Materialia*, **38**, 383-389 (1990).

[64] Y. L. Gao, J. Shen, J. F. Sun, and G. Wang, "Crystallization of Zr-Al-Ni-Cu bulk amorphous alloy during continuous heating," *Rare Metal Materials and Engineering*, **32**, 518-521 (2003).

[65] J. F. Loffler and W. L. Johnson, "Model for decomposition and nanocrystallization of deeply undercooled $Zr_{41.2}Ti_{13.8}Cu_{12.5}Ni_{10.0}Be_{22.5}$," *Applied Physics Letters*, **76**, 3394-3396, (2000).

Chapter 3

Deformation and Viscosity of the Bulk Metallic Glass $Zr_{47.4}Ti_{8.0}Cu_{7.3}Ni_{9.8}Be_{27.5}$ in Supercooled Liquid State

Abstract

Compressive deformation at constant strain rates has been utilized in this study as an effective and accurate method to characterize the viscosity of bulk metallic glasses in their supercooled liquid regimes, particularly near the glass transition temperature. In this investigation, uniaxial compression tests were performed on a newly developed Zr- based alloy (Vitreloy 4' or Vit 4') at temperatures in its supercooled liquid region and various constant strain rates. A deformation map for the alloy was constructed, and the Newtonian and non-Newtonian viscosities were determined. These viscosities were fit with the recently developed Cooperative Shear Model. Acoustic (shear) wave speed measurements were performed on deformed and quenched specimens to obtain the shear modulus of the deformed material. The Cooperative Shear Model was able to capture the essential features of the deformation of the alloy. The model predictions for the shear modulus computed from the dynamic viscosity were also in good agreement with the experimentally determined values.

Key words: Bulk metallic glass; Newtonian and non-Newtonian flow; Viscosity; Shear modulus; Cooperative Shear Model

3.1 Introduction

Metallic glasses are a relatively new class of materials and were first discovered by rapid quenching of binary metallic alloy melts at very high cooling rates (approximately $10^6 K\ s^{-1}$) in 1960 at Caltech by Duwez and his coworkers [1]. Good glass forming alloy systems feature a low eutectic point and a large supercooled liquid region, which result in lower cooling rates facilitating the formation of metallic glasses in bulk form, i.e., thickness>1 mm [2]. Development of bulk metallic glasses (BMGs) in recent years is associated with the discovery of good glass forming compositions such as La-Al-Ni [3], Mg-Cu-Y [4], Zr-Ni-Al-Cu [5], Zr-Ti-Cu-Ni-Be [6], and Cu-Zr-Ti-Ni [7]. The Zr-Ti-Cu-Ni-Be system is among the best glass forming alloy systems discovered thus far. Lower critical cooling rates (1-10 K/s) in these compositions result in larger sizes (thickness) of quenched specimens and therefore make BMGs attractive candidates for potential structural applications.

The structure of amorphous alloys differs from that of conventional crystalline metals in that there are no pronounced short-range orders among atoms of amorphous alloys. The atoms of different elements are packed in a way that they are kinetically constrained, or frozen, during the rapid quenching process. At room temperature, the amorphous structure of the metallic glasses is in a metastable phase which can evolve to equilibrium phase(s) under externally imposed conditions such as thermal annealing or deformation due to stress [8, 9]. Unlike the well characterized crystalline metals and their alloys, the details of the atomic interaction and the subsequent deformation mechanisms in amorphous metals are still subjects of investigation.

A hypothesis on the existence of free volume in glassy materials was first proposed by Turnbull and Cohen [10] and was subsequently adapted for metallic glasses by Spaepen [11]. It is suggested that during the rapid quenching there are “holes” or “voids” of various sizes frozen into the amorphous structure, which are collectively defined as “free volume” and suspected as the key to the diffusive arrangement of atoms. The possibility of an atom jumping into an adjacent hole (free volume) is dependent on the relative size of the atom and the hole. Free volume is generally a decreasing function of temperature. When the temperature is increased to a critical temperature, i.e., the glass transition temperature, the motion of the free volume is activated and more active relaxation process starts with the free volume diffusion.

Free volume is considered to be pressure dependent in metallic glasses [12]. However, shear component of the deformation also plays a more important role in the general deformation of the glass including shear localization and failure. The flow rule proposed by Spaepen [11] addressed the free volume variation due to applied shear stress and shearing rate. It is also generally believed that small variations in local free volume lead to strain localization during deformation. Spaepen’s free volume model has become the most widely accepted in demonstrating the physics of deformation in metallic glasses and for studying shear localization in these materials as a failure mechanism.

Extensive efforts have been made to prove or demonstrate the existence of free volume in BMGs. Duine *et al.* used the free volume based viscosity and defect evolution assumption to analyze the kinetic process of defects and their steady state concentration [13]. de Hey *et al.* associated quantitatively the specific heat capacity change at glass transition observed in differential scanning calorimetry (DSC) with the amount of free volume in the material prior to performing the measurement [14-16]. In contrast, Johnson *et al.* derived the specific heat capacity change at glass transition from enthalpy evolution without any assumption regarding the existence of free volume [17]. A TEM study by Spaepen’s group suggested the existence of nano-scale defects in the vicinity of shear bands using an optical image processing method [18]. It was found that though Spaepen’s model was able to describe the evolution of strain localization due to local variations in free volume, the experimental data for a Zr-based metallic glass in the homogeneous deformation region could not be adequately reproduced with this model [19]. The homogeneous deformation data was amenable to description by a phenomenological fictive stress model which does not involve the concept of free volume [20].

Recently, Langer *et al.* [21] proposed a shear-transformation-zone (STZ) theory that describes the deformation of metallic glasses with a set of equations of motion analogous to the Navier-Stokes equations of fluid dynamics. The equations of motion include evolution of STZ density besides the development of deformation rate and stress equilibrium, with an effective disorder temperature as the dynamic state variable. In the STZ model, a cluster of atoms instead of a single atom (free volume) is treated as a "deformation unit" that transforms into or out of an activated zone during the deformation.

Adapting the idea of shearing clusters, i.e., STZ, Johnson and Samwer [22] proposed a Cooperative Shear Model (CSM) that describes the atoms in amorphous alloys conglomerating into clusters of about 100 atoms each and deforming under a shearing dominant manner in the unit of the atom clusters. The shearing clusters have their potential energy landscape over different atomic configurations. The potential energy landscape for a many-particle system was described as ensemble of basins, peaks, and saddle points in multidimensional configurational space as proposed by Stillinger [23], Davis *et al.* [24], and Heuer [25] among others. Based on this topological point of view of potential energy of the glassy material, the CSM [22] postulates a simple scaling law to predict the temperature dependent critical shear stress of bulk metallic glasses. The key variable in CSM is the shear modulus of the unstressed glass, G, which in this model is not an elastic constant but a statistical parameter that varies with local distribution of the configurational energy. The measured G at certain temperature and stress is, therefore, the statistical average over the distributed configurations and the measurement time scale. Such a cooperative shear model explains the widely observed intrinsic local heterogeneity in amorphous structures [26]. A recent study found the correlation between the annealing temperature and change of shear modulus of Vitreloy 4 after annealing at that temperature, which could be quantitatively explained by CSM [27].

In this investigation, compression tests were performed on a newly developed Zr- based alloy at temperatures in its supercooled liquid regime and with various constant strain rates. A deformation map for the alloy was constructed, and the Newtonian and non-Newtonian viscosity was computed and was fitted with the cooperative shear model in a self-consistent manner. Acoustic (longitudinal and shear) wave speed measurements were performed on deformed and quenched specimens to obtain the shear modulus of the stressed material. The cooperative shear model was able to capture the essential features of the deformation of the alloy. The model predictions for shear modulus computed from the dynamic viscosity were also in good agreement with the experimentally determined values.

3.2 Experimental

3.2.1 Material and specimen preparation

The $Zr_{47.4}Ti_{8.0}Cu_{7.3}Ni_{9.8}Be_{27.5}$ bulk metallic glass was prepared from a mixture of the elemental metals of purity ranging from 99.5 to 99.9% by induction melting and subsequent water quenching in a 6.35 mm diameter silica tube. The newly developed bulk metallic glass is referred to as Vitreloy 4', or Vit 4', because of the closeness of its chemical composition to that of the well established alloy, Vitreloy 4 or Vit 4 ($Zr_{46.75}Ti_{8.25}Cu_{7.5}Ni_{10}Be_{27.5}$). The as-quenched material was broken into small fragments and injection cast to amorphous rods in copper moulds. Cylindrical specimens of two sizes were prepared. The smaller specimen was cast as 4 mm in diameter and cut to 6 mm in length, and the larger specimen was cast as 6 mm in diameter and cut to 8.5-9 mm in length. The top and bottom surfaces of all specimens were polished with 600-grit sandpapers. During the compression test, high temperature Bentone-Clay semi-synthetic grease was applied on both surfaces to reduce the effect of friction.

Differential scanning calorimetry (DSC) study of the as-prepared material revealed that the temperatures at the onset of the glass transition (T_g) and the temperature at the onset of the first crystallization (T_{x1}) to be $615 K$ and $733 K$, respectively, when subjecting to a constant heating rate of $20\ K/\min$ (see Fig. 3.1). Due to the slight composition difference (as compared to

Vitreloy 4, $Zr_{46.75}Ti_{8.25}Cu_{7.5}Ni_{10}Be_{27.5}$), the material has a slightly smaller supercooled liquid region ($\Delta T = T_x - T_g = 118K$) as compared to that of Vitreloy 4 (Vit 4), which has a $\Delta T = 123\,K$ [28]. Also, it does not have the spinodal phase separation as evident from its absence in the DSC trace of Vit 1 (see the discussion in Chapter 2). Therefore, the thermodynamical stability of the new material $Zr_{47.4}Ti_{8.0}Cu_{7.3}Ni_{9.8}Be_{27.5}$ (Vit 4') is superior to that of Vit 1 and close to Vit 4. By using $Zr_{47.4}Ti_{8.0}Cu_{7.3}Ni_{9.8}Be_{27.5}$ instead of Vit 1, the issues such as phase separation and nano-crystallization during high temperature compression tests can be minimized. For convenience, we denote the material as Vitreloy 4', or Vit 4', later in the discussion.

The density of Vit 4' was measured to be $5.935 \pm 0.020 g/cm^3$ according to the ASTM standard on density measurement by buoyancy [29]. The variation of the density arises from the different concentration level of voids in the quenched material.

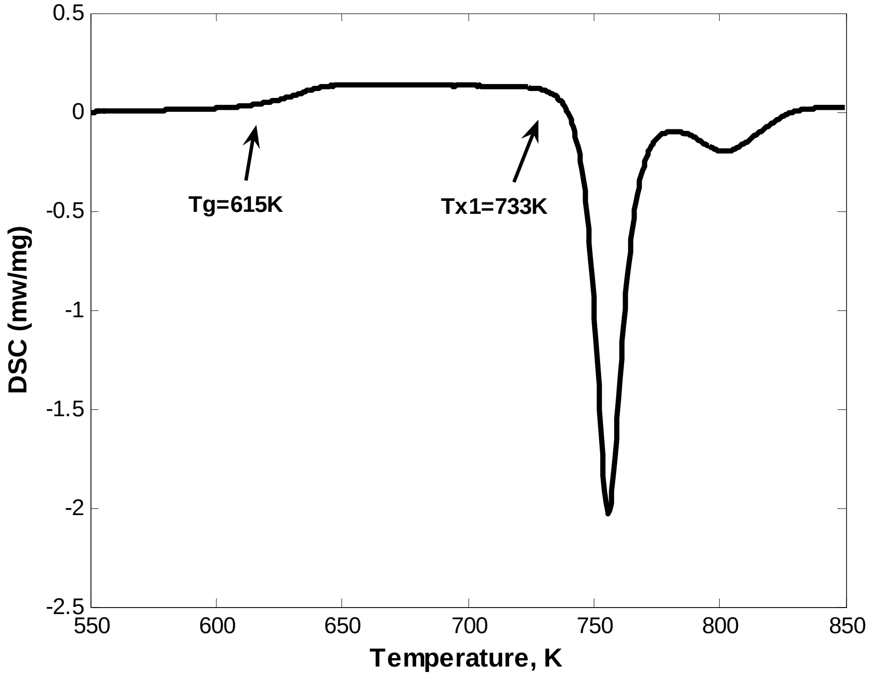

Fig.3.1 Differential scanning calorimetry (DSC) trace of the as-prepared Vit 4'.

3.2.2 High temperature deformation

For the purpose of studying the plastic flow behavior of Vit 4' in its supercooled liquid state, the testing temperatures are chosen to be in the vicinity of its glass transition temperature, $T_g = 615K$. All the experiments were conducted under uniaxial compressive stress condition, with the strain rates varying in the range of $10^{-5} - 10^{-1}\ s^{-1}$. All three deformation modes (shear localization, non Newtonian and Newtonian) were covered by the experimental conditions chosen for the study.

Quasi-static uniaxial compression tests were carried out using a servo-hydraulic Materials Testing System (MTS 358 series) with multiple 5-kip/20-kip/50-kip load cartridges and a 5-inch displacement cartridge. The compression test fixture was adopted from the design of Lu [30, 31], including a loading frame with features to accommodate a split electric furnace, a Linear Variable Differential Transducer (LVDT) and its conditioner for displacement measurement, and a set of furnaces with a temperature feedback/control system. For a detailed design of the apparatus, the reader is referred to Figure 1 in Chapter 2 and accompanying description of Lu [30, 31]. Small modifications, such as increasing the thickness of the plates that connect the extension rods and filling insulating materials in the furnace chamber, were made on the apparatus to improve the insulation and to minimize thermal flux during the tests.

Two sets of measurements were performed on the newly processed metallic glass, Vit 4'. The smaller specimens were used to generate a flow map covering various strain rates and a temperature region around its supercooled liquid state. Four temperatures were selected for testing: $583K$, $603K$, $623K$, and $643\ K$. At each temperature, four to five compression tests at strain rates varying from $10^{-3} s^{-1}$ to $10^{-5} s^{-1}$ were conducted. The larger specimens were used to perform the compressive tests at $583\ K$ with different strain rates. After each test, the bigger specimen was immediately taken out of the furnace and quenched in cold water. Acoustic measurements were performed on the quenched compression specimens subsequently to obtain the shear moduli of the deformed specimens.

To avoid crystallization in the specimens, the strain rate and the overall strain of each test were designed such that the total loading time plus the heating time prior to the loading did not exceed the crystallization time limit at this temperature. Since a complete time-temperature-transformation diagram was not available for this composition, the time-temperature-transformation diagram of Vit 1 was taken as a reference [32, 33], which provided a conservative estimate (see Fig. 3.2).

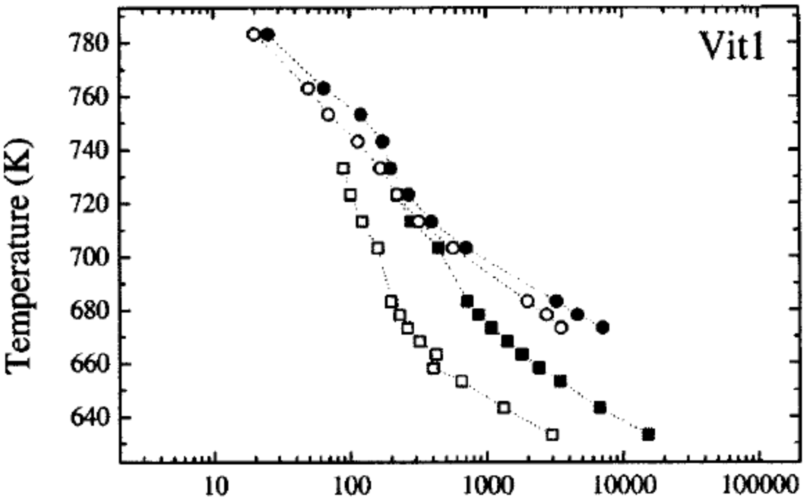

Fig.3.2 Time-temperature-transformation diagram of Vitreloy 1 (Reproduced from Waniuk *et al.* [33]) .

3.2.3 Acoustic measurement of mechanical modulus

Dynamic stress disturbances propagate in solids in the form of longitudinal and shear waves, each at a characteristic wave speed, which are functions of material properties. The longitudinal and the shear wave speed in an isotropic elastic solid can be expressed in terms of its elastic moduli as [34]

$$v_l = \sqrt{(\lambda + 2G)/\rho}$$
$$v_s = \sqrt{G/\rho}\ , \tag{3.1}$$

where v_l is the longitudinal wave speed, v_s is the shear wave speed, λ and G are elastic moduli known as the Lamé constants, and ρ is the density of the material. The Lamé constant G is also called the shear modulus of the material.

The Lamé constants of a solid can be expressed in terms of its Young's modulus (E) and its Poisson's ratio (ν) by

$$\lambda = \frac{\nu E}{(1+\nu)(1-2\nu)}$$
$$G = \frac{E}{2(1+\nu)}\ . \tag{3.2}$$

From (3.1) and (3.2), one can compute the elastic moduli of interest (E and G), the Poisson's ratio (ν) from the wave speeds (V_l, V_s) and the mass density ρ, which is measured independently:

$$G = \rho(V_s)^2$$
$$E = \rho(V_s)^2 \frac{3(V_l/V_s)^2 - 4}{(V_l/V_s)^2 - 1}$$
$$\nu = \frac{E}{2G} - 1 = \frac{(V_l/V_s)^2 - 2}{2(V_l/V_s)^2 - 2}\ . \tag{3.3}$$

The 6-mm-diameter specimens used in the compression tests were cleaned in an ultrasonic bath, and then the length of the each specimen was measured with a digital caliper with an accuracy of 1/1000". The surfaces of the test samples for acoustic characterization should be flat and smooth to permit clean pulse-echo measurement of the sound transit time through a section of known thickness. Usually, the specimens after a high temperature compressive test and cleaning satisfy this requirement and do not need further polishing. In some cases, however, it was necessary to polish the surfaces with 1200-grit sand paper to make them smooth and parallel. The diameter of the cross-section must exceed about five wavelengths to minimize the noise from boundary reflections. In most metallic alloys, the wave length for a 5 MHz signal (typical of ultrasonic transducers) can be estimated as around $1\,mm$, which means that the diameter of the sample should be larger than $5\,mm$. Hence, the larger 6 *mm* diameter specimens were used for determining wave speeds.

A Parametrics model# 5052UA Ultrasonic Analyzer working in the reflection mode was used for making the wave speed measurements. A shear transducer and an oscilloscope were employed for the measurements. When a shear wave signal is sent from one end of the specimen, the transducer measures the round trip transit time of the shear wave from the same end. The oscilloscope was used to record the transit time. The shear wave speeds can be computed from

$$V_s = 2L / t_{2L}^s , \qquad (3.4)$$

where L is the length of the specimen and t_{2L} is the round-trip transit time of the ultrasonic signal. Therefore, using the first formula in Eq. (3.3), the shear modulus can be calculated directly.

The density of the material was measured by the hydrostatic weighing technique [29]. The wave speed measurements were repeated several times on each specimen, and the average values were taken to compute the elastic moduli.

3.3 Results

3.3.1 Stress-strain response

The true stress-strain curves of Vit 4’ obtained from uniaxial compression tests are plotted in Fig. 3.3. The material exhibits flow behavior very similar to that of Vit 1 [19]. At T=$583\,K$, which is below the glass transition temperature ($T_g = 615K$), its flow stress shows very little strain rate sensitivity. With the strain rate increasing from $7.2\times10^{-5}s^{-1}$ to $2.3\times10^{-4}s^{-1}$ (by a factor of ~30), the flow stress increases less than 15%. Increasing the strain rate further to the order of $10^{-3}s^{-1}$, the specimen fails in a brittle manner right after reaching the elastic limit. With increasing temperature, the material shows larger strain rate sensitivity and deforms mostly in homogeneous flow mode, even the strain rate increases to the order of $10^{-2}s^{-1}$.

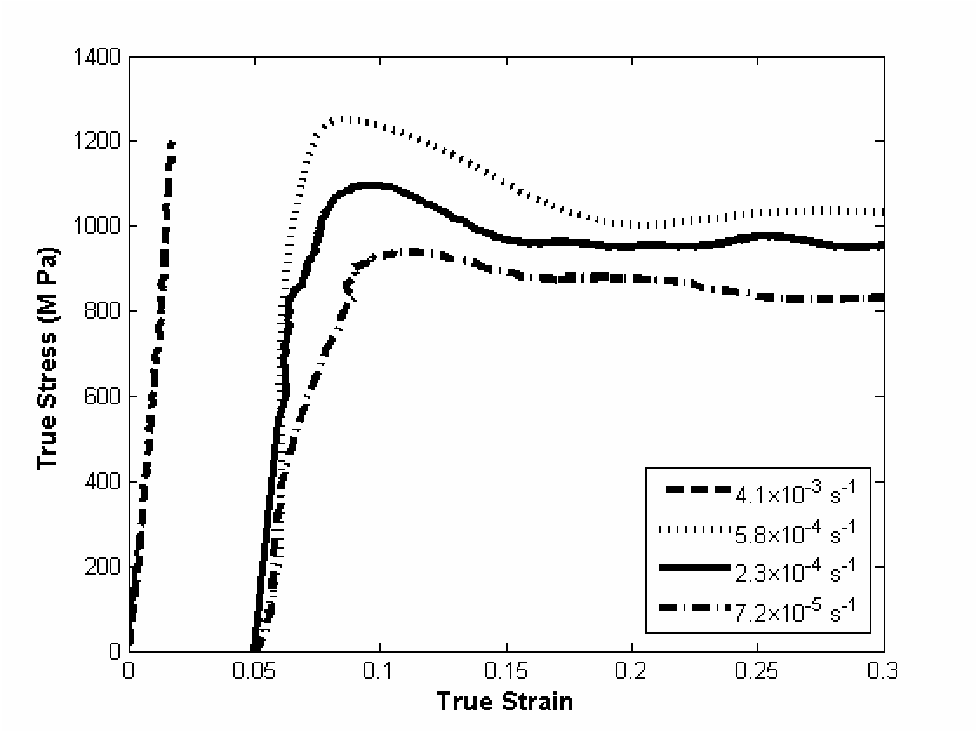

(a)

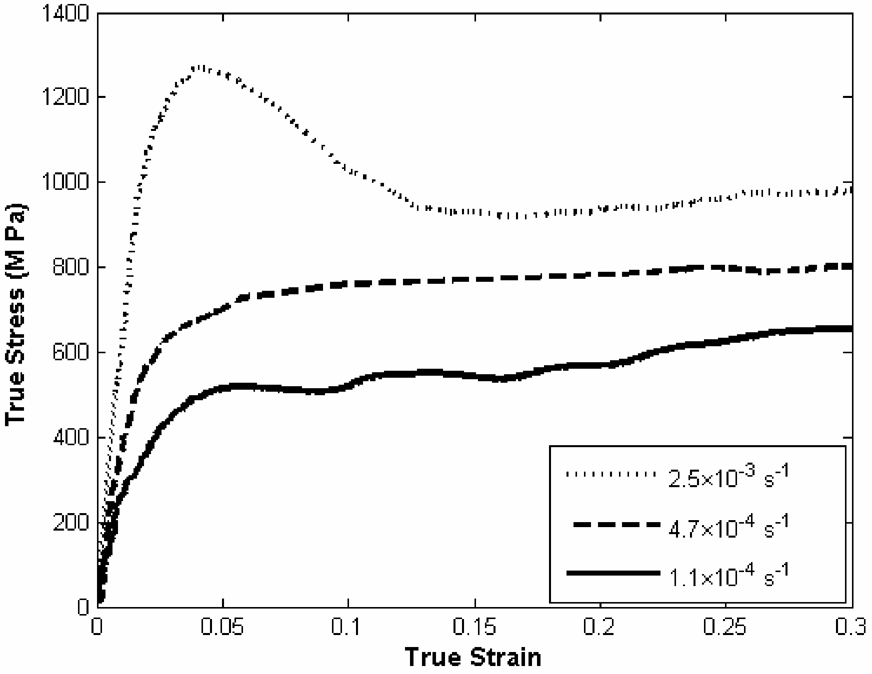
1400
1200
1000
800
600
400
200
0
True Stress (M Pa)
0
0.05
0.1
0.15
0.2
0.25
0.3
True Strain
2.5×10⁻³ s⁻¹
4.7×10⁻⁴ s⁻¹
1.1×10⁻⁴ s⁻¹

(b)

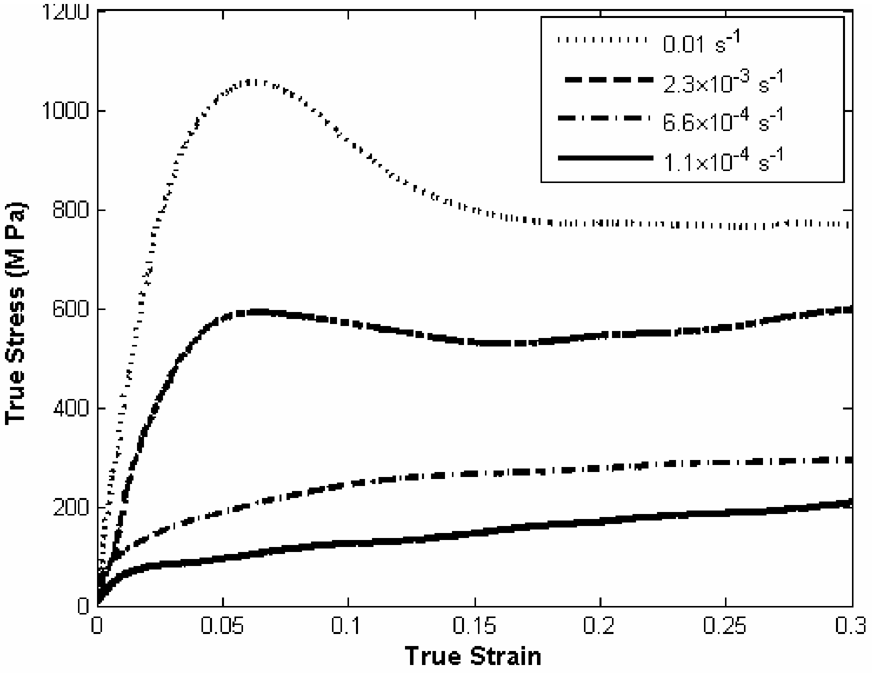
1200
1000
800
600
400
200
0
True Stress (M Pa)
0
0.05
0.1
0.15
0.2
0.25
0.3
True Strain
0.01 s⁻¹
2.3×10⁻³ s⁻¹
6.6×10⁻⁴ s⁻¹
1.1×10⁻⁴ s⁻¹

(c)

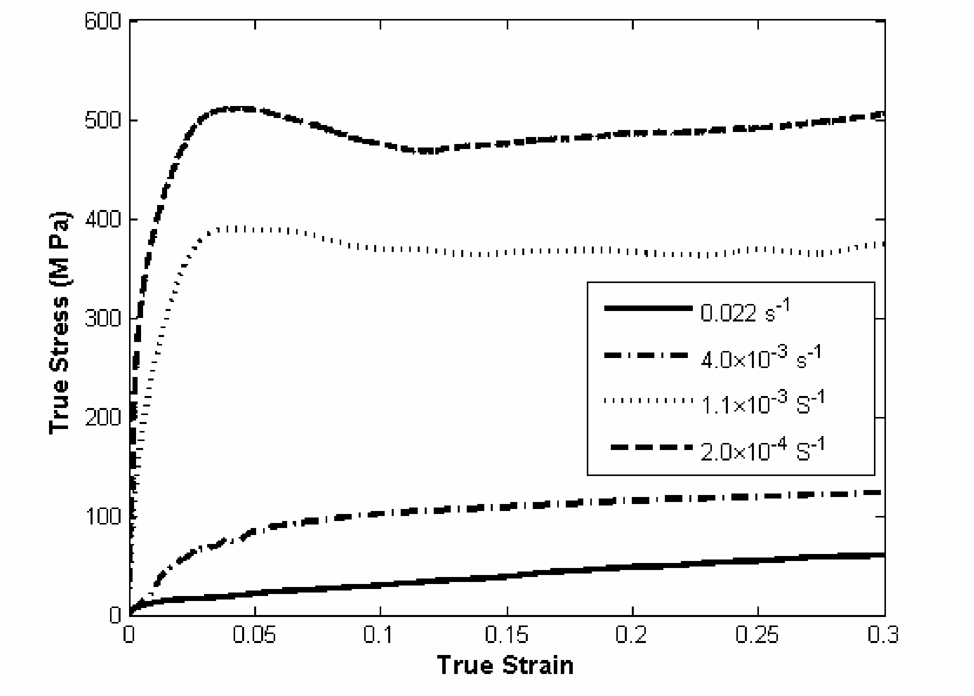

(d)

Fig.3.3 True stress-strain curves of Vit 4' in uniaxial compression at various temperatures and strain rates: (a) T = 583 K, the curves are shifted along the coordinate of true strain for display purposes; (b) T = 603 K; (c) T = 623 K; (d) T = 643 K. The strain rates are indicated in the legend.

3.3.2 Deformation at $T = 583\,K$ and wave speed measurements

Compression tests were performed at various strain rates at $T = 583\,K$ on the 6 *mm* diameter specimens. The specimens were quenched in cold water immediately after the high temperature deformation. They were then cleaned, and wave speed measurements were performed on them. The relaxation time of the material at $T = 583\,K$ can be estimated from $\tau_t = \eta_e / G$, where η_e is the Newtonian viscosity and G is the shear modulus of the unstressed material. This estimation for Vit 1 at $T = 583\,K$ yields about 30 seconds, with its viscosity taken as $10^{12}\,Pa\cdot s$ [35] and shear modulus taken as $34\,GPa$ [19]. By quenching the specimen immediately after compression within its relaxation time, the thermodynamic configuration of the glass is frozen in its supercooled liquid state. Therefore, the elastic moduli of the quenched specimens are a reflection of the supercooled liquid state (frozen state). When the testing temperature becomes higher, the relaxation time becomes so short that it becomes impractical to quench the specimen in laboratory conditions to recover its frozen structure. Hence, this type of measurement was only performed at $T = 583\,K$. Moreover, at this temperature, the chance that the material undergoes phase separation or nanocrystallization, which can influence the accurate viscosity measurements, is much lower at this temperature than at higher temperatures.

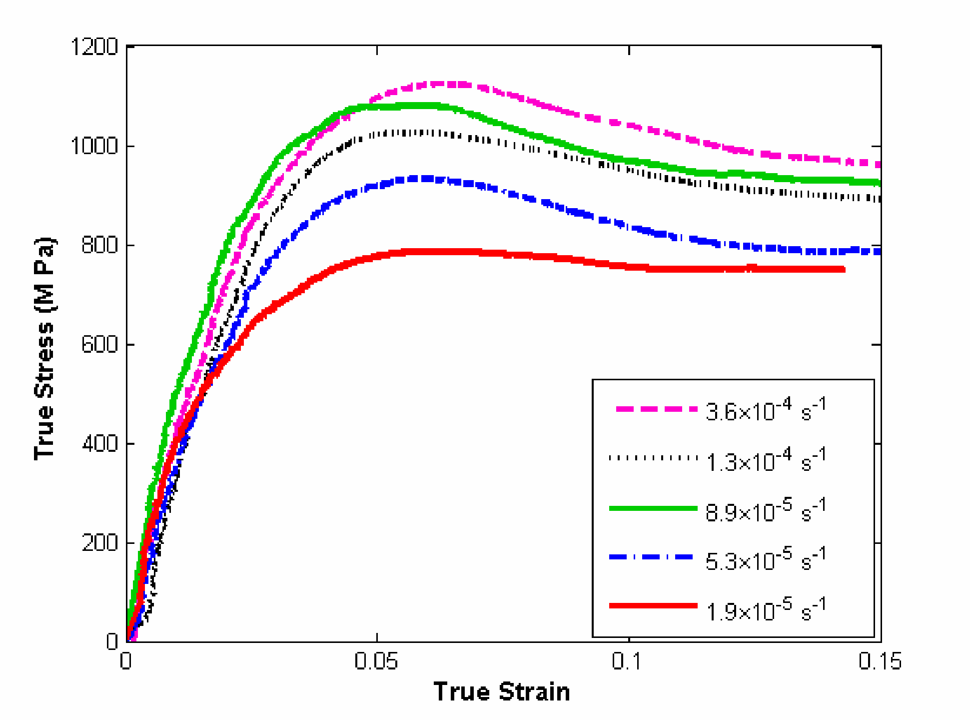

Fig.3.4 Compressional stress-strain curves of Vit 4' at $T = 583K$ and various strain rates.

Figure 3.4 shows the stress-strain curves of the tests performed at 583 K at different strain rates. The material is nearly strain rate insensitive in terms of flow stress, an observation made in connection with Fig. 3.3(a). Even though the strain rate increases by an order of magnitude, the steady state stress changes only from 800 MPa to 1000 MPa, which is probably the limiting strength of this material in supercooled liquid state. Higher strain rates will most likely result in brittle failure due to shear localization (Fig. 3.3(a)).

The shear modulus of each of the specimen after deformation was calculated from ultrasonically measured wave speeds by using Eq. (3.2). The shear modulus (*G*) of specimens tested at $\dot{\varepsilon} = 5.3\times10^{-5} s^{-1}$, $\dot{\varepsilon} = 8.9\times10^{-5} s^{-1}$, and $\dot{\varepsilon} = 1.3\times10^{-4} s^{-1}$ were found to be 36.39 ± 0.09 GPa, 35.84 ± 0.09 GPa, and 35.06 ± 0.08 GPa, respectively.

3.4 Analysis and Discussion

3.4.1 Cooperative Shear Model (CSM)

Due to the lack of long-range order, the atoms in amorphous alloys tend to relax and break the metastable state of the material under favorable thermo-mechanical conditions. To illustrate the manner of the arrangement of the unstructured atoms and their motions, Johnson and Samwer [22] recently proposed a Cooperative Shear Model (CSM) that describes the atoms in amorphous alloys conglomerating into clusters of about 100 atoms each, and deforming in a shear dominant manner in the unit of the atom clusters. The shearing clusters, each at a different potential energy state, thus form a potential energy landscape over different atomic configurations. The potential energy landscape for a many-particle system was described as an ensemble of basins, peaks, and saddle points in multimensional configurational space by Stillinger [23]. Buchner and Heuer wrote the partition function and derived related thermodynamic parameters for a model glass former based on this topological point of view of potential energy of glassy material [36]. The CSM is the first model to correlate the thermodynamical inner states of amorphous materials to their macroscopic mechanical properties such as shearing viscosity and shear modulus, which are experimentally measurable variables and can provide the validation of the model.

Following the theory proposed in [22], the relation between potential energy density and shear strain applied on an atom cluster is postulated as

$$\Phi(\gamma) = \Phi_o / 2[1 - \cos(\pi\gamma / 2\gamma_c)] = \Phi_o \sin^2(\pi\gamma / 4\gamma_c)\,, \qquad (3.5)$$

where Φ_o is the total barrier of the energy density and γ_c is defined as the yield strain. The potential energy density has minima of $\Phi(\gamma) = 0$ at $\gamma = 0$, and barriers at $\gamma = 2\gamma_c$ (see Fig. 3.5).

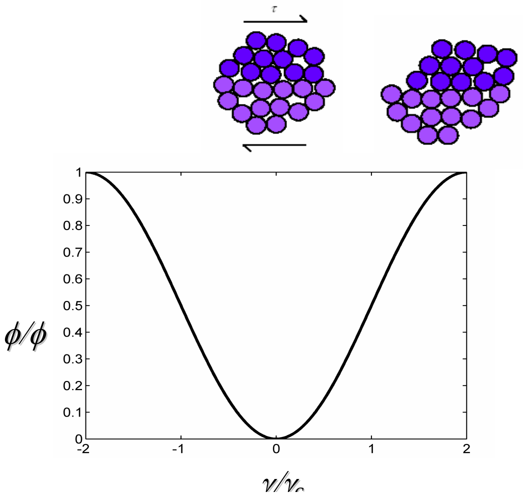

Fig.3.5 A model of the potential energy density of an atom cluster in amorphous alloys. Upon shearing, the cluster has a tendency to jump to a state with higher potential energy.

Assuming that shear is the dominant deformation mode of metallic glasses, the shear modulus of the unstressed solid can then be expressed as

$$G = \left.\frac{d^2\Phi}{d\gamma^2}\right|_{\gamma=0} = \frac{\pi^2}{8\gamma_c^2}\Phi_o . \qquad (3.6)$$

Now, instead of being an elastic constant (the shear modulus), G of metallic glass becomes a thermodynamic variable that fluctuates with different potential energy configurations. The measured G at a certain temperature and stress condition is a statistical average of the distributed local shear moduli, G.

From (3.6),

$$\Phi_o = \frac{8}{\pi^2} G\gamma_c^2 . \qquad (3.6)’$$

Therefore, if the effective size of a cluster is Ω, the potential energy barrier W_o of an atom cluster in an unstressed amorphous solids can be expressed as

$$W_o = W(\gamma = 0) = \Omega \cdot \Phi_o = \alpha (G / G_c)\,, \tag{3.7}$$

where $\alpha = \dfrac{8}{\pi^2} \Omega G_c \gamma_c^2$.

At a finite temperature T and applied shear stress τ, strain fluctuations will carry the system over the barrier $W(\tau)$. With a frequency ω_o of attempted fluctuation, the macroscopic variable, shearing rate, can be expressed in terms of thermodynamic parameters:

$$\dot{\gamma} = \omega_o \exp(-W_o / \kappa T) = \omega_o \exp\left[-(\alpha / \kappa T)(G / G_c)\right]. \tag{3.8}$$

For a simple Maxwell model of viscoelastic behavior of a liquid, the shearing viscosity η can be scaled with the shear strain rate as

$$\frac{\dot{\gamma}}{\omega_o} = \frac{\eta_\infty}{\eta}\,, \tag{3.9}$$

where η_∞ is the limiting viscosity when the shear strain rate reaches infinity.

Using (3.8) and (3.9), the normalized viscosity can be written as

$$\frac{\eta}{\eta_\infty} = \exp\left[(\alpha / kT) \frac{G}{G_c}\right]. \tag{3.10}$$

The equilibrium (unstressed) shear modulus G_e is postulated to have an exponential relationship with temperature [27]:

$$\frac{G_e}{G_c} = \exp\left(-\frac{T}{T_w}\right). \tag{3.11}$$

Therefore, by fitting T_w and α to Eq. (3.10) and Eq. (3.11), one can find the relationship between the Newtonian viscosity, η, and the temperature, T.

The Newtonian viscosities of two amorphous alloys were computed with CSM. $Pd_{43}Ni_{10}Cu_{27}P_{20}$ amorphous alloy measured with three-point beam bending tests and parallel-plate rheometry method [37] are plotted in Fig. 3.6 along with fits suggested by various models. The shearing viscosity from the uniaxial compressive tests are deduced as one-third of the ratio of the steady state stress to the corresponding uniaxial strain rate following Scherer [38]. The comparison among fittings of Vogel-Tammann-Fulcher model [39, 40], Cohen-Grest free volume model [41] and the recently proposed cooperative shear model are shown. From Fig. 3.6, it can be seen that data from compressive tests fill the region of the data unexplored by Fan *et al.* [37] and suggest a smooth exponential trend from the three-point-beam-bending data at low temperature to parallel-plate- rheometry data at high temperature. All three models capture the trend of the Newtonian viscosities of the material with the temperature without a distinguishable difference. Experiments at even lower temperatures and strain rates, which take a very long time to attain equilibrium state, should be carried to determine the low temperature trend. The parameters of CSM (Eq. (3.10) and Eq. (3.11)) for $Pd_{43}Ni_{10}Cu_{27}P_{20}$ are $\alpha = 4.57\times10^{-18}\,J$ and $T_w = 200\,K$.

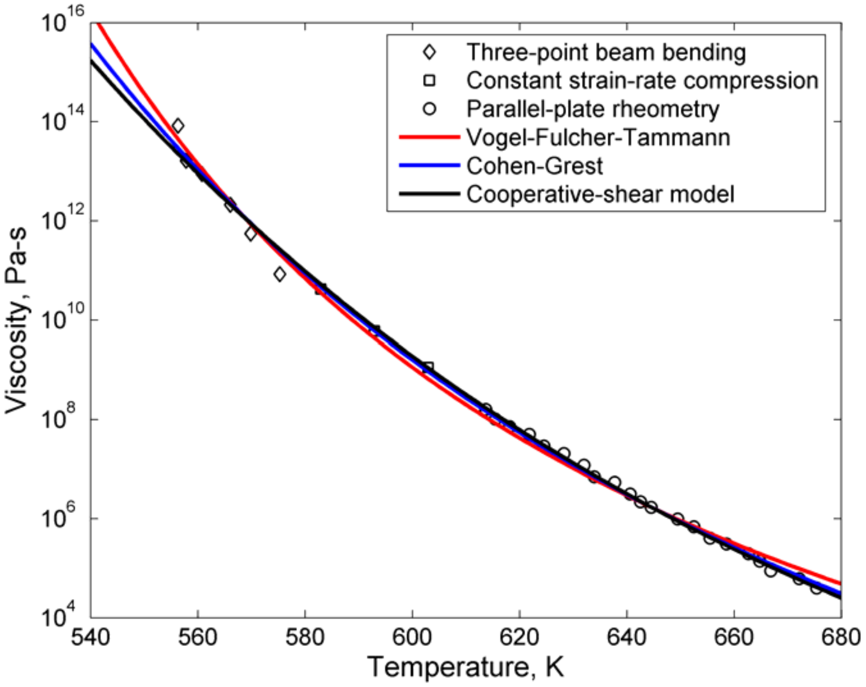

Fig.3.6 Various model fits of Newtonian viscosity data at different temperatures of $Pd_{43}Ni_{10}Cu_{27}P_{20}$ amorphous alloy. Three-point Beam bending and Parallel-plate rheometry data were taken from Ref. [37].

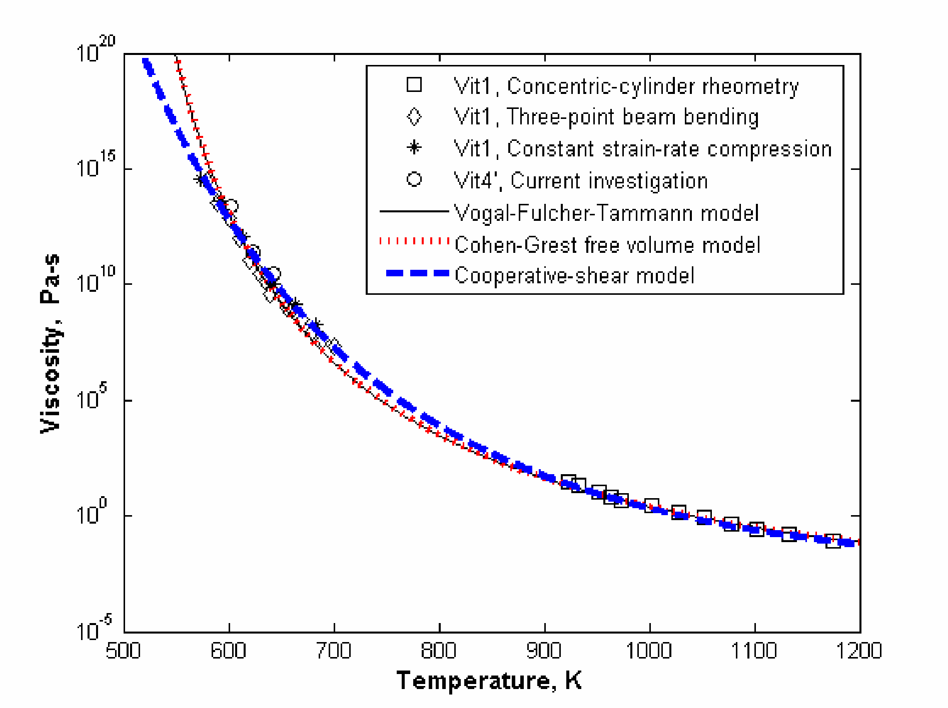

Fig.3.7 Various model fits of Newtonian viscosity data of Vit 4' (this investigation) and Vit 1 at different temperatures. The Vit 1 data were from Ref. [19] and [41].

The Newtonian viscosity at different temperatures Vit 4' is also computed from one thirds of the ratio of its Newtonian compressive flow stress to the strain rate. The data at temperatures lower than $603K$ was not obtained in the current compression experiments because it requires the tests to be conducted at very low strain rate to reach Newtonian flow, and the required testing time is thus too long for laboratory work. There are no other Newtonian viscosity data available in literature because this is a newly developed material. However, the strength of the material is found to be close to that of Vitreloy 1 in the supercooled liquid state. For comparison purposes, the results of the current investigation are plotted in the same Fig. 3.7 along with Newtonian viscosity data of Vit 1 from three-point beam bending test [41], concentric-cylinder rheometry [41], and constant strain-rate compression test by Lu et al. [19]. The Newtonian viscosity data of Vit 4' fall within the band of the other Vit 1 data in a consistent manner. Therefore, the CSM along with the Vogel-Tammann-Fulcher and the Cohen-Grest model is applied on the data of Vit 4' and Vit 1, and the results are shown in Fig. 3.7. The parameters of CSM (Eq. (3.10) and Eq. (3.11)) for Vit 4' and Vit 1 are $\alpha = 7.19 \times 10^{-19}\,J$ and $T_w = 347\ K$.

3.4.2 Non-Newtonian viscosity of Vit 4' with shear softening

Equation (3.10) is also valid for the non-Newtonian viscosity $\eta(\dot{\gamma}, T)$ with the shear modulus of the material in its non-equilibrium state, i.e., $G = G(\xi, T)$, where $\dot{\gamma}$ is the shear strain rate and $\dot{\xi}$ is the specific configurational potential energy of flow zones. For a non-equilibrium system, two variables are sufficient to determine its thermodynamical status. Therefore, the rate of softening of G can be formulated as

$$\frac{\partial G(\xi,T)}{\partial t} = \dot{\xi}\frac{\partial G}{\partial \xi}\bigg|_T \approx (\eta\dot{\gamma}^2)\frac{\partial G}{\partial \xi}\bigg|_T , \qquad (3.12)$$

where $\eta(G)\dot{\gamma}$ is the rate of change of specific configurational potential energy approximated by the rate of dissipated energy density, and $\frac{\partial G}{\partial \xi} = \frac{\partial G}{\partial T} / \frac{\partial \xi}{\partial T}$ is a dimensionless thermodynamic parameter denoting the change in shear modulus with respect to changes in specific configurational energy.

Configurational relaxation can be accounted for by adopting a uni-molecular kinetic model, $(G - G_e)/\beta\tau_M$, where G_e is the equilibrium shear modulus of the material which can be obtained from Eq. (3.11), $\tau_M = \eta(G)/G$ is the Maxwell relaxation time, and β is the parameter that accounts for the deviance of the model from the Maxwell relaxation. For steady state flow,

$$\frac{dG}{dt} = (\eta\dot{\gamma}^2)\left.\frac{\partial G}{\partial \xi}\right|_T - \frac{G - G_e}{\beta(\eta/G)} = 0. \qquad (3.13)$$

Therefore, combining Eqs. (3.10), (3.11), and (3.13), the transient non-Newtonian viscosity and non-equilibrium shear modulus can be solved in an implicit form with one parameter $\beta\left.\frac{\partial G}{\partial \xi}\right|_T$. To compare the predictions from the cooperative shear model and experimentally determined viscosities, the numerical solution of the implicit equations for the viscosities, Eqs. (3.10) and (3.13), are solved using the Newton-Raphson method [44]. The fitting of the viscosities of Vit 4' using the cooperative shear model is shown in Fig. 3.8. As can been seen from the figure, the cooperative shear model predictions capture the viscosity of the material over a wide range of temperatures and strain rates fairly well. The fitting parameter $\beta\left.\frac{\partial G}{\partial \xi}\right|_T$ is found to be $358.8 \pm 11.2 Pa/J$ when used together with the Newtonian fitting parameters from the last section, namely, $\alpha = 7.19 \times 10^{-19} J$ and $T_w = 347\ K$.

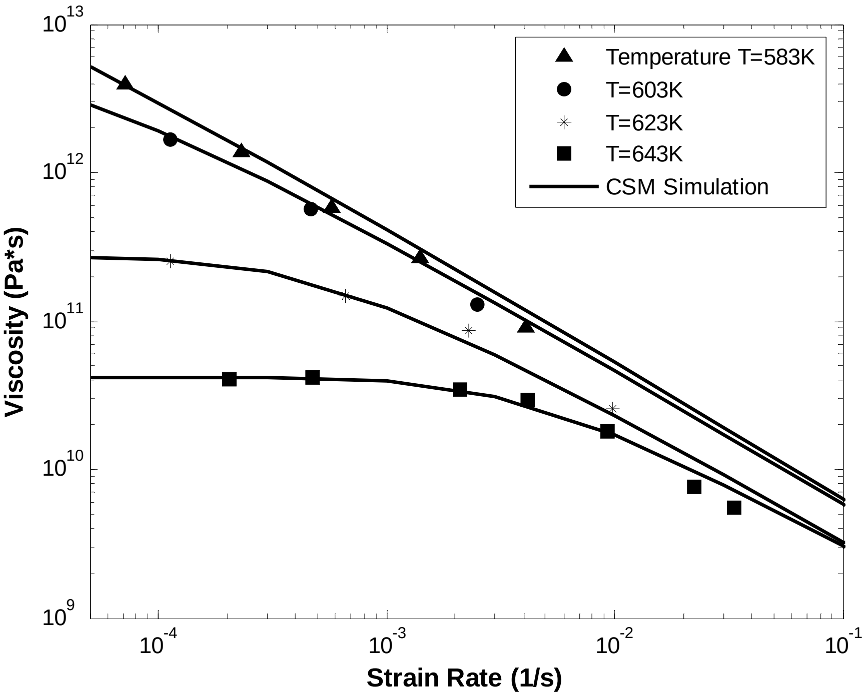

Fig.3.8 Non-Newtonian viscosity of Vit 4' deduced from the compression tests at various temperatures and strain rates. The solid lines are the numerical solutions of cooperative shear model predictions obtained using Newton-Raphson method. Symbols represent experimental data at various temperatures.

3.4.3 Wave speed measurement vs. strain rate

For the purpose of validating the relationship between the shear modulus of the stressed material and its viscosity under the same conditions, compression tests were performed on the 6-mm-diameter specimens at the temperature of $T = 583K$. From the stress-strain relation of the Zr-based amorphous alloy ($Zr_{47.4}Ti_{8.0}Cu_{7.3}Ni_{9.8}Be_{27.5}$), Vit 4' at 583 *K*, and different strain rates (Fig. 3.3), the shear viscosities can be deduced from the experimental data as one-third of the ratio of the steady state stress to the corresponding uniaxial strain rate [39] and are plotted in Fig. 3.9. Three specimens after compressive loading at $\dot{\varepsilon} = 5.3 \times 10^{-5} s^{-1}$, $\dot{\varepsilon} = 8.9 \times 10^{-5} s^{-1}$, and $\dot{\varepsilon} = 1.3 \times 10^{-4} s^{-1}$ were quenched and subjected to ultrasonic wave speed measurement. From Eq. (3.10), the shear modulus of the amorphous alloy can be deduced from their measured viscosities using the uniaxial compression tests. A comparison of the shear modulus directly measured from the quenched specimens using ultrasonic methods and that deduced from viscosity is shown in Fig. 3.10. They are in good agreement with the predictions from cooperative-shear model (CSM) presented in Eq. (3.8). It is worth noting a consistent trend of decreasing shear modulus with increasing strain rate.

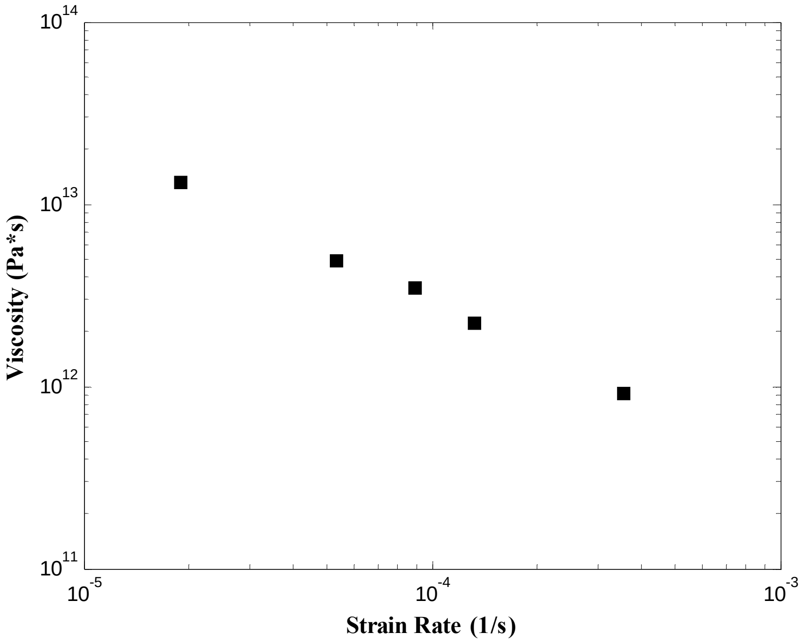

Fig.3.9 Shearing viscosity of Vit 4’ deduced from the results of compression tests conducted at T= 583 *K* and different strain rates.

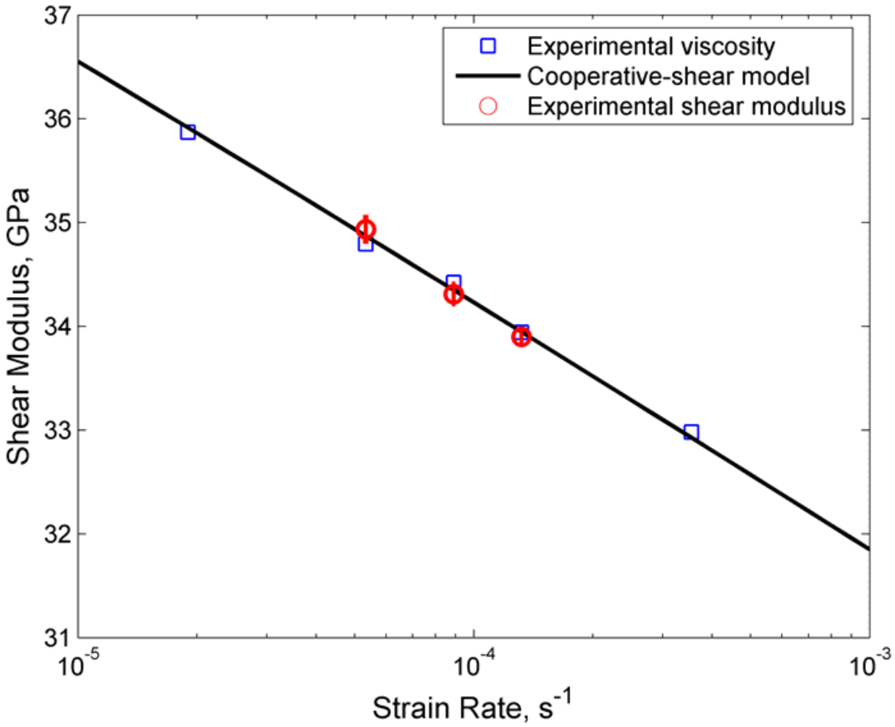

Fig. 3.10 Comparison of the shear modulus from wave speed measurements (circles) and viscosity from compression tests (squares). The cooperative shearing model prediction is shown as a solid line.

3.5 Conclusions

High temperature compression tests were used to characterize the viscosity of a newly developed amorphous alloy $Zr_{47.4}Ti_{8.0}Cu_{7.3}Ni_{9.8}Be_{27.5}$ (Vit 4'). Ultrasonic wave speed measurements were also conducted on specimens quenched immediately after compression to explore the correlation between the viscosity and the shear modulus of the stressed material. The following conclusions can be drawn from this investigation:

(i) The flow stress of $Zr_{47.4}Ti_{8.0}Cu_{7.3}Ni_{9.8}Be_{27.5}$ (Vitreloy 4') is higher than that Vitreloy 4 in the supercooled liquid regime. Its viscosities are similar to those of Vitreloy 1 at the same temperature and strain rate. Moreover, unlike Vitreloy 1, the DSC trace of Vit 4 does not show spinodal phase separation. With the improved thermal stability and mechanical properties, it is a good candidate in the Vitreloy family for future thermodynamical study and structural application.

(ii) A cooperative shear model is used to describe the deformation mechanism of amorphous materials. It captures the viscosities of both the Newtonian and non-Newtonian flows of $Zr_{47.4}Ti_{8.0}Cu_{7.3}Ni_{9.8}Be_{27.5}$ well and the model is in good agreement with the experimental results. The Newtonian viscosities of other alloys with established viscosity databases in literature, such as the $Pd_{43}Ni_{10}Cu_{27}P_{20}$ and Vitreloy 1, are also characterized and fit with the model. They are both coherent between the experimental data and the predictions from cooperative shear model.

(iii) The shear moduli of $Zr_{47.4}Ti_{8.0}Cu_{7.3}Ni_{9.8}Be_{27.5}$ after testing at 583 K and various strain rates are measured with the acoustic technique. A decreasing in the shear modulus is observed with increasing strain rate. The relation between the non-Newtonian viscosity and the shear modulus of stressed amorphous alloy suggested by cooperative shear model is used to calculate the shear modulus from the measured viscosity of $Zr_{47.4}Ti_{8.0}Cu_{7.3}Ni_{9.8}Be_{27.5}$. The results ($\dot{\varepsilon} = 5.3 \times 10^{-5} s^{-1}$, $\dot{\varepsilon} = 8.9 \times 10^{-5} s^{-1}$, and $\dot{\varepsilon} = 1.3 \times 10^{-4} s^{-1}$) are in good agreement with the modulus measured with the acoustic technique.

References

[1] W. Klement, R. H. Willens, and P. Duwez, "Non-Crystalline Structure in Solidified Gold-Silicon Alloys," *Nature*, **187**, 869-870 (1960).

[2] W. L. Johnson, "Metastable Phases," in *Intermetallic Compounds*, vol. 1, J. H. Westbrook, Fleischer, R.L., Ed. New York: Wiley, 687-709 (1994).

[3] A. Inoue, T. Zhang, and T. Masumoto, "Production of Amorphous Cylinder and Sheet of $La_{55}Al_{25}Ni_{20}$ Alloy by a Metallic Mold Casting Method," *Materials Transactions JIM*, **31**, 425-428 (1990).

[4] A. Inoue, A. Kato, T. Zhang, S. G. Kim, and T. Masumoto, "Mg-Cu-Y Amorphous-Alloys with High Mechanical Strengths Produced by a Metallic Mold Casting Method," *Materials Transactions JIM*, **32**, 609-616 (1991).

[5] T. Zhang, A. Inoue, and T. Masumoto, "Amorphous Zr-Al-Tm (Tm = Co, Ni, Cu) Alloys with Significant Supercooled Liquid Region of over 100-K," *Materials Transactions JIM*, **32**, 1005-1010 (1991).

[6] A. Peker and W. L. Johnson, "A Highly Processable Metallic Glass - $Zr_{41.2}Ti_{13.8}Cu_{12.5}Ni_{10.0}Be_{22.5}$," *Applied Physics Letters*, **63**, 2342-2344 (1993).

[7] X. H. Lin and W. L. Johnson, "Formation of Ti-Zr-Cu-Ni Bulk Metallic Glasses," *Journal of Applied Physics*, **78**, 6514-6519 (1995).

[8] J. F. Loffler and W. L. Johnson, "Model for decomposition and nanocrystallization of deeply undercooled $Zr_{41.2}Ti_{13.8}Cu_{12.5}Ni_{10.0}Be_{22.5}$," *Applied Physics Letters*, **76**, 3394-3396 (2000).

[9] H. Chen, Y. He, G. J. Shiflet, and S. J. Poon, "Deformation-Induced Nanocrystal Formation in Shear Bands of Amorphous-Alloys," *Nature*, **367**, 541-543 (1994).

[10] D. Turnbull and M. H. Cohen, "Free-Volume Model of Amorphous Phase - Glass Transition," *Journal of Chemical Physics*, **34**, 120-& (1961).

[11] F. Spaepen, "Microscopic Mechanism for Steady-State Inhomogeneous Flow in Metallic Glasses," *Acta Metallurgica*, **25**, 407-415 (1977).

[12] G. Ruitenberg, P. deHey, F. Sommer, and J. Sietsma, "Pressure dependence of the free volume in amorphous Pd40Ni40P20 and its implications for the diffusion process," *Materials Science and Engineering A-Structural Materials Properties Microstructure and Processing*, **226**, 397-400 (1997).

[13] P. A. Duine, J. Sietsma, and A. Vandenbeukel, "Defect Production and Annihilation near Equilibrium in Amorphous $Pd_{40}Ni_{40}P_{20}$ Investigated from Viscosity Data," *Acta Metallurgica Et Materialia*, **40**, 743-751 (1992).

[14] P. de Hey, J. Sietsma, and A. Van den Beukel, "Structural disordering in amorphous $Pd_{40}Ni_{40}P_{20}$ induced by high temperature deformation," *Acta Materialia*, **46**, 5873-5882 (1998).

[15] P. de Hey, J. Sietsma, and A. vandenBeukel, "Creation of free volume in amorphous $Pd_{40}Ni_{40}P_{20}$ during high temperature deformation," *Materials Science and Engineering A-Structural Materials Properties Microstructure and Processing*, **226**, 336-340 (1997).

[16] B. van Aken, P. de Hey, and J. Sietsma, "Structural relaxation and plastic flow in amorphous $La_{50}Al_{25}Ni_{25}$," *Materials Science and Engineering A-Structural Materials Properties Microstructure and Processing*, **278**, 247-254 (2000).

[17] R. Busch, Y. J. Kim, and W. L. Johnson, "Thermodynamics and Kinetics of the Undercooled Liquid and the Glass-Transition of the $Zr_{41.2}Ti_{13.8}Cu_{12.5}Ni_{10.0}Be_{22.5}$Alloy," *Journal of Applied Physics*, **77**, 4039-4043 (1995).

[18] J. Li, F. Spaepen, and T. C. Hufnagel, "Nanometre-scale defects in shear bands in a metallic glass," *Philosophical Magazine A-Physics of Condensed Matter Structure Defects and Mechanical Properties*, **82**, 2623-2630 (2002).

[19] J. Lu, G. Ravichandran, and W. L. Johnson, "Deformation behavior of the $Zr_{41.2}Ti_{13.8}Cu_{12.5}Ni_{10.0}Be_{22.5}$ bulk metallic glass over a wide range of strain-rates and temperatures," *Acta Materialia*, **51**, 3429-3443 (2003).

[20] H. Kato, Y. Kawamura, H. S. Chen, and A. Inoue, "A fictive stress model calculation of nonlinear viscoelastic behaviors in a Zr-based glassy alloy: Stress growth and relaxation," *Japanese Journal of Applied Physics Part 1-Regular Papers Short Notes & Review Papers*, **39**, 5184-5187 (2000).

[21] J. S. Langer and L. Pechenik, "Dynamics of shear-transformation zones in amorphous plasticity: Energetic constraints in a minimal theory," *Physical Review E*, **68**, 061504 (2003).

[22] W. L. Johnson and K. Samwer, "A universal criterion for plastic yielding of metallic glasses with a $(T/T\text{-}g)^{(2/3)}$ temperature dependence," *Physical Review Letters*, **95**, 195501 (2005).

[23] F. H. Stillinger, "A Topographic View of Supercooled Liquids and Glass-Formation," *Science*, **267**, 1935-1939 (1995).

[24] D. J. Wales, "A microscopic basis for the global appearance of energy landscapes," *Science*, **293**, 2067-2070 (2001).

[25] A. Heuer, "Properties of a glass-forming system as derived from its potential energy landscape," *Physical review letters*, **78**, 4051-4054 (1997).

[26] K. Kristiakova, P. Svec, and M. Deanko, "Cluster structure and thermodynamics of formation of (nano)crystalline phases in disordered metastable metallic systems," *Materials Science and Engineering A-Structural Materials Properties Microstructure and Processing*, **375-77**, 136-149 (2004).

[27] M. L. Lind and W. L. Johnson, "Unpublished result," (2006).

[28] C. C. Hays, C. P. Kim, and W. L. Johnson, "Large supercooled liquid region and phase separation in the Zr–Ti–Ni–Cu–Be bulk metallic glasses," *Applied Physics Letter*, **75**, 1089-1091 (1999).

[29] ASTM, "Annual book of ASTM standards," in Standard Test Method for Density of Glass by Buoyancy. Philadelphia: American Society of Testing and Materials (1998).

[30] J. Lu, "Mechanical behavior of a bulk metallic glass and its composite over a wide range of strain rates and temperatures," *Ph D Thesis*. Pasadena: California Institute of Technology (2002).

[31] Y. J. Kim, R. Busch, W. L. Johnson, A. J. Rulison, and W. K. Rhim, "Experimental determination of a time-temperature-transformation diagram of the undercooled $Zr_{41.2}Ti_{13.8}Cu_{12.5}Ni_{10.0}Be_{22.5}$ alloy using the containerless electrostatic levitation processing technique," *Applied Physics Letters*, **68**, 1057-1059 (1996).

[32] T. Waniuk, J. Schroers, and W. L. Johnson, "Timescales of crystallization and viscous flow of the bulk glass-forming Zr-Ti-Ni-Cu-Be alloys," *Physical Review B*, **67**, 184203 (2003).

[33] H. Kolsky, *Stress waves in solids*. Oxford: Clarendon Press (1953).

[34] T. A. Waniuk, R. Busch, A. Masuhr, and W. L. Johnson, "Equilibrium viscosity of the $Zr_{41.2}Ti_{13.8}Cu_{12.5}Ni_{10.0}Be_{22.5}$ bulk metallic glass-forming liquid and viscous flow during relaxation, phase separation, and primary crystallization," *Acta Materialia*, **46**, 5229-5236 (1998).

[35] S. Buchner and A. Heuer, "Potential energy landscape of a model glass former: Thermodynamics, anharmonicities, and finite size effects," *Physical Review E*, **60**, 6507-6518 (1999).

[36] M. Tao, J. S. Harmon, and M. D. Demetriou, "Unpublished result," (2005).

[37] G. J. Fan, H. J. Fecht, and E. J. Lavernia, "Viscous flow of the $Pd_{43}Ni_{10}Cu_{27}P_{20}$ bulk metallic glass-forming liquid," *Applied Physics Letters*, **84**, 487-489 (2004).

[38] G. W. Scherer, *Relaxation in glass and composites*. Malabar: Krieger Publishing (1992).

[39] G. S. Fulcher, "Analysis of recent measurements of the viscosity of glasses," Journal *of the American Ceramic Society*, **8**, 339-355 (1925).

[40] M. H. Cohen and G. S. Grest, "Liquid-Glass Transition, a Free-Volume Approach," *Physical Review B*, **20**, 1077-1098 (1979).

[41] A. Masuhr, R. Busch, and W. L. Johnson, "Thermodynamics and kinetics of the $Zr_{41.2}Ti_{13.8}Cu_{12.5}Ni_{10.0}Be_{22.5}$ bulk metallic glass forming liquid: glass formation from a strong," *Journal of Non-Crystalline Solids*, **252**, 566-571 (1999).

[42] J. H. Mathews and K. D. Fink, *Numerical Methods Using Matlab*, 4th ed, Prentice Hall, (2003).

Chapter 4

High temperature behavior of β phase Vitreloy composite

Abstract

The plastic flow behavior of a bulk metallic glass *in-situ* composite $Zr_{56.3}Ti_{13.8}Cu_{6.9}Ni_{5.6}Be_{12.5}Nb_{5.0}$ (β-Vitreloy™ or β-Vit) was investigated under uniaxial compression at various strain rates ($10^{-4} \sim 10^{-1} s^{-1}$) in the supercooled liquid regime. The *in-situ* composite contains $\sim 25\%$ volume fraction of crystalline β-phase dendrites (Zr-Ti-Nb rich bcc phase) embedded in the amorphous matrix whose composition is close to that of amorphous Vitreloy 1. The composite exhibited extended plasticity similar to that of amorphous Vitreloy 1. Significant "hardening" was observed when the material was deformed at high temperatures and low strain rates. A dual-phase composite model was employed in finite element simulations to understand the hardening mechanism. The constitutive relations of both the amorphous matrix and the crystalline dendrite at constant temperature and strain rate were characterized by a Ramberg-Osgood power hardening law, with parameters found by fitting the uniaxial compression test data for each of the phases. Numerical simulation of the composite with 25% volume fraction of dendrite inclusions was able to capture the "hardening" feature observed in the experimental results. The effects of the dendrite size and distribution on the overall composite behavior were also studied. This comprehensive study on the high temperature mechanical properties of β-Vit1 revealed the complexity of the deformation mechanisms of composites with a metallic glass matrix at the mesoscopic level and provided insights for designing metallic glass composites for high temperature applications.

Key words: Metallic glass composite, Dual-phase, Volume fraction, High temperature deformation, Strain hardening, Superplasticity

4.1 Introduction

Bulk metallic glasses (BMGs) have received significant attention in recent years due to their unique thermal and mechanical properties and potential in structural applications [1, 2]. The deformation of bulk metallic glasses differs from that of a crystalline metallic material because of the absence of long-range ordering in its amorphous structure. Some bulk metallic glasses have revealed exceptional physical and mechanical properties. One such material is $Zr_{41.25}Ti_{13.75}Cu_{12.5}Ni_{10}Be_{22.5}$ (Vitreloy 1™, commonly referred to as Vit 1), which has a critical cooling rate of 1 *K/s* and can be cast up to a size of 5 cm in thickness [1]. Its high yield stress and high strength-to-density make it an excellent candidate for structural applications [3, 4].

A recent experimental study [5] of Vit 1 provided a flow map of the material over a large range of strain rates and temperatures. At room temperature, Vit 1 deforms through shear localization, associated with limited plasticity accumulated from localized thin shear bands, and then fails as a brittle material. At temperatures around the onset of the glass transition T_g and intermediate strain rates, Vit 1 exhibits extended ductility due to viscous flow which features stress overshooting and undershooting before reaching a constant value and is characterized as the non-Newtonian flow mode. At even higher temperatures in the supercooled liquid regime and lower strain rates, the viscous flow of Vit 1 becomes Newtonian, and the flow stress reaches steady state immediately after the material yields. Such deformation behavior is found almost universally in metallic glasses discovered to date, namely in Zr based alloys, in Fe- based, La-based, and Pd-based alloys [6-8].

Since the room temperature deformation of metallic glasses is dominated by shear localization in which the material exhibits almost no plastic deformation before it fails, these materials could find only limited practical applications. Most bulk metallic glasses fail in a catastrophic manner under uniaxial tension, breaking along a single dominant shear band right after reaching the yield point. Multiple shear bands form under confined stress states such as compression and indentation [9, 10], with plastic deformation accumulated increased by 1-3 %. Considerable ductility (up to 10%) in BMGs can be achieved by deforming the materials under sufficient confinement or pressure [11, 12]. To increase the ductility of BMGs and to expand the scope of their applications, researchers have been working toward finding alloy compositions which lead to enhanced ductility. Due to the glassy nature of amorphous alloys, such efforts had very limited space. So far, the alloy discovered with the best room temperature ductility is a platinum based alloy, $Pt_{57.5}Cu_{14.7}Ni_{5.3}P_{22.5}$, developed at Caltech, which exhibited 20% plastic strain in compression [13]. However, with 57.5% of platinum in the chemical composition, the alloy is very expensive and for that reason, not suitable for practical structural applications, though it is an excellent model material for understanding the physics of deformation in amorphous alloys. An alternative solution to improved the ductility of metallic glasses is to process metallic glass composites whose microstructure can be tailored to improve their mechanical properties [14-17].

Early efforts in fabricating metallic glass composites included the use of amorphous metal ribbons as reinforcement in polymer or glass ceramic matrix [18-20], adding ceramic particles or fibers in metallic glass ribbons with melt spinning technique [21], and reinforcing bulk metallic glass matrix with ductile metal or ceramic particles or wires [22-26]. The mechanical properties of these *ex-situ* reinforced metallic glass composites were improved because the existence of additional phases facilitated the formation of multiple shear bands during deformation, and thus enhancing the macroscopic plasticity of the composites [27, 28]. However, the second phase introduced in the amorphous matrix also caused problems such as debonding between the phases and, as a consequence, e.g., poor fatigue resistance [27].

Recently, *in-situ* composite processing techniques were developed with the discovery of new amorphous alloy systems with improved glass forming abilities [29-31]. Among them which exhibited excellent mechanical properties is a zirconium based metallic glass composite discovered at Caltech in 2000 by Johnson and coworkers [16]. By introducing five atomic percent (at. %) of niobium in the place of copper in Vitreloy 1 and processing with the same arc-melting and quenching procedures, a secondary bcc β-phase crystalline was formed and stabilized in the amorphous matrix [16, 31]. This so-called β-Vitreloy composite was found to have a chemical composition of $Zr_{71}Ti_{16.3}Nb_{10}Cu_{1.8}Ni_{0.9}$ (at. %) in the crystalline dendrite phase, and the amorphous matrix phase was found to have a chemical composition of $Zr_{47}Ti_{12.9}Nb_{2.8}Cu_{11}Ni_{9.6}Be_{16.7}$ (at. %) with an estimate of 25% volume fraction of the dendritic β-phase. The chemical composition of the amorphous matrix is close to that of the Vitreloy 1 [1]. Scanning electron microscopic (SEM) and transmitted electron microscopic (TEM) studies [16, 32] showed that the dendrites were perfectly bonded with the amorphous matrix even after having been plastically deformed in tensile or bending tests. The ductility of the composite was significantly increased by the dendritic phase. Upon compression, the material accumulated 5-6% plastic strain before it failed without significant loss of strength [33]. A comparison of the physical and mechanical properties of Vit 1 and β-Vit is shown in Table 4.1.

The promising mechanical properties of β-Vit composite have attracted much attention. Hays *et al.* [34] conducted a series of mechanical tests on the fabricated composite. They noted that the composite sustained 5% of overall plastic strain and 15% of plastic strain in the necking area of a tensile specimen. Charpy tests on the composite showed a three fold increase in the impact toughness of β-Vit over amorphous Vit 1 specimen [33]. *In-situ* TEM study on a milled β-Vit piece under tension revealed dislocations and twins in the ductile β phase, which were attributed as the mechanisms that resulted in the formation of multiple shear bands. Fracture and fatigue studies showed enhanced fracture toughness, more stable crack growth, and increased fatigue life of the composite material than the amorphous Vit 1 [27]. The mechanical behavior of composites with slightly different niobium concentrations were also studied in a comparative manner [33]. Clausen *et al*. [35] employed the neutron diffraction technique and performed independent compression tests on β-Vit composite and the monolithic β phase crystallite. They used a self-consistent model to describe the deformation behavior of the composite in both the elastic and plastic regimes. However, their conclusion on the mechanism of shear band formation did not entirely agree with the earlier interpretation of Hays *et al.* [16].

Table 4.1 Physical and mechanical properties of Vit 1 and β-Vit composite

Properties	Vit 1	β-Vit
Density (g/cm^3)	6.0	6.2
Young modulus (GPa)	96	80
Shear modulus (GPa)	34	29
Poisson's ratio	0.36	0.37
Elastic strain limit	0.02	0.018
Tensile yield strength (GPa)	1.90	1.45
Vickers hardness (kg/mm^2)	534	–
Plane strain fracture toughness ($MPam^{1/2}$) at loading rate of 10^{-2} MPa $m^{1/2}s^{-1}$	~16 *	35 *
Dynamic fracture toughness ($MPam^{1/2}$) at loading rate of 10^4 MPa $m^{1/2}s^{-1}$	~50-70	–
Dynamic fracture toughness (MPa $m^{1/2}$) at loading rate of 10^7 MPa $m^{1/2}s^{-1}$	~150-300	–
Charpy impact resistance (J)	~8.0	~24.0

- * are from Flores *et al.* 2003 [27].
- all other data are adopted from Lu [36]; for original sources, refer to Table1 in Chapter 2 of Ref. [36].

With most of the studies of β-Vit focused on it mechanical properties at room temperature, the high temperature properties of the composite are not well known, though it is important to understand the material properties in a wide range of thermomechanical conditions. The high sensitivity of the matrix material to temperature and strain rate change in its supercooled liquid state [5] provides additional motivation to investigate the high temperature behavior of β-Vit composite. Also, the β-Vit composite serves as an excellent model system to study the flow behavior of dual-phase composite with an amorphous matrix.

The property of dual-phase composite materials poses a classic mechanics problem with extensive studies on theoretical modeling and numerical simulation. Eshelby first provided the analytical solution for the elastic field for an ellipsoidal inhomogeneity in an infinite matrix [37]. Bao *et al*. [38, 39] extended the two-phase model to the plastic flow region. They studied the overall stress-strain relation of two non-hardening solids with various flow stress ratios and different volume fractions using a stress and a strain-rate self-consistent model [39]. The plastic flow and creep behavior of ductile matrices reinforced by rigid particles was also studied in a systematic manner for inclusions with different shapes in a unit cell [39]. Brinson and Knauss studied a particular type of composite consisting of two viscoelastic phases (thermorheologically complex material) to model its mechanical response behavior as a function of time (frequency) and temperature, which provided a scheme of numerically modeling multiphase viscoelastic materials [40]. Recent work on amorphous polymeric materials or polymeric composites with semi-crystalline inclusions could possibly also be taken as an analogy to the study of BMGs and their composites [41-42].

The numerical simulation of the deformation behavior of BMGs and their composites has been a challenge because of the complicated constitutive relations of their phases which cannot be effectively described with conventional plastic flow theories developed for crystalline solids. The inhomogeneous deformation of BMGs features shear band formation and instabilities, and the homogeneous deformation in non-Newtonian flow region features stress over- and under-shooting. All of the features pose considerable difficulties for numerical simulation. Anand and Su [43] developed a finite-deformation, Mohr- Coulomb type constitutive model and used it to study the room temperature deformation of metallic glasses. Using this model, the formation of multiple shear bands was successfully simulated in the compression of cylindrical specimens and in indentation. A recent study by Mota, Yang, and Ortiz successfully captured the high temperature deformation features of BMGs such as strain hardening, thermal softening, rate-dependency, and non-Newtonian viscosity by assuming that the free volume concentration was the fundamental mechanism causing the deformation of amorphous alloys and provided a relatively comprehensive constitutive model for finite deformation plasticity of BMGs [44].

Other studies focused mostly on either theoretical model development [45-47] or on molecular dynamics simulations [49-50] without directly simulating deformations in structural applications.

In this investigation, compression tests were performed at various strain rates on β-Vit over a range of temperatures in its supercooled liquid region. Besides shear localization, non-Newtonian flow, and Newtonian flow modes similar to those observed in pure metallic glasses, the β-Vit composite also exhibited strain hardening under certain conditions (high temperature, low strain rate). The deformation behavior of the monolithic bcc β phase crystallite was also studied under different temperature and strain rate conditions. To understand the mechanism of hardening in the composite, finite element simulations were performed with appropriate component material properties as input. The properties of monolithic β phase crystallites were obtained from laboratory measurements, and the stress-strain relations of the amorphous matrix were taken the same as those of Vitreloy 1 [5]. The simulations were conducted with the commercial finite element software ABAQUS/Standard [62] with an appropriate choice of the unit cell models with inclusions of different shapes and periodic boundary conditions.

4.2 Experimental

4.2.1 Material preparation

The *in-situ* bulk metallic glass composite $Zr_{56.3}Ti_{13.8}Cu_{6.9}Ni_{5.6}Be_{12.5}Nb_{5.0}$ (commercial trade mark β-Vitreloy1™ or β-Vit) was originally developed in the Keck Materials Research Laboratories at Caltech by Hays *et al.*, in 2000 [16]. The composite material for this investigation was prepared by mixing metal elements with purity of 99.9% ~ 99.999% in appropriate proportions, then arc melting and water quenching into ingots of about 25 mm (1 inch) long at Liquid Metal Technologies, Inc., Lake Forrest, CA. Differential scanning calorimetry (DSC) study of the as-prepared material revealed that the temperatures at the onset of the glass transition (T_g) and the temperature at the onset of the first crystallization (T_{x1}) were

602 K and 655 K, respectively, when subjected to a constant heating rate of $20\,K/\min$ (see Fig. 4.1). Cylindrical specimens with a nominal size of $3.8\,mm$ in diameter $6.3\,mm$ in length were electrical discharge machined from the ingots. Only the center part of the ingots, of which the homogeneity is better than the boundary part, was used for making the specimens. The length-to-diameter aspect ratio was kept smaller than 2:1 to avoid buckling during compression loading.

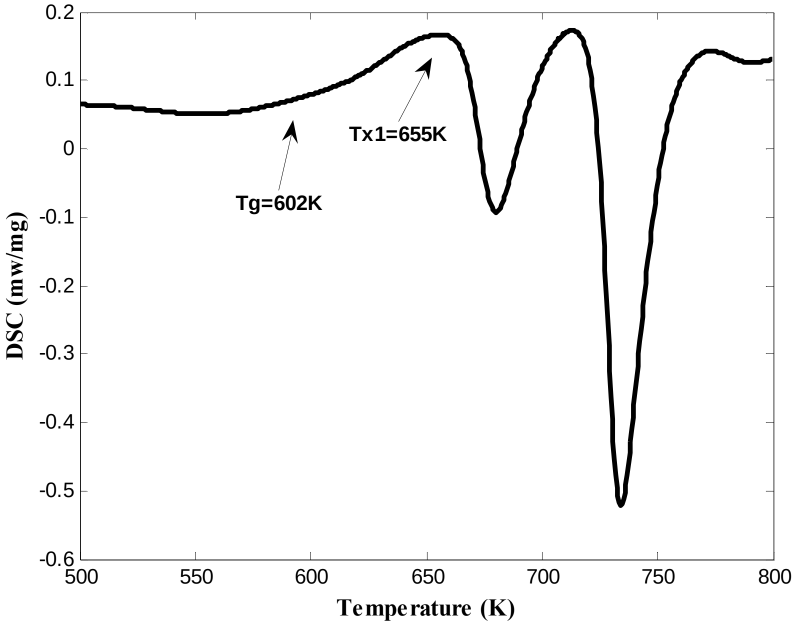

Fig 4.1 DSC trace of as-prepared β-Vit composite material.

Microprobe analyses of the individual phases in a sample of the composite were performed to determine their chemical composition. The surface of a sample was cut from the ingot with a diamond saw, then polished with 600-grit, 1200-grit sandpaper and 9, 3, and 2 μm diamond polishing compound in sequence. A JEOL JXA-8200 electron probe micro-analyzer was used in this investigation, which provided a measurement resolution of 1 μm^3. About 20 random spots were chosen in both the dendrite and the matrix for analysis. The average dendrite composition was determined to be $Zr_{71.5}Ti_{16.4}Cu_{1.9}Ni_{0.83}Nb_{9.4}$ (at. %), and the average matrix composition was found to be $Zr_{45.7}Ti_{12.0}Cu_{9.5}Ni_{8.1}Nb_{2.5}Be_{22.1}$ (at. %). According to Hays *et al*. [16], the first ever β-Vit produced in the Keck Laboratories had the nominal dendrite chemical composition of $Zr_{71}Ti_{16.3}Cu_{1.8}Ni_{0.9}Nb_{9.6}$ (at. %). Considering the influence of the processing conditions such as arc melting homogeneity and cooling rate on the shape, size, and composition of the dendrites in the composite [51], the composition of the current as-prepared composite material was in good agreement with the original composite. The matrix material had the chemical composition close to that of Vitreloy 1, $Zr_{41.25}Ti_{13.75}Cu_{12.5}Ni_{10}Be_{22.5}$ (at. %), but was exactly the same.

Monolithic crystalline specimens of the β-phase dendrite were also prepared for compression tests. The material was made by mixing the metal elements according to the composition from the microprobe result, then arc-melting and quenching it into 1 inch (25 mm) long ingots. Rectangular specimens with $3\,mm \times 3\,mm$ square cross-section and $5.5\,mm$ length were cut from the ingots with a diamond saw. The top and bottom surfaces of all specimens were polished with a 600-grit sandpaper. During the test, high temperature Bentone-Clay semi-synthetic grease was applied to both surfaces to reduce the effect of friction.

4.2.2 High temperature compression

In order to investigate the flow behavior of the β-Vit composite in its supercooled liquid state, the testing temperatures were chosen to fall within $\Delta T = T_{x1} - T_g$, the interval between the onset temperature of the glass transition (T_g) and the onset temperature of the first crystallization (T_{x_1}). All experiments were conducted under uniaxial compression, with strain rates varying in the range of $10^{-5} - 10^{-1} s^{-1}$. All three deformation modes (shear localization, non-Newtonian, and Newtonian) were covered under the current experimental conditions.

Quasi-static compression tests were carried out using a servo-hydraulic Materials Testing System (MTS 358 series) with multiple 5-kip/20-kip/50-kip load cartridges and a 5-inch displacement cartridge. The testing apparatus includes a loading frame designed to accommodate a split electric furnace, a Linear Variable Differential Transducer (LVDT) and its conditioner for displacement measurement, and a set of furnaces with a temperature feedback/control system. During the experiment, the specimen was placed at the center of the electric furnaces (model# 5010-1057-00A, Lunaire, WI; 75 mm in diameter and 150 mm long) with steel plates on top and bottom and glass wool tightly wrapped around for insulation. The PID temperature controller (series CN77000, Omega Engineering) had the input from a K-type thermocouple welded at the center of the lateral surface of the specimen, and the output controlling the status of the furnaces. A constant heating rate of about 20 K/min that brought the specimen close to desired temperature was implemented by properly setting the proportional (P), integral (I), and derivative (D) values of the controller. Manual adjustment with small temperature increment was preferred during the last 20 K of the heat-up phase, to avoid overshoot over the desired set-point temperature. The PID controller took over again after reaching the testing temperature and was capable of maintaining the temperature within a fluctuation of $\pm 0.5\,K$ during the course of the loading.

Four temperatures within ΔT (supercooled liquid region) of β-Vit composite were selected for testing: $613\,K$, $623\,K$, $633\,K$, and $643\,K$. At each temperature, 3 to 4 compression tests at strain rates varying in the range of $10^{-5} - 10^{-1} s^{-1}$ were performed. To avoid deformation induced crystallization of the amorphous matrix material, the strain rate and the overall strain for each test were designed such that the sum of the heating and the loading times did not exceed the crystallization time limit of the matrix material of β-Vit. Even though the complete data of the time-temperature-transformation diagram was not available for β-Vit, such characterization has been performed on a series of Zr- based amorphous alloy families, whose chemical compositions were very close to that of the matrix of the β-Vit composite [52]. Therefore, it was assumed that the transformation time of the amorphous phase of β-Vit composite at certain temperature fell within the range of the transformation times of other alloys in the Vitreloy family. This transformation time was taken as the time upper limit for the compression tests at a given temperature. Figure 4.2 shows the time-temperature-transformation diagrams of the Vitreloy family of alloys and forms the basis for the assumed time-temperature-transformation data for the amorphous phase of β-Vit. At the testing temperatures in this investigation ($613K \sim 643K$), the average value of the transformation time is about 5000 seconds. All the experiments at various strain rates were conducted to be completed within this time range.

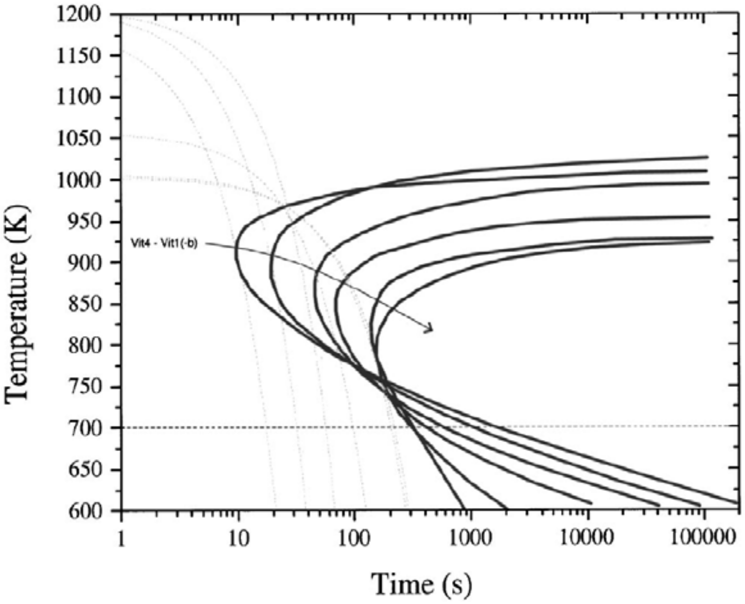

Fig. 4.2 Time-temperature-transformation diagram for a series of Vitreloy family of alloys (Reproduced from Waniuk *et al.* [52])

4.3 Results

4.3.1 Stress-strain behavior of β-Vit composite

The true stress-strain curves obtained from the compression tests on β-Vit composite at four different temperatures for various strain rates are shown in Figs. 4.3(a)-(d). Similar to the other amorphous alloys reported previously, e.g., for amorphous Vitreloy 1 [5, 7, 53], three distinct modes of deformation in the amorphous alloys could also be clearly observed for this composite. For the test at the temperature of $T = 613\,K$ and strain rate of $\dot{\varepsilon} = 0.03\,s^{-1}$, the specimen failed in a brittle manner after reaching the yield point, without showing much ductility. The specimens which were tested at intermediate strain rates at each temperature showed non-Newtonian homogeneous flow behavior, which featured stress overshooting and undershooting in the stress-strain curve. ($T = 613\,K$, $\dot{\varepsilon} = 0.01 s^{-1}$, and $\dot{\varepsilon} = 1.2 \times 10^{-3} s^{-1}$; $T = 623\,K$, $\dot{\varepsilon} = 0.07 s^{-1}$ and $\dot{\varepsilon} = 0.01 s^{-1}$; $T = 633\,K$, $\dot{\varepsilon} = 0.07 s^{-1}$, and $\dot{\varepsilon} = 0.01 s^{-1}$; $T = 643\,K$, $\dot{\varepsilon} = 0.07 s^{-1}$, and $\dot{\varepsilon} = 0.01 s^{-1}$). The specimen tested at even lower strain rates and higher temperature deformed in a Newtonian flow manner, in which the stress-strain curve reached steady-state soon after the yield point was reached. ($T = 613\,K$, $\dot{\varepsilon} = 2.2 \times 10^{-4} s^{-1}$; $T = 623\,K$, $\dot{\varepsilon} = 1.2 \times 10^{-3} s^{-1}$ and $\dot{\varepsilon} = 2.0 \times 10^{-4} s^{-1}$; $T = 633\,K$, $\dot{\varepsilon} = 1.2 \times 10^{-3} s^{-1}$).

The present high temperature compression tests on β-Vit composite revealed another interesting mode of deformation. At very low strain rates and high temperatures, the flow did not reach a steady state but showed a hardening trend ($T = 633\,K$, $\dot{\varepsilon} = 2.2 \times 10^{-4} s^{-1}$; $T = 643\,K$, $\dot{\varepsilon} = 1.1 \times 10^{-3} s^{-1}$ and $\dot{\varepsilon} = 2.5 \times 10^{-4} s^{-1}$) (Figs. 4.3(c) and 4.3(d)). Such hardening was not observed obviously in the deformation of amorphous alloys at high temperatures [5]. It has been reported that in the high temperature tension (compression) tests of other Zr- based BMGs [54, 55], such hardening phenomenon dominated the later stages of the deformation. It was suspected that a large amount of nano-crystallites formed in the amorphous matrix, which served as reinforcing inclusions in the matrix, thus hardening the material and increasing the overall flow stress. Nieh and Wadsworth proposed a simple mode to estimate the strain rate and flow stress of an amorphous-nanocrystalline liquid mixture in terms of the volume fraction of the nano-crystalline inclusions and their distribution of morphologies [56]. Hence, it was not surprising to see the hardening behavior in the high temperature compression tests of β-Vit composite, which contained *in-situ* bcc crystalline β-phase with the dendrite size varying from a few nanometers to a few microns.

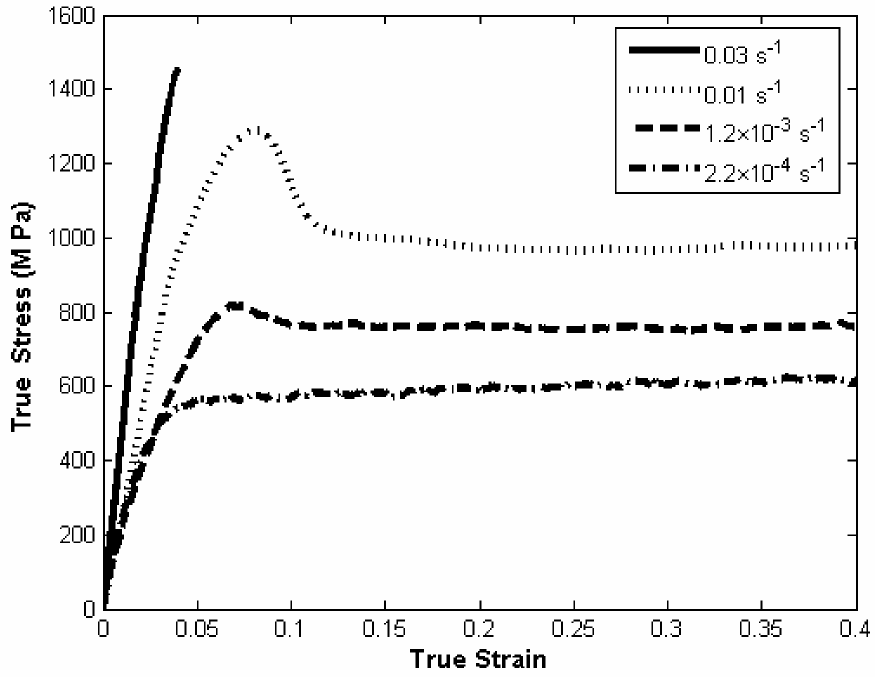

1600
1400
1200
1000
800
600
400
200
0
0
0.05
0.1
0.15
0.2
0.25
0.3
0.35
0.4
True Strain
True Stress (M Pa)
0.03 s^{-1}
0.01 s^{-1}
1.2×10^{-3} s^{-1}
2.2×10^{-4} s^{-1}

(a)

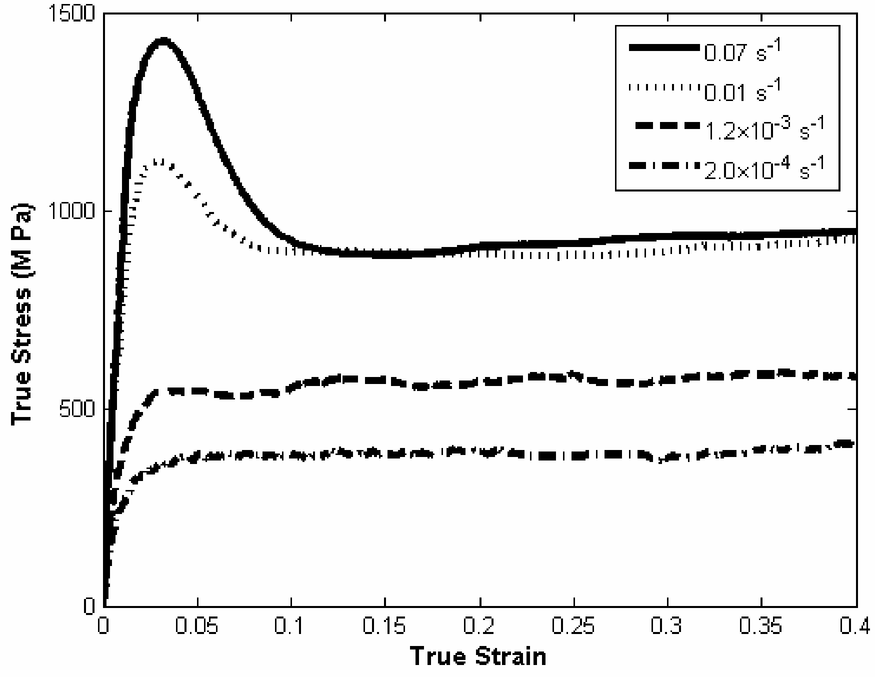

1500
1000
500
0
0
0.05
0.1
0.15
0.2
0.25
0.3
0.35
0.4
True Strain
True Stress (M Pa)
0.07 s^{-1}
0.01 s^{-1}
1.2×10^{-3} s^{-1}
2.0×10^{-4} s^{-1}

(b)

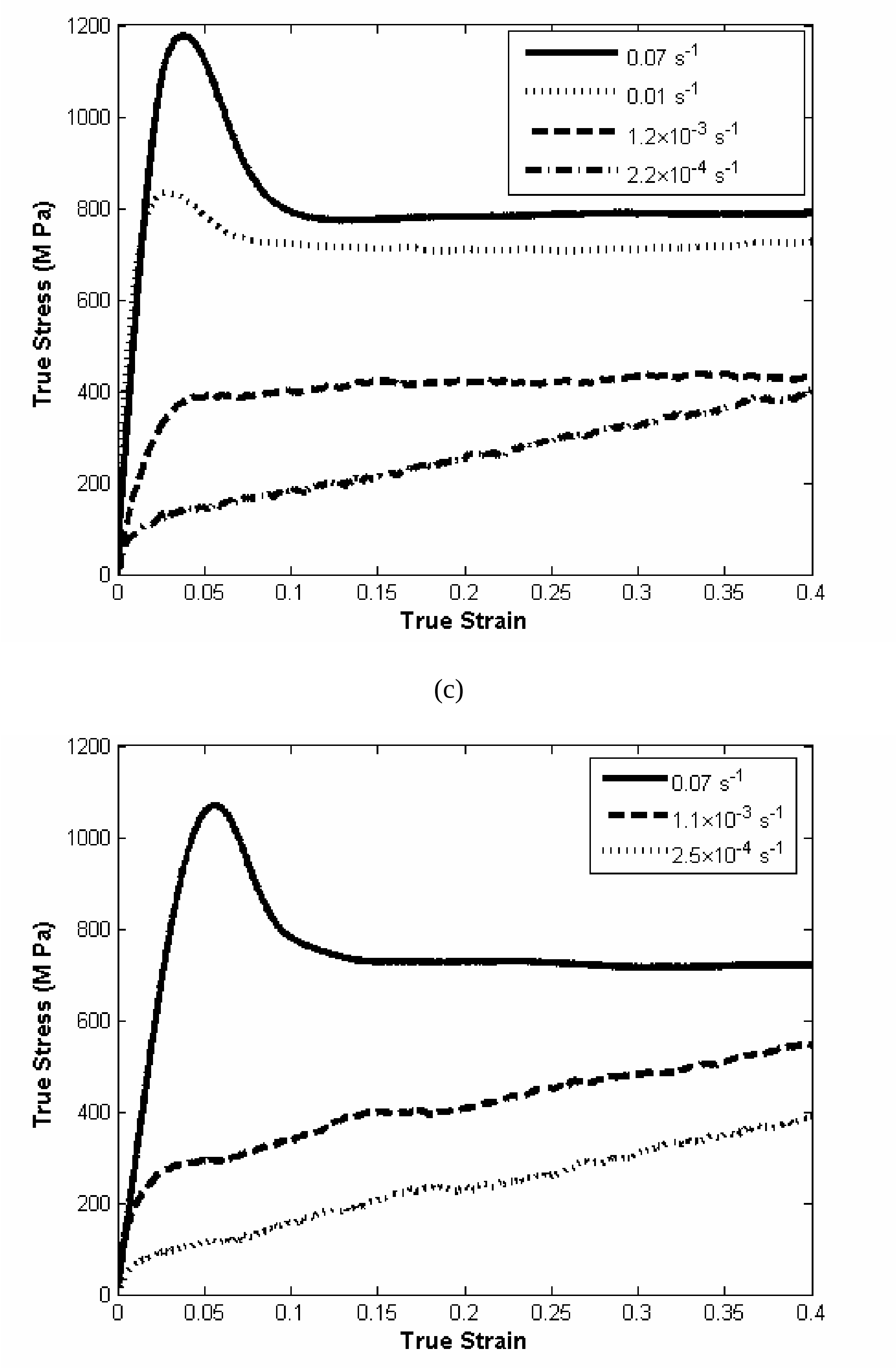

(c)

(d)

Fig. 4.3 True stress-strain curves of β-Vit1 in uniaxial compression at various temperatures and strain rates: (a) T=613 K; (b) T=623 K; (c) T=633 K; (d) T=643 K.

4.3.2Stress-strain behavior of the monolithic β phase crystallite

Compression tests were performed on the as cast monolithic β phase crystalline specimens, and the stress-strain relations were obtained following the procedures outlined earlier. The constitutive response obtained for the β phase crystallite will be used in the numerical simulations of the effective behavior of the β-Vit composite in section 4.5. It is noted that the deformation of the crystalline dendrite should be related to the crystallography (anisotropy) of the material. According to the first discovers of β-Vit composite, most of the β phase dendrites have a bcc structure with a lattice parameter of 3.5 Å [57]. However, there is no further information about the orientation about the crystallite arrangement and orientation. Also, there is no direct evidence to show that the arc melted monolithic crystallite material has the same crystallography as the crystalline dendrites formed *in-situ* in the β-Vit composite. If crystal orientation does exist, either in the monolithic crystallites or in the *in-situ* dendrites, which might also be different in the two forms, it is also very difficult to control the growth of the orientation with current material processing techniques and prepare the specimens accordingly. It is reasonable to assume that the *in-situ* formed crystalline dendrites reach microscopic isotropy in the composite due to the variance of crystal orientations (if they exist) at the local level. Therefore, for simplicity reasons, both the monolithic crystallites and the *in-situ* dendrites are treated as isotropic materials, and the crystallographic effect on the mechanical properties is not included in this investigation, though it would be a natural topic for future studies.

Figure 4.4 shows the true stress-strain relations from tests done performed three different temperatures, namely, at room temperature, at $613K$, and at $643K$, and with the same strain rate of $2.5\times10^{-4}s^{-1}$.

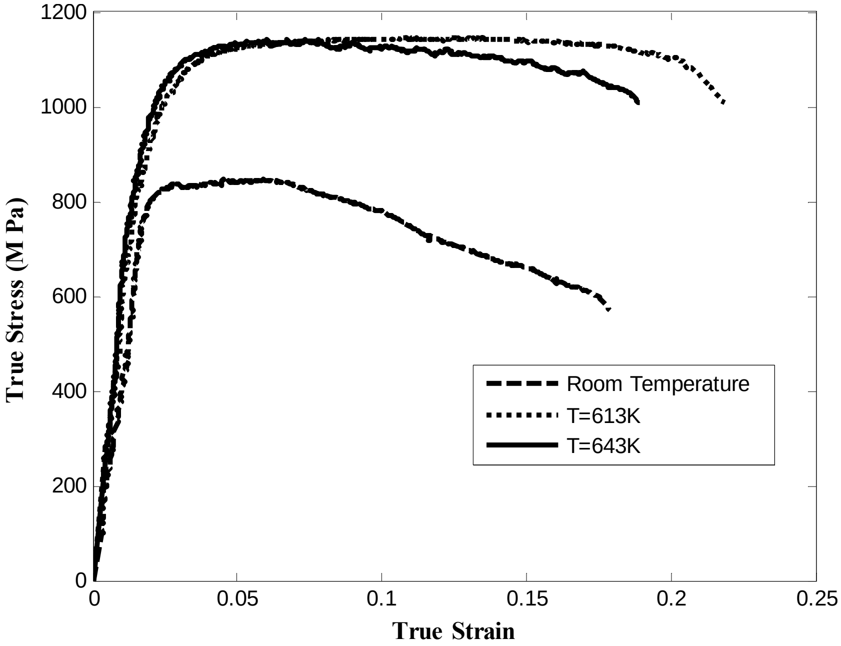

Fig. 4.4 Compressive stress-strain response of the monolithic β-phase crystallite, all tests are performed at the strain rate of $\dot{\varepsilon} = 2.5\times10^{-4} s^{-1}$ and at different temperatures.

It is worth noting that the flow stress of the monolithic crystallite in the supercooled liquid regime is almost one third higher than its value at the room temperature. Also, the room temperature stress-strain curve showed a clear trend of softening. These features may be explained by phase stabilization during the heating and loading processes. At room temperature, the dominant elements Zr and Ti in the β-Vit1 composite ($Zr_{56.3}Ti_{13.8}Cu_{6.9}Ni_{5.6}Be_{12.5}Nb_{5.0}$, at. %) are in hcp (α) phases, which evolve towards bcc (β) phase when the temperature increases to above 800°C (862°C for Zr and 890°C for Ti) and stabilize at β phase until melting [58]. The presence of the element Nb in the dendrite, which is in its bcc phase at room temperature, stabilizes the bcc phase of the *in-situ* dendrite in a metastable state at room temperature. Studies on the monolithic crystallite also showed that the bcc phase would undergo phase strengthening and decomposition with different high temperature treatment (heating temperatures: $573K$ and $973K$, heating time: 3 hours to 18 hours) [51]. Therefore, the hardening of the monolithic crystallite material tested in the supercooled liquid regime could be attributed to the stabilization of stronger bcc phases at high temperature. It is also evident that within the temperature range of 613~643 K, the stress-strain relations of the monolithic crystallite are almost the same when the tests are conducted at the same strain rate, with small variation that might come from the slight difference in the percentage of the bcc phase at different temperatures. All the specimens tested at a low strain rate ($\dot{\varepsilon} = 2.5\times10^{-4}s^{-1}$) started to localize at about 18%~20% of true strain, and they all failed by shear localization along 45^0 relative to the loading direction, typical of polycrystalline metal alloys. The finding of the softening and shear localization behavior of the monolithic β-phase crystallite justifies the previous argument of the shear band formation in the β-Vit1 composite. The existence of the soft and ductile (compared to the glass at room temperature) bcc phase facilitates the initiation and arrest of multiple shear bands, thus enhancing the overall ductility of the composite as compared to that of the amorphous alloy [16, 27].

The compression tests were performed also at the strain rate of $\dot{\varepsilon} = 1\times10^{-3}s^{-1}$, which is the highest stain rate at which the composite was deformed (see Fig.4.3). The true stress-strain curves of the monolithic crystallite tested at $\dot{\varepsilon} = 1\times10^{-3}s^{-1}$, and temperatures of $613K$ and $643K$ are shown in Fig. 4.5. Contrary to the stress-strain curves shown in Fig. 4.4, in which the specimens tested at $613K$ and $643K$ exhibited almost identical response under a constant strain rate of $\dot{\varepsilon} = 2.5\times10^{-4}s^{-1}$, the crystallite tested at $\dot{\varepsilon} = 1.0\times10^{-3}s^{-1}$ shows distinctly different behavior. While the specimens tested at $643K$ deform plastically with slight hardening, the specimens tested at $613K$ soften similar to the specimens tested at room temperature with the strain rate of $\dot{\varepsilon} = 2.5\times10^{-4}s^{-1}$ (see Figs. 4.4 and 4.5 for comparison). Also, it is worth noting that the specimens tested at the higher strain rate ($\dot{\varepsilon} = 1.0\times10^{-3}s^{-1}$) have extended ductility (>50% before the specimen fails) as compared to that of the specimens tested at lower strain rate ($\dot{\varepsilon} = 2.5\times10^{-4}s^{-1}$) (~20% before the specimen fails), regardless of the testing temperature. The specimens tested at high strain rate also showed lower strength as compared to those tested at lower strain rate (see Fig. 4.4 and Fig. 4.5). This discrepancy can also be explained in terms of the phase stabilization and transformation occurring in the monolithic crystalline material during heating. When the specimens were tested at a higher strain rate ($\dot{\varepsilon} = 1.0 \times 10^{-3} s^{-1}$), the total testing time was about 20 times shorter than that of those tested at $\dot{\varepsilon} = 2.5 \times 10^{-4} s^{-1}$. Hence, the strong and brittle bcc phases have less time to be stabilized and the material exhibited a softer and more ductile behavior as compared to those tested at a lower strain rate and for longer time. When the testing temperature is higher (643 *K*), the time required for stabilizing the bcc phase is shorter than that at 613 *K*, therefore the stress-strain curve of the specimen tested at 643 *K* and $1 \times 10^{-3} s^{-1}$ behaved more stable than the one tested at 613 *K* and $1 \times 10^{-3} s^{-1}$ (Fig. 4.5).

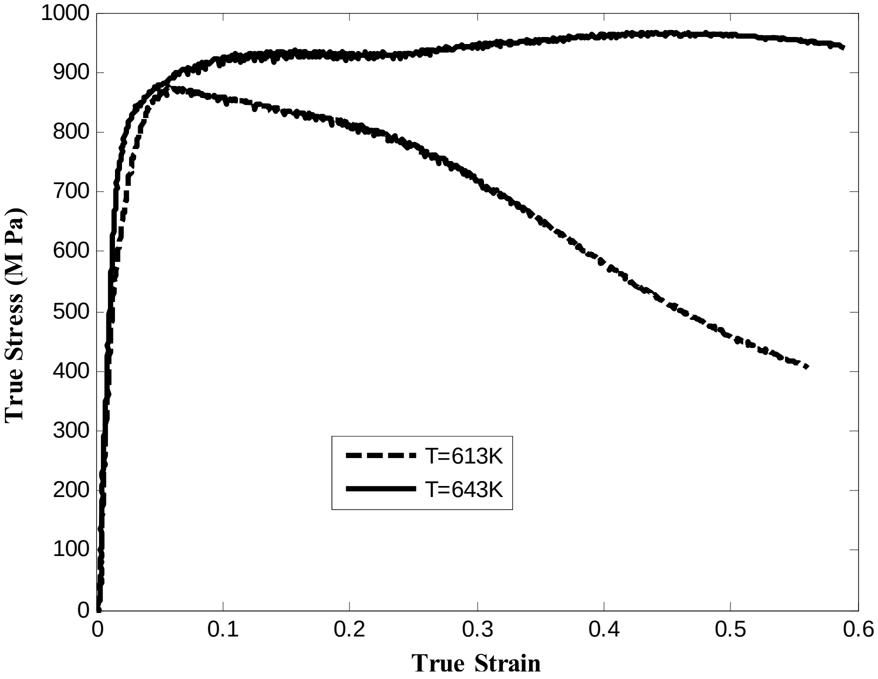

Fig. 4.5 Compressive stress-strain response of the monolithic β-phase crystallite at a strain rate of $\dot{\varepsilon} = 1.0 \times 10^{-3} s^{-1}$ and at different temperatures, 613 *K* and 643 *K*.

4.3.3 Morphological study

To understand the mechanism of strain hardening exhibited during the high temperature compression of β-Vit composite and to simulate the overall stress-strain behavior of the composite material, three key issues need to be resolved prior to further investigation. They are,

(i) the volume fraction of the secondary β-phase dendrites in the composite; (ii) the morphology of the dendrites; and (iii) the size of the dendrites. Microprobe analysis was conducted on the undeformed β-Vit composite material to quantify the chemical compositions of the matrix and the dendrite (inclusion), which rendered the volume fraction of each part. Scanning electron microscopic (SEM) examination with a back scattered electron detector was conducted on undeformed and selected deformed specimens to obtain the micrographs for computing the distribution and the morphology of the dendrites in the composite.

A LEO 1550VP field emission scanning electron microscope (SEM) in the Geological & Planetary Sciences Division of Caltech was used for the microstructural examination. A Robinson back-scatter detector was used to image not only the geometrical features but also the phase contrast in composites. The backscattered images of the distribution of the secondary crystalline phase in the glassy matrix were thus obtained.

Two cylindrical specimens deformed at T=613 $K, \dot{\varepsilon} = 2.2\times10^{-4} s^{-1}$ (Newtonian flow) and T=643 K, $\dot{\varepsilon} = 2.5\times10^{-4} s^{-1}$ (strain hardening flow) were cut at the center along their length and parallel to the loading faces along the direction perpendicular to the loading axis. The section of the specimens was polished with diamond paste with particle size down to $1\ \mu m$, and then examined with SEM. The as-received material was also examined before any deformation, which revealed a homogeneous dendrite pattern (Fig. 4.6). The white areas are the crystalline dendrites, and the dark areas represent regions of the amorphous matrix. The color contrast in the SEM images was revealed by the chemical contrast activated by the electron back scattering.

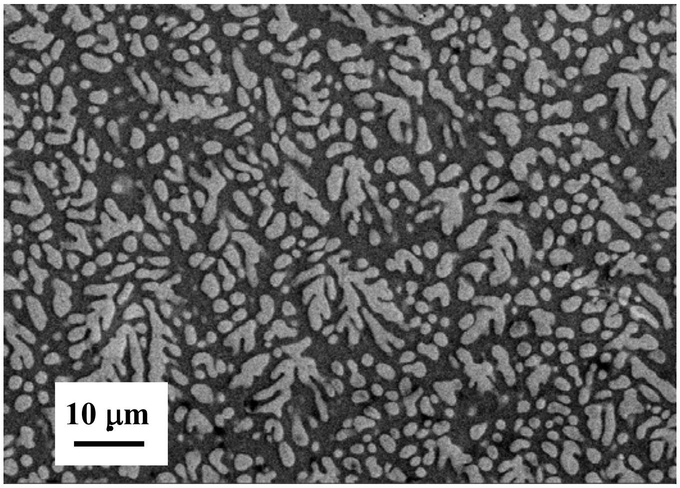

Fig. 4.6 SEM micrograph of the as-received β-Vit composite. The white regions are the Zr-Ni-Ti rich crystalline (bcc) dendritic phase and the black regions are the glassy matrix.

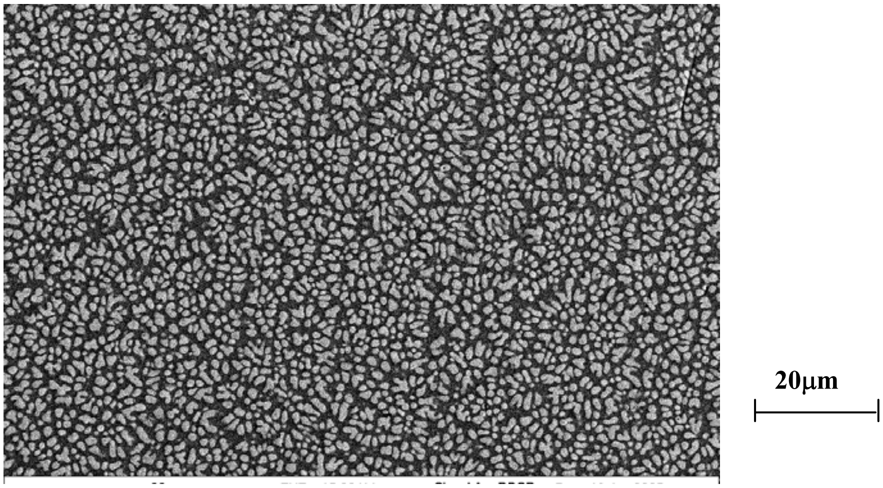

(a)

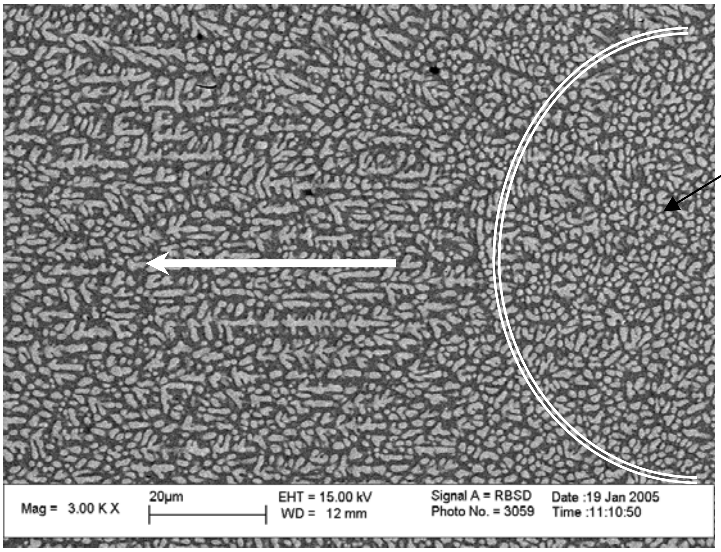

(b)

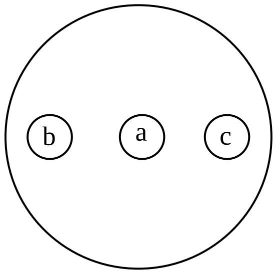

The positions of the SEM images
(a), (b) and (c) on the cross section

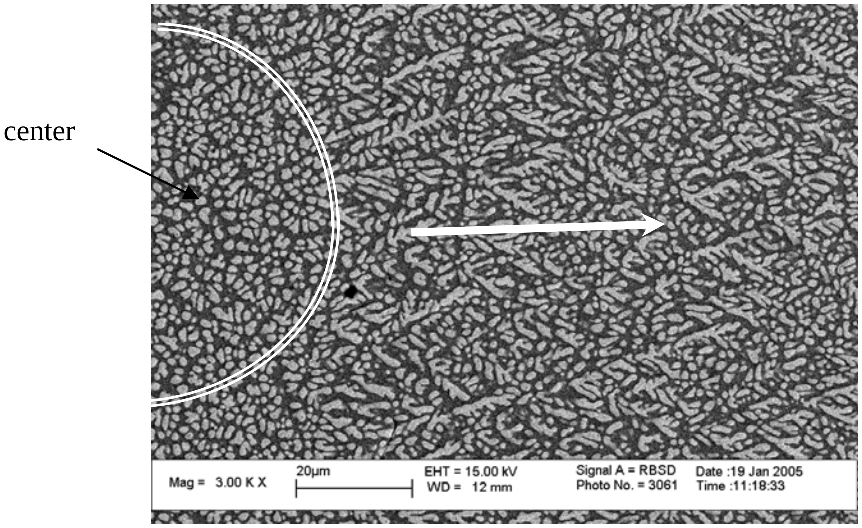

(c)

Fig. 4.7 SEM micrographs of a specimen deformed at T=613 K, $\dot{\varepsilon} = 2.2\times10^{-4} s^{-1}$ in the Newtonian flow mode. The images (a), (b), (c) were taken at the center, left, and right side of the center in the cross section perpendicular to the loading axis. The dendrites show the radial flow from the center to the periphery of the specimen.

The dendrite distribution pattern in the deformed specimens revealed considerable differences in terms of the dendrite size and distribution pattern. In the Newtonian flow specimen deformed at T=613 K, $\dot{\varepsilon} = 2.2 \times 10^{-4} s^{-1}$ (stress-strain curve shown in Fig. 4.3(a)), the dendrites were in the size range of $1 \sim 2\ \mu m$ (Fig. 4.7). Micrographs of different spots in the cross sectional area were taken and inhomogeneity in distribution and shape of the dendrites was observed at these different locations. Figure 4.7 (a) shows the center part of the cross-section of the deformed specimen. The dendrites appear like small particles spherical in shape and are distributed in a homogenous manner. Figures 4.7 (b) and 4.7 (c) are images of regions that are to the left and right hand side of the center, respectively. From these two images, one could see a clear flow of dendrites along rays from the center to the periphery. The small rounded dendrites at the center have linked together to form a "tree structure" in the direction of flow.

A similar flow pattern was found in images taken from the cross section of the specimen deformed at $T = 643\,K$ and $\dot{\varepsilon} = 0.07 s^{-1}$. From the stress-strain curve (Fig. 4.3(d)), one could see that this specimen underwent non-Newtonian homogeneous flow. The specimen was cut along 45^o to the loading axis, which is the maximum shear direction. Figure 4.8 shows the images of the deformed specimen at the upper (Fig. 4.8 (a)) and lower (Fig. 4.8(b)) side of the cut surface of the specimen. The "upper" and "lower" are defined to correspond to the shearing direction. Once again, the dendrites were found to line up in forming vertical rays along the flow direction. Differences in dendrites patterns in the specimens undergoing Newtonian and non-Newtonian flows were not quite evident. However, the Newtonian specimen (Fig. 4.7) showed more structured flow patterns than the non-Newtonian specimen (Fig. 4.8).

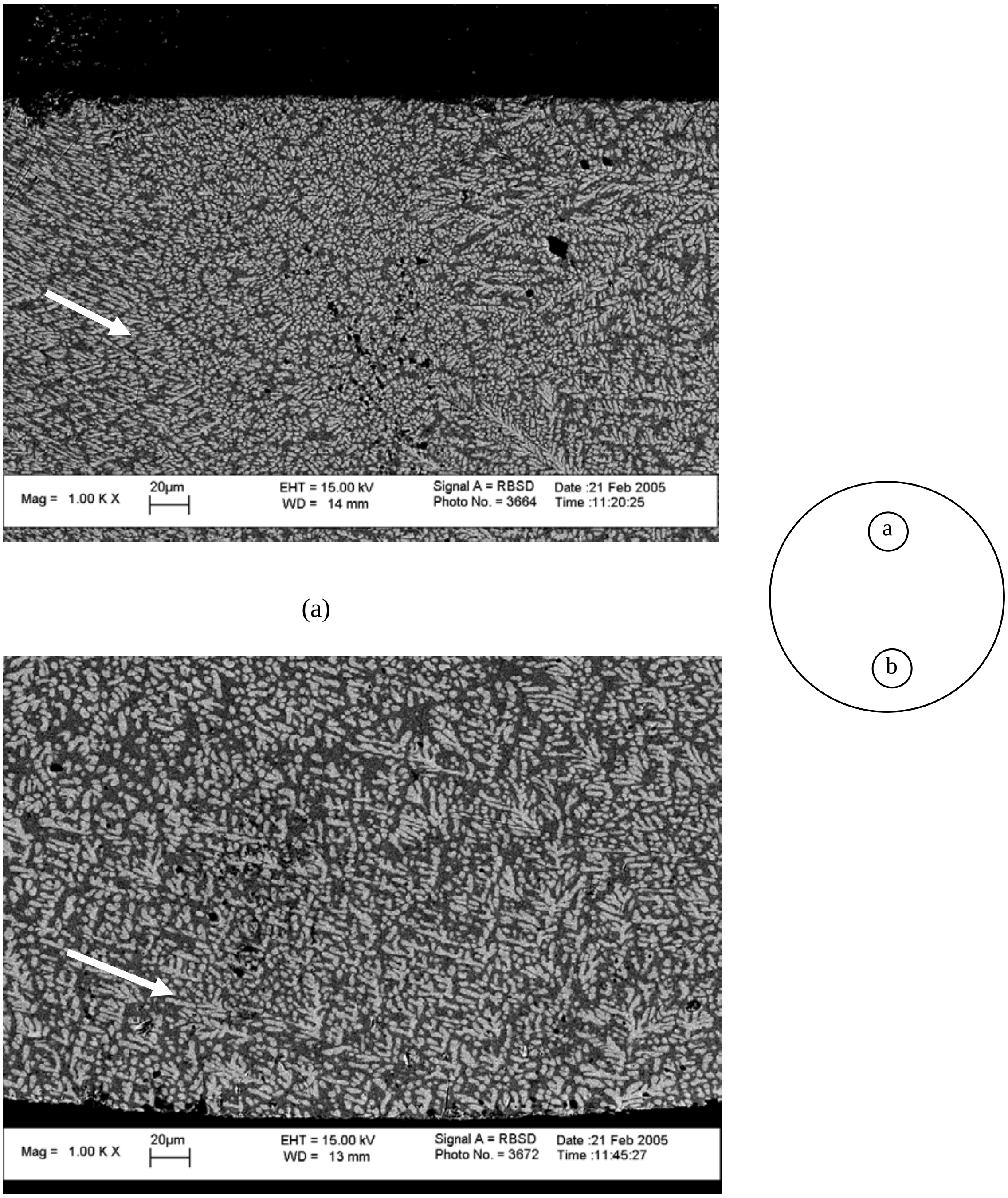

(a)

(b)

Fig. 4.8 SEM images of a section cut at 45^0 to the loading axis in a specimen tested at $T = 643K$, $\dot{\varepsilon} = 0.07s^{-1}$, which underwent non-Newtonian flow: (a) upper corner; (b) lower corner. The directions of the dendrite alignment are labeled with white arrows in the figures.

A specimen deformed at high temperature and low strain rate ($T = 643\,K$, $\dot{\varepsilon} = 2.5\times10^{-4}s^{-1}$) that exhibited material hardening (Fig. 4.3(d)) was examined on a section perpendicular to the loading axis. There was no clear radial flow of the dendrites as had been observed in the specimens deformed in the Newtonian and the non Newtonian flow regimes. Severe inhomogeneity in the dendrite sizes was observed, with the sizes ranging from 2-3 microns (Fig.4.9 (a)) to 20-30 microns (Fig. 4.9 (b)) distributed along different areas of the cross section. The size and distribution did not show any correlation with the location or loading direction. The SEM examination of the as-received material showed a relatively uniform distribution in size and shape of the dendrites over the entire cross section (Fig. 4.6). The dendrite size variation was not observed in other β-Vit specimens deformed with Newtonian and non-Newtonian flow (Figs. 4.7 and 4.8).

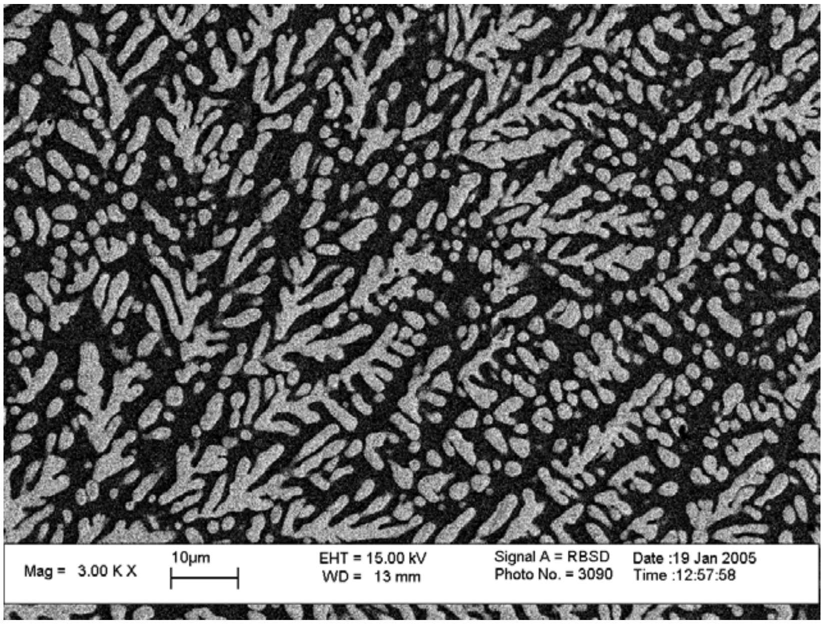

(a)

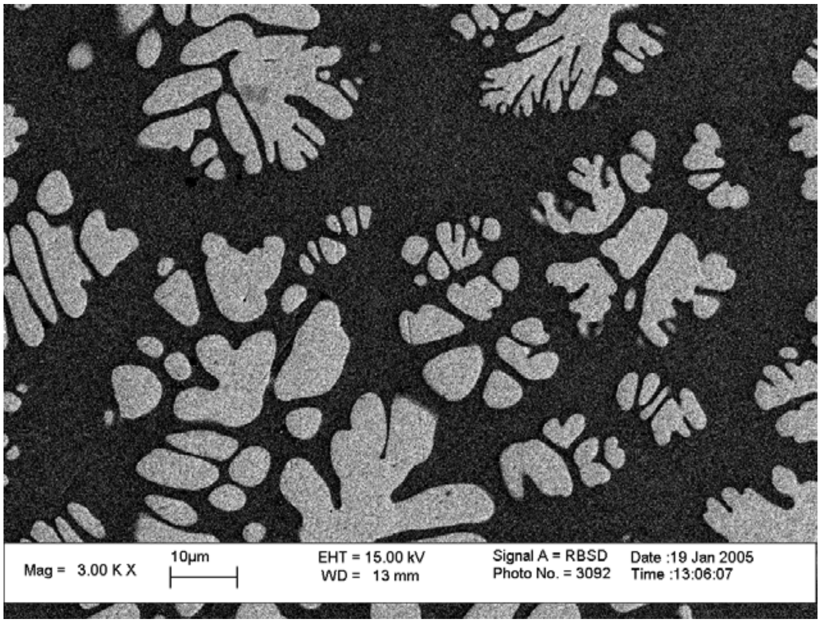

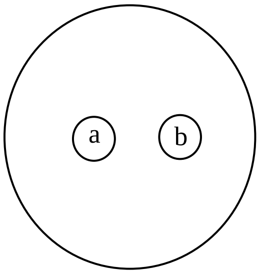

(b)

Fig. 4.9 SEM images of the specimen tested at $T = 643K$ and $\dot{\varepsilon} = 2.5\times10^{-4} s^{-1}$, which underwent hardening deformation. (a) and (b), both shown at the same image scale, were taken at two random locations on the cross section and they showed high inhomogeneity in the dendrites size and distribution.

To understand how the dendrite size inhomogeneity occurred during high temperature ($T = 643K$) and low strain rate ($\dot{\varepsilon} = 2.5\times10^{-4} s^{-1}$) deformation, a set of control experiments were performed in which the specimens were heated to $643K$ and held at the temperature for different lengths of time which equaled the time periods when 0.1, 0.2, and 0.5 of strain occurred during the compressive loading at $643K$. Evidence was found that in the specimen held at $643K$ for $2400 s$, the duration of heating for the specimen shown in Fig. 4.9 and corresponding to 0.5 of strain, small dendrites started to coalesce with each other and grow into bigger ones (see Fig. 4.10). This was not observed in other control specimens with shorter heating time and the as-received sample, though all of them were cut from the same ingot of material, and some even shared common interfaces. Hence, it is reasonable to assume that the growth in size of the dendrites is associated with high temperature and a relatively long duration of the deformation due to low strain rate. Whether such coalescence of dendrites was responsible for the observed hardening behavior is explored further through numerical simulations in section 4.5.

From the foregoing results and characterization of the β phase monolithic crystallite, one can see that the nature of deformation and microstructural evolution during thermomechanical loading is complex. Further detailed investigations are needed to address these and other issues including the anisotropy of the crystallite and their relationship with the *in-situ* dendrites in the composite. Of particular interest would be the examination of the crystallography and crystal stability of the monolithic β-phase as a function of temperature and time.

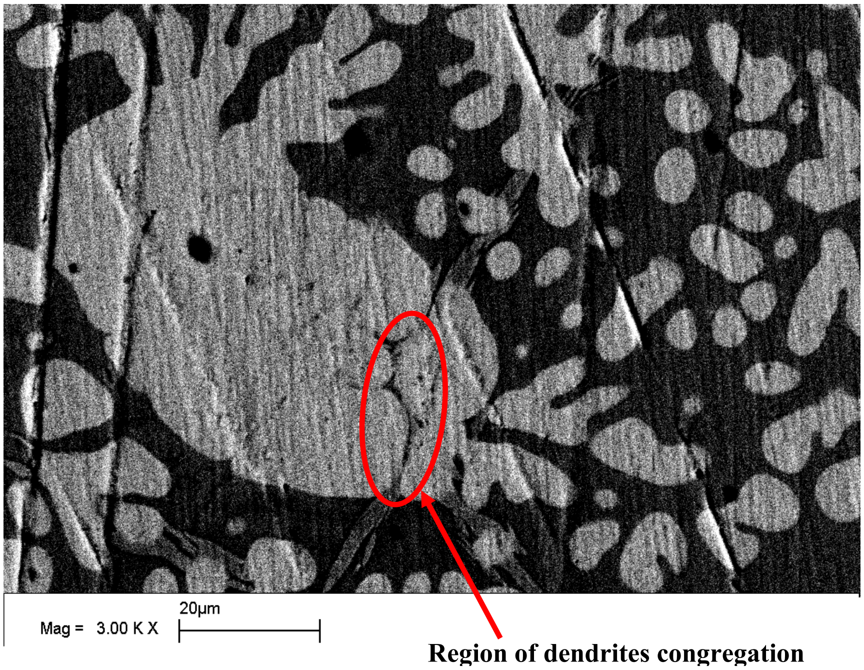

Region of dendrites congregation

Fig. 4.10 SEM image of the undeformed specimen heated at $T = 643K$ for 2400 seconds which had the same thermal history as the specimen whose stress-strain response is shown in Fig. 4.9. Dendrite coalescence (circled in red) was observed and could account for the inhomogeneity in the dendrite size in Fig. 4.9.

4.4Analysis

4.4.1 Strain rate sensitivity of β-Vit in its supercooled liquid regime

The deformation of viscoplastic materials can be characterized using a power relation between the flow stress and strain rate, which is generally expressed by [59]

$$\sigma = B\dot{\varepsilon}^{m} , \tag{4.1}$$

where B is a constant which incorporates the dependence on temperature and material characteristics, m is termed as the strain rate sensitivity coefficient $\left(m = \frac{\partial \ln \sigma}{\partial \ln \dot{\varepsilon}} \right)$, i.e., the slope of stress vs. strain rate curve in a logarithmic scale.

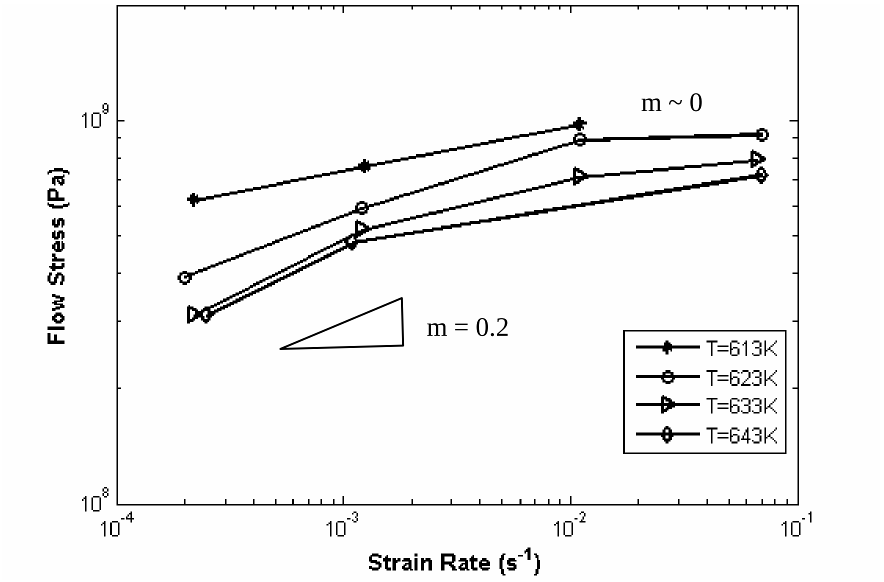

Fig. 4.11 Flow stress dependence of β-Vit composite on strain rate at temperatures T=613K, 623K, 633K, and 643K.

The dependence of the flow stress of β-Vit composite on the strain rate was analyzed and plotted in Fig. 4.11. Because no clear steady state flow stresses for the strain hardening mode at low strain rate and high temperature would be identified, so the stresses at 0.2 of the true strain were taken as “flow stress” and plotted against various strain rates. The strain rate sensitivity coefficient m is almost zero in the inhomogeneous flow region and is around 0.2 in the homogeneous flow region.

The shear viscosities of the flow were computed from one third of the flow stress over strain rate for uniaxial compressive loading [59]. Therefore, the viscosity dependence on the strain rate at various temperatures in the supercooled region can be computed for the composite. The viscosities are plotted in Fig. 4.12. Unlike the common feature in metallic glasses deformed in their supercooled regions, the viscosity dependence on strain rate does not differ much from each other at different temperatures in the supercooled liquid regime of the β-Vit1 composite. The insert in Fig. 4.12 shows the viscosity data of Vit 1 from Lu *et al.* [5]. At relatively higher temperatures in the supercooled region, the viscosity-strain rate curve flattens out to the Newtonian viscosity regime with decreasing strain rate. Such a feature is observed in the viscosity studies on Vit 4 (Fig. 3.8) and other BMGs [22, 53]. The β-Vit composite does not show the same high temperature sensitivity of shear viscosity (Fig. 4.12), probably due to the existence of ~25% volume fraction of the crystalline dendrites which are not as sensitive to the temperature as the glass in the supercooled liquid region.

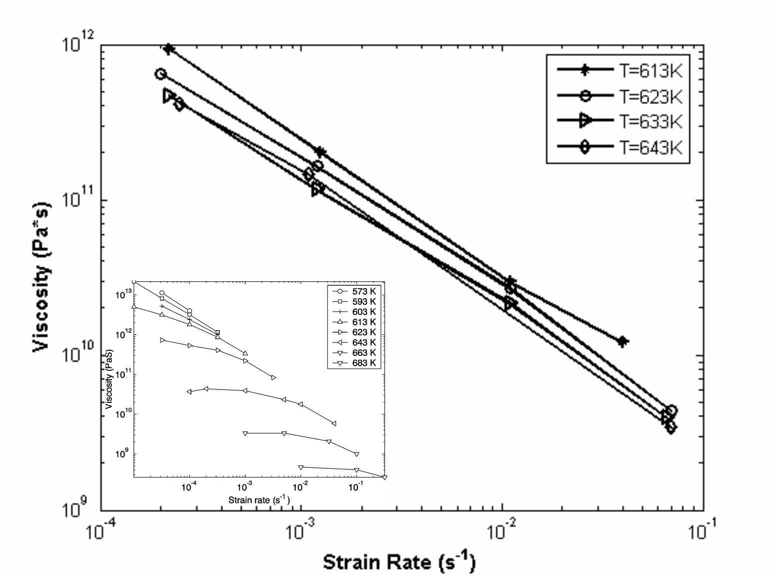

Fig. 4.12 Viscosity dependence of β-Vit on strain rate at temperatures of T=613 *K*, 623 *K*, 633 *K* and 643 *K*. The insert shows that of Vit 1 glass [5] which features flattening at high temperature and low strain rate corresponding to the Newtonian flow, which is not present in the composite in the temperature and strain rate regime explored here.

4.5 Computational Modeling

4.5.1 Micromechanical model

The micromechanical model of the β-Vit composite can be described with a unit cell model with a set of geometric features and material characteristics. The geometric features include the particle volume fraction, particle shape, and distribution. The material characteristics include the constitutive relations of both phases under various temperature and strain rate conditions, and the matrix/dendrite interface behavior. In this investigation, the focus is on the simplified case of the deformation of uniform, well-aligned, and perfectly bonded crystalline dendrites in an amorphous matrix, to simulate the hardening behavior of the composite specimen at high temperature ($643K$) and low strain rate ($\dot{\varepsilon} = 2.5 \times 10^{-4} s^{-1}$). The influences of the particle volume fraction and dendrite distribution are also studied. The constitutive relations of the two phases are given in section 4.5.2.

Different unit cell models can be adopted to simulate composite material with various microstructures. For example, a stacked hexagonal array was used to simulate an axisymetric cell structure [38]. Structures like body-centered tetragonal array of particles and body-centered cubic array of particles were also simulated with proper unit cell geometries and boundary conditions [61].

All numerical simulations were carried out with using commercial finite element software ABAQUS [62]. In the current study, three-dimensional unit cells with various shapes of inclusions were used in the finite element analysis. A unit cell with rectangular parallelepiped inclusion of volume fraction 24.5% is shown in Fig. 4.13. The inclusion is chosen to be in rectangular shape for convenience in simulations.

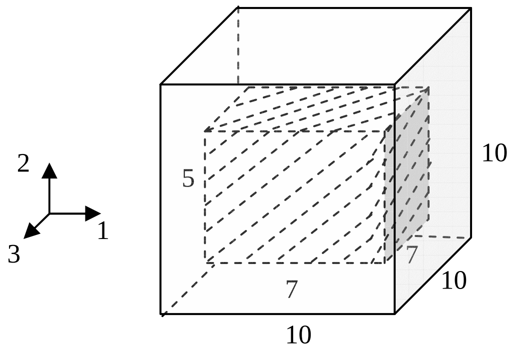

Fig. 4.13 A typical composite unit cell for FEM simulation (24.5% volume fraction of rectangular parallelepiped dendrites), scales are given to show the relative sizes of the cell and the particle.

The periodic boundary condition is widely used for numerical simulation of deformation of composite material to save computational time. Periodic boundary conditions expressed in terms of macroscopic strain tensor $\underline{\underline{\varepsilon}}$ are applied to the unit cell. A prescribed normal strain ε_{22} is applied as a displacement loading to simulate the compressive deformation of the entire cell, which satisfies the kinematic periodic boundary conditions and stress equilibrium. For the detailed description of periodic boundary conditions applied on the unit cell and their implementation in the finite element setting, the reader is referred to Appendix A.

The principle of virtual work is used to calculate the macroscopic mechanical response of the unit cell. A dummy node that is not attached to any elements is introduced in constraint equations along with the boundary node sets. For a given constraint equation, the reaction force at each node is proportional to its respective coefficient. Therefore, the reaction forces at the boundary nodes can be obtained with knowing the generalized reaction forces at the dummy node. The implementation of the dummy node to introduce the deformation and to obtain the macroscopic constraint force is delineated in the ABAQUS user manual [62]. The details of these calculations are also given in Appendix A.

4.5.2 Material Modeling

Since the focus of the numerical simulation is to understand the effect of dendrite inclusion on the hardening behavior of the composite deformed at high temperatures, a simple deformation plasticity model was used for both the dendrite and the matrix that accounts for their deformation behavior in the experiments at certain temperature and strain rate, even though a more comprehensive viscoplastic/viscoelastic constitutive models for the amorphous matrix and the crystallite are desirable.

The Ramberg-Osgood relation for the power law hardening materials is [38]:

$$\frac{\varepsilon}{\varepsilon_o} = \frac{\sigma}{\sigma_o} + \alpha\left(\frac{\sigma}{\sigma_o}\right)^n \quad ,(4.2)$$

where n is the stress exponent, $\varepsilon_0 = \sigma_0 / E$ is the yield strain, E is the Young's modulus, and α is a material parameter. For a certain temperature and strain rate, both the behavior of the dendrite and the metallic glass can be fit with the Ramberg-Osgood relation as an empirical model.

The experimental results of Vit 1, the monolithic crystallite, and the β-Vit composite, all deformed at 643K and $2.5\times10^{-4}s^{-1}$, and the corresponding model fits according to Ramberg-Osgood relation (Eq. (4.2)) are shown in Fig. 4.14. It should be noted that the composition of the matrix part of the β-Vit composite ($Zr_{45.7}Ti_{12}Nb_{2.5}Cu_{9.5}Ni_{8.14}Be_{22.1}$) is not exactly the same as that of Vit 1 ($Zr_{41.25}Ti_{13.75}Cu_{12.5}Ni_{10}Be_{22.5}$) but is close enough for a good reference since no data of the glass made out of the exact matrix composition are available. The fitting parameters for Vit 1 tested at 643K and $2.5\times10^{-4}s^{-1}$ were found as $n = 16.43$ and $\alpha = 0.56$, with $\sigma_0 = 30MPa$ and $\varepsilon_0 = 0.01$. For the monolithic bcc β-phase dendrite, $n = 24.07$ and $\alpha = 0.22$, with $\sigma_0 = 1000MPa$ and $\varepsilon_0 = 0.018$. The Poison's ratio for both the materials are taken to be 0.36 [52].

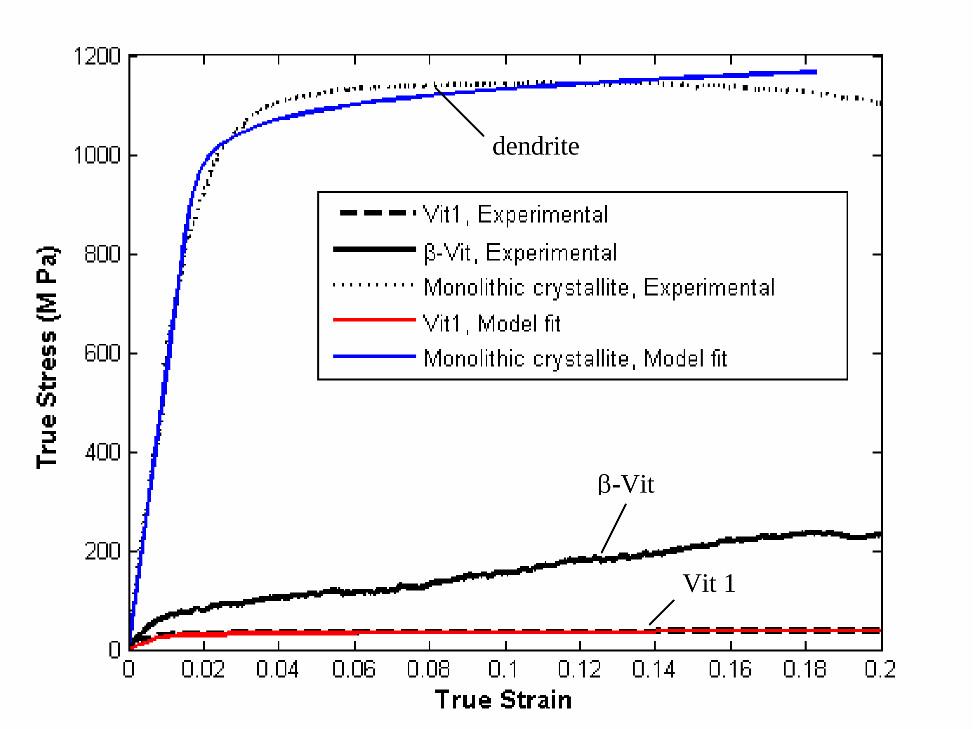

Fig. 4.14 True stress-strain relations of Vit 1, monolithic dendrite and β-Vit1 composite in uniaxial compression at temperature, T=643K and strain rate, $\dot{\varepsilon} = 2.5 \times 10^{-4} s^{-1}$.

The two empirical material models with Ramberg-Osgood relation were incorporated in ABAQUS/Standard [63] to simulate the macroscopic composite response. The interfaces between the two phases were assumed to be perfectly bonded. The implemented computational model is discussed in Appendix A, and the results are presented in the following section.

4.5.3 Results and discussion

The stress-strain relations computed with the model in Appendix A with a block of dendrite in the center of the unit cell (center-inclusion) and different volume fractions of the inclusion are plotted in Fig. 4.15. Models with three different volume fraction were computed (16%, 24.5%, and 39.2%), and the one with 24.5% volume fraction of inclusion reproduced the experimental result fairly well. This supports the claim of Hays *et al.* [16] that the volume fraction of the dendrites in the β-Vit composite is 25%, rather than Lee's statement that it is 40% [52].

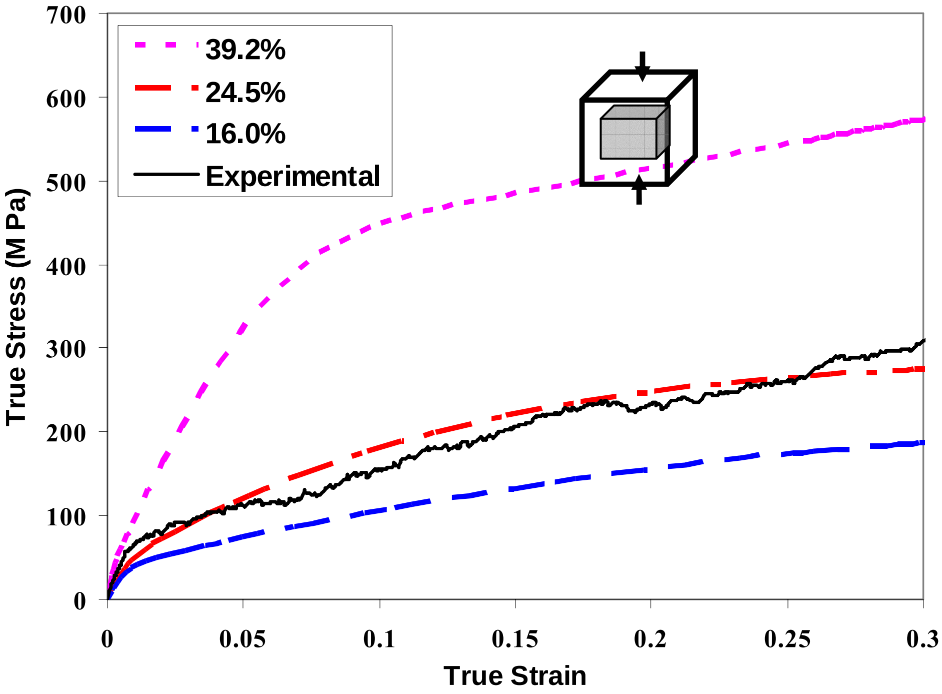

Fig. 4.15 True stress-strain relations of models with volume fractions of 16%, 24.5% and 39.2%, compared to the result from uniaxial compression of β-Vit composite at temperature, T=643K and strain rate, $\dot{\varepsilon} = 2.5\times10^{-4}s^{-1}$.

To study the effect of the inclusion shape and size on the overall composite behavior, few other cell models with the same dendrite volume fraction of 24.5% but containing dendrites in different shapes were considered. Figure 4.16 shows the three different models that were considered. In (a), the 24.5% volume fraction of dendrite is in a single rectangular block located at the center of the cell, while in (b), the same volume fraction of dendrites are distributed in 8 small blocks with the dimension of each about half of the dimension of the dendrite in (a). The dendrite in model (c) is in a tree-like shape, which is closest to the dendrite pattern in the as-received β-Vit composite. Upon compressive loading, their stress-strain curves are plotted in Fig. 4.17.

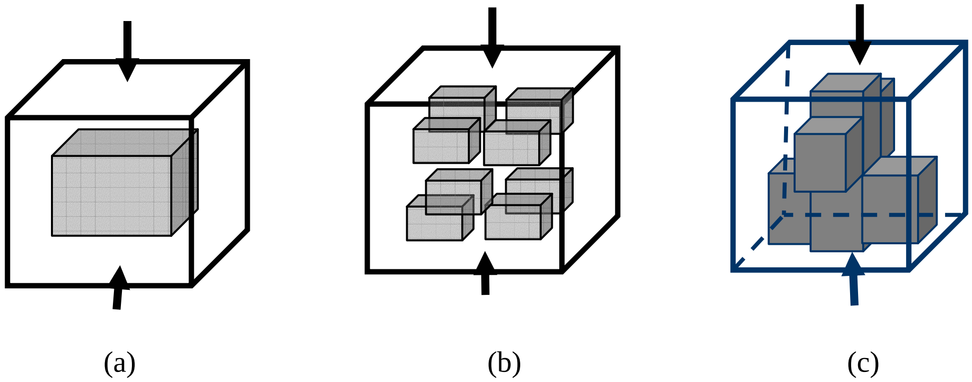

Fig. 4.16 Model of computational unit cells with different dendrite sizes and shapes. (a) a single rectangular inclusion at the center of the unit cell; (b) 8 smaller distributed rectangular inclusions and (c) a tree shape inclusion. The volume fraction of inclusions in each unit cell is 24.5%.

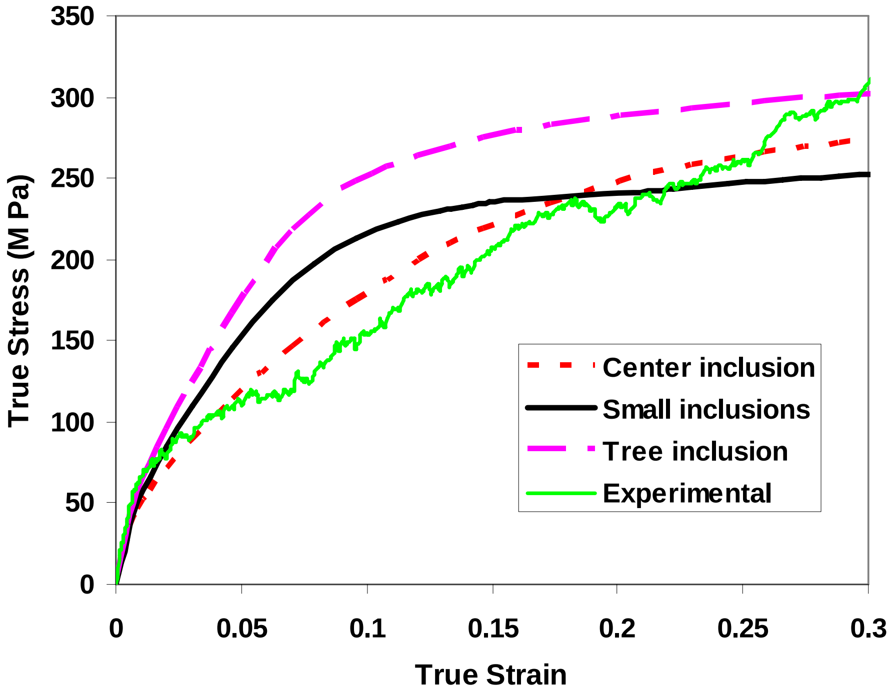

Fig. 4.17 True stress-strain relations of models containing the same volume fraction (24.5%) but different sizes and shapes of dendrites. The red dotted line corresponds to the unit cell in Fig. 4.16 (a), the black solid line corresponds to the unit cell in Fig. 4.16 (b), and the pink dash line corresponds to the unit cell in Fig. 4.16 (c).

Figure 4.17 shows the stress-strain relations computed from the three unit cells described above. Comparing the results of the two rectangular inclusion models (red dotted line and black solid line), it shows that the unit cell with bigger dendrite has slightly higher flow strength, which is consistent with the previous observation of β-Vit specimen with larger dendrites showing more evidence of strain hardening than those with smaller dendrites (Figs. 4.3(d) and 4.9). Figure 4.18 also shows that the unit cell with smaller and more evenly distributed dendrites can undergo more stable deformation as compared to the one with big and centered dendrite. The latter localizes at about 0.35 of true strain. The small and uniform dendrites pattern was found to be present in the β-Vit1 specimens in Newtonian and non-Newtonian flow modes (Figs. 4.7 and 4.8) and possibly accounts for the steady and stable flow without undergoing hardening.

The stress-strain curve obtained from the tree-shape model (Fig. 4.16(c)) is shown as a pink dashed line in Fig. 4.17. The tree-shape microstructure exhibits obvious advantages to the center-block structure in terms of both flow strength and stability. If the processing temperature and cooling condition are both optimized, the *in-situ* formed crystalline phase in the β-Vit composite has a natural tendency to form the tree-shape structure (Fig. 4.6). Under certain favorable thermal and mechanical loading conditions, the dendrites even align with each other to obtain higher strength and more stability (Fig. 4.7). When the tree structure is broken due to dendrites coalescence or splitting (Fig. 4.9(a) and (b)), the composite tends to lose the steady-state flow and begin to exhibit hardening behavior.

4.6 Conclusions

The deformation behavior of β-Vit composite was studied in uniaxial compression at high temperatures (within the supercooled liquid regime of the glassy matrix) and various strain rates, followed by microstructural characterization and numerical simulation on a simplified dual-phase composite unit cell. The conclusions from this study are summarized below:

(i)The β-Vit composite exhibits extended plasticity at high temperature similar to its glassy matrix. Newtonian and non-Newtonian flow modes of deformation were observed during the high temperature deformation. Another distinct flow mode in the homogeneous flow region, the strain hardening mode, was discovered during uniaxial compression tests performed on the composite at very low strain rate and high temperature.

(ii)The morphologies of the specimens that underwent Newtonian flow, non-Newtonian flow, and strain hardening flow were examined in a scanning electron microscope. Uniform small size dendrites were found in the Newtonian and non-Newtonian specimens. In the Newtonian specimen, the dendrites showed a tendency to align and link with each other to form a tree or a chain structure along the deforming direction, which was not quite evident in the specimen that underwent non-Newtonian flow. The dendrites in the strain hardening specimen showed high inhomogeneity in their size and distribution. Some dendrites were more than ten times larger than the smaller dendrites in the specimen and those in the as-received material. A set of control specimens were prepared by heating them for the same amount of time corresponding to 0.1, 0.2, and 0.5 of true strain during the high temperature compressive loading. It was found that with longer heating time, some dendrites had the tendency to coalesce and form inclusions with larger size.

(iii) From the stress-strain behaviors of the monolithic bcc crystallites and the amorphous matrix material (analogous to Vit 1), it is suspected that the transition from non-hardening to hardening in deformation of the composite happens when the flow strength of the amorphous matrix changes dramatically with the strain rate and temperature change in the supercooled liquid region, while the strength of the crystalline dendrite phase remains more or less at the same level despite small changes brought about by the bcc phase stabilization and phase transformation. Therefore, the dual-phase composite transitions from hard-matrix-soft-inclusion type at room temperature to soft-matrix-hard-inclusion type with increasing temperature and decreasing strain rate.

(iv) Numerical simulations of deformation of the composite were performed on simplified models of unit cells with inclusions of various shapes and sizes. The effects of volume fraction, dendrite size and dendrite distribution on the overall composite behavior were studied. The simulations revealed the following noteworthy results which were in agreement with the experimental observations: (a) dendrites in larger size contribute to increases in the composite strength, but also make the material more prone to localization during compression; (b) small and uniform dendrites, as observed in the specimens that underwent Newtonian or non-Newtonian flow, help the composite to achieve a more stable plastic flow; and (b) a tree-shape dendrite structure, similar to that in the as-received β-Vit composite material, is superior to granular dendrites in terms of both flow strength and stable deformation.

Appendix A.Periodic boundary conditions for uniaxial compression on a unit cell

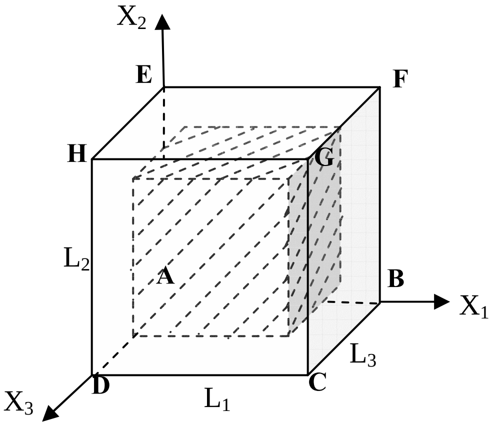

Fig. 4A-1 Model of a unit cell with inclusion

For a unit cell shown in Fig. 4A-1, the boundary displacements can be related to the macroscopic deformation gradient $\underline{\underline{F}}$.

Each pair of parallel surfaces is constrained with three equations. For example, the displacements of the surface AEHD and those of the surface BFGC have the relations as follows:

$$\begin{aligned}
u_1|_{BFGC} &= u_1|_{AEHD} + (F_{11}-1)\times L_1 \\
u_2|_{BFGC} &= u_2|_{AEHD} + F_{12}\times L_1 \quad \text{(4A-1)} \\
u_3|_{BFGC} &= u_3|_{AEHD} + F_{13}\times L_1 .
\end{aligned}$$

Similar equations are applied to surfaces ABFE and DCGH, surfaces ABCD and EFGH to obtain 9 equations in total.

If the edges are included every time when a pair of surfaces is applied with three equations, each edge will be constrained with six equations. Therefore, the edges are applied with the constraints independently. For example, the displacements of edge HG can be constrained with those of edge AB:

$$u_1|_{HG} = u_1|_{AB} + F_{12}\times L_1$$

$$\begin{aligned} u_2\,|_{HG} &= u_2\,|_{AB} + (F_{22}-1)\times L_2 \,. \quad \text{(4A-2)} \\ u_3\,|_{HG} &= u_3\,|_{AB} + (F_{33}-1)\times L_3 \end{aligned}$$

Any pair of parallel edges can be put together to construct the constraints. From the twelve edges in three parallel sets, there are 27 equations to constrain the boundary conditions.

Similarly, to avoid over-constraints, the vertices can not be included in the equations for the edges. For example, the displacements of vertex G have the relation with those of vertex A as follows:

$$\begin{aligned} u_1\,|_{G} &= u_1\,|_{A} + (F_{11}-1)\times L_1 \\ u_2\,|_{G} &= u_2\,|_{A} + (F_{22}-1)\times L_2 \quad \text{(4A-3)} \\ u_3\,|_{G} &= u_3\,|_{A} + (F_{33}-1)\times L_3 \end{aligned}$$

There are 21 equations in total obtained from the eight vertices.

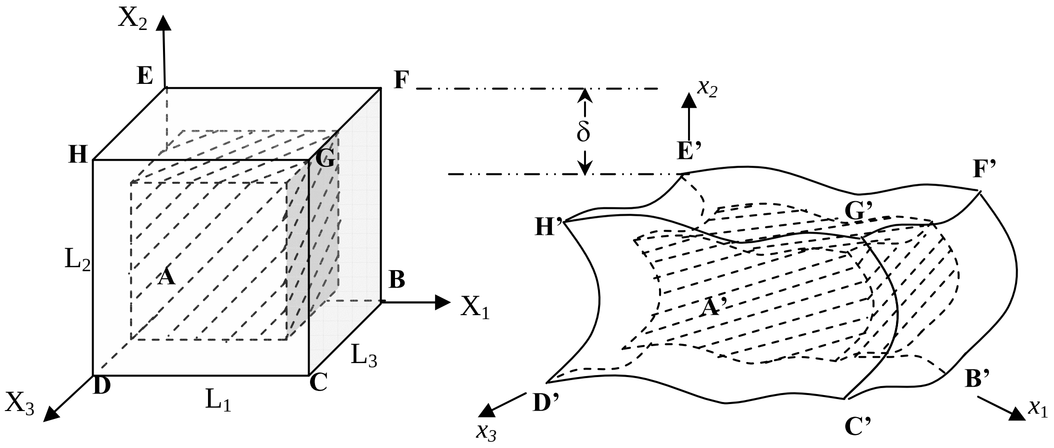

Fig. 4A-2 Unit cell under uniaxial compression of δ, with scale exaggerated.

Now, if a uniaxial compression with displacement control loading is considered, as shown in Fig. 4A-2, the deformation gradient can be written as

$$\underline{\underline{F}} = \begin{bmatrix} 1+\nu_1\dfrac{\delta}{L_1} & 0 & 0 \\ 0 & 1-\dfrac{\delta}{L_2} & 0 \\ 0 & 0 & 1+\nu_3\dfrac{\delta}{L_3} \end{bmatrix}, \text{(4A-4)}$$

where $-\dfrac{\delta}{L_2}$ is associated with macroscopic strain tensor component ε_{22}. ν_1 and ν_3 are Poisson's ratios along different orthogonal directions in the material. For the isotropic unit cell model, $L_1 = L_2 = L_3$ and $\nu_1 = \nu_2 = \nu$. Therefore, Eqs. (4A-1)-(4A-3) can be simplified as:

$$\begin{aligned} &u_1\,|_{BFGC} - u_1\,|_{AEHD} - \nu\delta = 0 \\ &u_1\,|_{BFGC} - u_1\,|_{AEHD} = 0 \quad \text{(4A-1)'} \\ &u_1\,|_{BFGC} - u_1\,|_{AEHD} = 0 \end{aligned}$$

$$\begin{aligned} &u_1\,|_{HG} - u_1\,|_{AB} = 0 \\ &u_2\,|_{HG} - u_2\,|_{AB} + \delta = 0 \quad \text{(4A-2)'} \\ &u_3\,|_{HG} - u_3\,|_{AB} - \nu\delta = 0 \end{aligned}$$

$$\begin{aligned} &u_1\,|_{G} - u_1\,|_{B} - \nu\delta = 0 \\ &u_2\,|_{G} - u_2\,|_{A} + \delta = 0 \quad \text{(4A-3)'} \\ &u_3\,|_{G} - u_3\,|_{A} - \nu\delta = 0 \end{aligned}$$

Equations (4A-1)'-(4A-3)' can be directly implemented in ABAQUS in the form of a set of homogeneous and inhomogeneous constraint equations. All the edges and surfaces can be represented with sets of discrete nodes. The inhomogeneous term can be implemented by introducing a dummy node Z which is not attached to any elements in the model and has a pre-defined displacement in the x_2 direction: $u_2\,|_Z = -\delta$. Therefore, each of the equations above denotes N equations in terms of nodal displacements, with N being the total nodal number in the node set. For example, the first equation in (4A-2)' can be rewritten as

$$u_1|_{P_i} - u_1|_{Q_i} - u_1|_Z = 0\,, \quad \text{(4A-5)}$$

where Z denotes the dummy node, P_i denotes any node on the surface BFGC, Q_i denotes the node on the surface AEHD and is at the opposite position of P_i, i.e., $X_2(Q_i) = X_2(P_i)$, $X_3(Q_i) = X_3(P_i)$, $X_1(P_i) = X_1(Q_i) + L_1$, and i is from 1 to N, the total number of nodes on one surface (not including the edges and the vertices).

The linear constraint generates constraint forces at all degrees of freedom involved in the equation. According to the principle of virtual work [63, 64], for a given constraint equation these forces are proportional to their respective coefficients. Again, taking Eq. (4A-5) as an example, which gives

$$\begin{aligned} f_1^{Pi} &= f_1^{Z} \\ f_1^{Qi} &= -f_1^{Z}\,, \end{aligned} \qquad \text{(4A-6)}$$

where f_1^{Z} is the X_1 component of the constraint force at the dummy node Z and f_1^{Pi} and f_1^{Qi} are the X_1 components of the constraint forces at P_i and Q_i, respectively. The total reaction force on surface BFGC equals the sum of the constraint forces at all the surface nodes (including interior nodes and nodes at the edges and vertices) and can be computed as:

$$\begin{aligned} F_1^{BFGC} &= \sum_i f_1^{Pi} = (N + M + O) f_1^{Z} \\ F_2^{BFGC} &= \sum_i f_2^{Pi} = 0 \quad \text{(4A-7)} \\ F_3^{BFGC} &= \sum_i f_3^{Pi} = 0\,, \end{aligned}$$

where i is node index, which covers all the interior nodes (N) , edges (M), and vertices (O) of surface BFGC. Similarly, the reaction force on the top surface EFGH can be obtained as:

$$F_1^{EFGH} = \sum_i f_1^{Ri} = 0$$
$$F_2^{EFGH} = \sum_i f_2^{Ri} = (N' + M' + O')\, f_2^Z \quad (4A\text{-}7)$$
$$F_3^{EFGH} = \sum_i f_3^{Ri} = 0 .$$

The macroscopic compressional engineering (nominal) stress and strain (in the reference configuration) of the unit cell can be computed on an average basis:

$$E_{22} = d_2 / L_2$$
$$\zeta_{22} = F_2^{EFGH} / (L_1 \times L_3) . \ (4A\text{-}8)$$

In addition, the true stress and strain (in the deformed configuration) are computed accordingly:

$$\varepsilon_{22} = -\ln(1 - E_{22})$$
$$\sigma_{22} = \zeta_{22}(1 - \varepsilon_{22}) . \ (4A\text{-}9)$$

With displacement control loading condition, F_2^{EFGH} is the output result of the simulation. The average stress and strain are computed according to (4A-9) and can be compared with experimental results.

References

[1] A. Peker and W. L. Johnson, "A Highly Processable Metallic-Glass - $Zr_{41.2}Ti_{13.8}Cu_{12.5}Ni_{10.0}Be_{22.5}$," *Applied Physics Letters*, **63**, 2342-2344 (1993).

[2] A. Inoue, T. Nakamura, N. Nishiyama, and T. Masumoto, "Mg-Cu-Y Bulk Amorphous-Alloys with High-Tensile Strength Produced by a High-Pressure Die-Casting Method," *Materials Transactions Jim*, **33**, 937-945 (1992).

[3] H. A. Bruck, T. Christman, A. J. Rosakis, and W. L. Johnson, "Quasi-Static Constitutive Behavior of $Zr_{41.2}Ti_{13.8}Cu_{12.5}Ni_{10.0}Be_{22.5}$ Bulk Amorphous-Alloys," *Scripta Metallurgica Et Materialia*, **30**, 429-434 (1994).

[4] H. A. Bruck, A. J. Rosakis, and W. L. Johnson, "The dynamic compressive behavior of beryllium bearing bulk metallic glasses," *Journal of Materials Research*, **11**, 503-511 (1996).

[5] J. Lu, G. Ravichandran, and W. L. Johnson, "Deformation behavior of the $Zr_{41.2}Ti_{13.8}Cu_{12.5}Ni_{10.0}Be_{22.5}$ bulk metallic glass over a wide range of strain-rates and temperatures," *Acta Materialia*, **51**, 3429-3443 (2003).

[6] Y. Kawamura, T. Shibata, A. Inoue, and T. Masumoto, "Deformation behavior of $Zr_{65}Al_{10}Ni_{10}Cu_{15}$ glassy alloy with wide supercooled liquid region," *Applied Physics Letters*, **69**, 1208-1210 (1996).

[7] B. van Aken, P. de Hey, and J. Sietsma, "Structural relaxation and plastic flow in amorphous $La_{50}Al_{25}Ni_{25}$," *Materials Science and Engineering a-Structural Materials Properties Microstructure and Processing*, **278**, 247-254 (2000).

[8] D. Lee, "Localized Vs Homogeneous Deformation in $Fe_{82}B_{15}Si_3$ Amorphous Alloy," *Metallurgical Transactions a-Physical Metallurgy and Materials Science*, **12**, 419-424 (1981).

[9] R. Vaidyanathan, M. Dao, G. Ravichandran, and S. Suresh, "Study of mechanical deformation in bulk metallic glass through instrumented indentation," *Acta materialia*, **49**, 3781-3789 (2001).

[10] Z. Bian, G. Chen, G. He, and X. Hui, "Microstructure and ductile-brittle transition of as-cast Zr-based bulk glass alloys under compressive testing," *Materials science & engineering. A, Structural materials*, **316**, 135-144 (2001).

[11] P. Lowhaphandu, S. L. Montgomery, and J. J. Lewandowski, "Effects of superimposed hydrostatic pressure on flow and fracture of a Zr-Ti-Ni-Cu-Be bulk amorphous alloy," *Scripta materialia*, **41**, 19-24 (1999).

[12] J. Lu and G. Ravichandran, "Pressure-dependent flow behavior of $Zr_{41.2}Ti_{13.8}Cu_{12.5}Ni_{10.0}Be_{22.5}$ bulk metallic glass," *Journal of materials research*, **18**, 2039-2049 (2003).

[13] J. Schroers and W. L. Johnson, "Ductile bulk metallic glass," *Physical Review Letters*, **93**, 255506 (2004).

[14] J. C. Lee, Y. C. Kim, J. P. Ahn, and H. S. Kim, "Enhanced plasticity in a bulk amorphous matrix composite: macroscopic and microscopic viewpoint studies," *Acta Materialia*, **53**, 129-139 (2005).

[15] G. He, W. Loser, J. Eckert, and L. Schultz, "Enhanced plasticity in a Ti-based bulk metallic glass-forming alloy by in situ formation of a composite microstructure," *Journal of Materials Research*, **17**, 3015-3018 (2002).

[16] C. C. Hays, C. P. Kim, and W. L. Johnson, "Microstructure controlled shear band pattern formation and enhanced plasticity of bulk metallic glasses containing in situ formed ductile phase dendrite dispersions," *Physical Review Letters*, **84**, 2901-2904 (2000).

[17] H. Ma, J. Xu, and E. Ma, "Mg-based bulk metallic glass composites with plasticity and high strength," *Applied Physics Letters*, **83**, 2793-2795 (2003).

[18] R. U. Vaidya and K. N. Subramanian, "Metallic-Glass Ribbon-Reinforced Glass-Ceramic Matrix Composites," *Journal of Materials Science*, **25**, 3291-3296 (1990).

[19] R. U. Vaidya and K. N. Subramanian, "Toughening in Metallic-Glass Ribbon Reinforced Glass-Ceramic Matrix Composites," *Sampe Journal*, **29**, 26-30 (1993).

[20] S. J. Cytron, "A Metallic Glass-Metal Matrix Composite," *Journal of Materials Science Letters*, **1**, 211-213 (1982).

[21] P. G. Zielinski and D. G. Ast, "Preparation of Rapidly Solidified Ribbons with 2nd Phase Particles," *Journal of Materials Science Letters*, **2**, 495-498 (1983).

[22] H. Kato, T. Hirano, A. Matsuo, Y. Kawamura, and A. Inoue, "High strength and good ductility of $Zr_{55}Al_{10}Ni_5Cu_{30}$ bulk glass containing ZRC particles," *Scripta Materialia*, **43**, 503-507 (2000).

[23] C. P. Kim, R. Busch, A. Masuhr, H. Choi-Yim, and W. L. Johnson, "Processing of carbon-fiber-reinforced $Zr_{41.2}Ti_{13.8}Cu_{12.5}Ni_{10.0}Be_{22.5}$ bulk metallic glass composites," *Applied Physics Letters*, **79**, 1456-1458 (2001).

[24] H. Choi-Yim, R. D. Conner, F. Szuecs, and W. L. Johnson, "Processing, microstructure and properties of ductile metal particulate reinforced $Zr_{57}Nb_5Al_{10}Cu_{15.4}Ni_{12.6}$ bulk metallic glass composites," *Acta Materialia*, **50**, 2737-2745 (2002).

[25] H. Choi-Yim, R. Busch, U. Koster, and W. L. Johnson, "Synthesis and characterization of particulate reinforced $Zr_{57}Nb_5Al_{10}Cu_{15.4}Ni_{12.6}$ bulk metallic glass composites," *Acta Materialia*, **47**, 2455-2462 (1999).

[26] H. Choi-Yim and W. L. Johnson, "Bulk metallic glass matrix composites," *Applied Physics Letters*, **71**, 3808-3810 (1997).

[27] K. M. Flores, W. L. Johnson, and R. H. Dauskardt, "Fracture and fatigue behavior of a Zr-Ti-Nb ductile phase reinforced bulk metallic glass matrix composite," *Scripta Materialia*, **49**, 1181-1187 (2003).

[28] R. D. Conner, H. Choi-Yim, and W. L. Johnson, "Mechanical properties of $Zr_{57}Nb_5Al_{10}Cu_{15.4}Ni_{12.6}$ metallic glass matrix particulate composites," *Journal of Materials Research*, **14**, 3292-3297 (1999).

[29] J. Das, S. K. Roy, W. Loser, J. Eckert, and L. Schultz, "Novel in situ nanostructure-dendrite composites in Zr-base multicomponent alloy system," *Materials and Manufacturing Processes*, **19**, 423-437 (2004).

[30] C. Fan, C. F. Li, and A. Inoue, "Nanocrystal composites in Zr-Nb-Cu-Al metallic glasses," *Journal of Non-Crystalline Solids*, **270**, 28-33 (2000).

[31] C. C. Hays, C. P. Kim, and W. L. Johnson, "Enhanced plasticity of bulk metallic glasses containing ductile phase dendrite dispersions," *Metastable, Mechanically Alloyed and Nanocrystalline Materials, Pts 1 and 2*, **343-3**, 191-196 (2000).

[32] E. Pekarskaya, C. P. Kim, and W. L. Johnson, "In situ transmission electron microscopy studies of shear bands in a bulk metallic glass based composite," *Journal of Materials Research*, **16**, 2513-2518 (2001).

[33] F. Szuecs, C. P. Kim, and W. L. Johnson, "Mechanical properties of $Zr_{56.2}Ti_{13.8}Nb_{5.0}Cu_{6.9}Ni_{5.6}Be_{12.5}$ ductile phase reinforced bulk metallic glass composite," *Acta Materialia*, **49**, 1507-1513 (2001).

[34] C. C. Hays, C. P. Kim, and W. L. Johnson, "Improved mechanical behavior of bulk metallic glasses containing in situ formed ductile phase dendrite dispersions," *Materials Science and Engineering a-Structural Materials Properties Microstructure and Processing*, **304**, 650-655 (2001).

[35] B. Clausen, S. Y. Lee, E. Ustundag, C. P. Kim, D. W. Brown, and M. A. M. Bourke, "Compressive deformation of in situ formed bulk metallic glass composites," *Scripta Materialia*, **54**, 343-347 (2006).

[36] J. Lu, "Mechanical behavior of a bulk metallic glass and its composite over a wide range of strain rates and temperatures," *Ph. D Thesis*. Pasadena: California Institute of Technology (2002).

[37] J. D. Eshelby, "The Determination of the Elastic Field of an Ellipsoidal Inclusion, and Related Problems," *Proceedings of the Royal Society of London Series a-Mathematical and Physical Sciences*, **241**, 376-396 (1957).

[38] G. Bao, J. W. Hutchinson, and R. M. Mcmeeking, "Particle Reinforcement of Ductile Matrices against Plastic-Flow and Creep," *Acta Metallurgica Et Materialia*, **39**, 1871-1882 (1991).

[39] G. Bao, J. W. Hutchinson, and R. M. Mcmeeking, "The Flow-Stress of Dual-Phase, Non-Hardening Solids," *Mechanics of Materials*, **12**, 85-94 (1991).

[40] L. G. Brinson and W. G. Knauss, "Thermorhologically complex behavior of multiphase viscoelastic materials," *Journal of the Mechanics and Physics of Solids*, **39**, 859-880 (1991).

[41] D. M. Parks, J. A. W. van Dommelen, M. C. Boyce, F. P. T. Baaijens, and W. A. M. Brekelmans, "Micromechanical modeling of finite elasto-visco plastic deformation in semi-crystalline polymers.," *Abstracts of Papers of the American Chemical Society*, **223**, D92 (2002).

[42] N. Sheng, M. C. Boyce, D. M. Parks, G. C. Rutledge, J. I. Abes, and R. E. Cohen, "Multiscale micromechanical modeling of polymer/clay nanocomposites and the effective clay particle," *Polymer*, **45**, 487-506 (2004).

[43] L. Anand and C. Su, "A theory for amorphous viscoplastic materials undergoing finite deformations, with application to metallic glasses," *Journal of the Mechanics and Physics of Solids*, **53**, 1362-1396 (2005).

[44] Q. Yang, A. Mota, and M. Ortitz, "A finite-deformation constitutive model of bulk metallic glass plasticity," *Computational mechanics*, **37**, 194-204 (2006).

[45] W. L. Johnson, J. Lu, and M. D. Demetriou, "Deformation and flow in bulk metallic glasses and deeply undercooled glass forming liquids - a self consistent dynamic free volume model," *Intermetallics*, **10**, 1039-1046 (2002).

[46] R. Huang, Z. Suo, J. H. Prevost, and W. D. Nix, "Inhomogeneous deformation in metallic glasses," *Journal of the Mechanics and Physics of Solids*, **50**, 1011-1027 (2002).

[47] M. L. Falk, J. S. Langer, and L. Pechenik, "Thermal effects in the shear-transformation-zone theory of amorphous plasticity: Comparisons to metallic glass data," *Physical Review E*, **70**, 011507 (2004).

[48] X. Y. Fu, M. L. Falk, and D. A. Rigney, "Sliding behavior of metallic glass - Part II. Computer simulations," *Wear*, **250**, 420-430 (2001).

[49] M. L. Falk and J. S. Langer, "Dynamics of viscoplastic deformation in amorphous solids," *Physical Review E*, **57**, 7192-7205 (1998).

[50] A. C. Lund and C. A. Schuh, "Yield surface of a simulated metallic glass," *Acta Materialia*, **51**, 5399-5411 (2003).

[51] S. Y. Lee, "Deformation Mechanisms of Bulk Metallic Glass Composites," *Ph. D Thesis*, Pasadena: California Institute of Technology (2005).

[52] T. Waniuk, J. Schroers, and W. L. Johnson, "Timescales of crystallization and viscous flow of the bulk glass-forming Zr-Ti-Ni-Cu-Be alloys," *Physical Review B*, **67**, 184203 (2003).

[53] H. Kato, Y. Kawamura, A. Inoue, and H. S. Chen, "Newtonian to non-Newtonian master flow curves of a bulk glass alloy $Pd_{40}Ni_{10}Cu_{30}P_{20}$," *Applied Physics Letters*, **73**, 3665-3667 (1998).

[54] M. Bletry, P. Guyot, Y. Brechet, J. J. Blandin, and J. L. Soubeyroux, "Homogeneous deformation of bulk metallic glasses in the super-cooled liquid state," *Materials Science and Engineering a-Structural Materials Properties Microstructure and Processing*, **387-89**, 1005-1011 (2004).

[55] W. J. Kim, D. S. Ma, and H. G. Jeong, "Superplastic flow in a $Zr_{65}Al_{10}Ni_{10}$Cu15 metallic glass crystallized during deformation in a supercooled liquid region," *Scripta Materialia*, **49**, 1067-1073 (2003).

[56] T. G. Nieh and J. Wadsworth, "Homogeneous deformation of bulk metallic glasses," *Scripta Materialia*, **54**, 387-392 (2006).

[57] C. P. Kim, "Ductile Phase Reinforced Bulk Metallic Glass Composites Formed by Chemical Partitioning," *Ph. D Thesis*. Pasadena, California: California Institute of Technology (2001).

[58] A. I. H. Committee, *ASM handbook*, Vol. 2, 10th ed, (1990).

[59] A. H. Chokshi, A. K. Mukher, and T. G. Langdon, "Superplasticity in Advanced Materials," *Materials science & engineering. R, Reports*, **10**, 237-274 (1993).

[60] G. W. Scherer, *Relaxation in glass and composites*. Malabar: Krieger Publishing (1992).

[61] M. C. Boyce, S. Socrate, and P. G. Llana, "Constitutive model for the finite deformation stress-strain behavior of poly(ethylene terephthalate) above the glass transition," *Polymer*, **41**, 2183-2201 (2000).

[62] ABAQUS, *Reference Manuals, v6.5*. Providence, RI (2004).

[63] M. Danielsson, D. M. Parks, and M. C. Boyce, "Constitutive modeling of porous hyperelastic materials," *Mechanics of Materials*, **36**, 47-358 (2004).

Chapter 5

Summary and Future Work

As one of the best glass forming compositions and most studied amorphous alloys, the Zr-Cu-Ni-Ti-Be family of BMGs (Vitreloy) provided good candidates for both scientific exploration and practical application. This dissertation is based on the experimental studies on two Vitreloy alloys, $Zr_{41.2}Ti_{13.8}Cu_{12.5}Ni_{10}Be_{22.5}$ (Vit 1) and $Zr_{46.7}Ti_{8.3}Cu_{7.5}Ni_{10}Be_{27.5}$ (Vit 4), one of their newly processed variations, $Zr_{47.4}Ti_{8.0}Cu_{7.3}Ni_{9.8}Be_{27.5}$ (Vit 4'), and an *in-situ* composite, $Zr_{56.3}Ti_{13.8}Cu_{6.9}Ni_{5.6}Be_{12.5}Nb_{5.0}$ (β-Vit). The deformation behavior of these materials in their supercooled liquid regions were characterized with high temperature uniaxial compression tests and correlated with the atomic disordering and microstructural change in them using the materials characterization techniques of DSC and SEM.

A comparative study of Vit 1 and Vit 4 was performed by using uniaxial compression tests at a single temperature (643 *K*) in their supercooled liquid regions at various strain rates, followed by DSC examination on the deformed specimens. Constant strain rate tests and following DSC examination revealed different relaxation mechanisms in the two material systems. The DSC trace of Vit 1 features a spinodal phase-separation prior to the primary crystallization event. Mechanical loading increases the extent of the spinodal phase-separation and accelerates it to occur at a lower temperature. This phase-separation is responsible for nucleating nano-crystallites during the low strain rate tests. In Vit 4, no such phase separation is discerned from the DSC traces. Decomposition in the form of local chemical composition fluctuation dominates and has a strong influence on the deformation tests performed at relatively high strain rates. Jump in strain rate tests, in which the strain rate dropped abruptly to Newtonian flow region after reaching a steady state in the non-Newtonian region, were then performed and reconfirmed the difference of the deformation mechanisms in the two materials. While Vit 1 retained its Newtonian flow stress after the strain rate drop, the flow stress of Vit 4 decreased to almost 1/3 as compared to that of the constant strain rate test in the Newtonian region. DSC examination at the glass transition regions of Vit 1 and Vit 4 showed evidence of less free volume decrease in Vit 1, which is expected to help retain the flow strength after the strain rate drop. The activation volumes of the two materials in both their Newtonian and non-Newtonian regions were calculated by multiple jump-in-strain-rate tests independently in the two flow regions. It was discovered that for both materials, the activation volumes of the non-Newtonian flow are much smaller than those of the Newtonian flow, which accounts for the different features of the two flow modes. The multiple jump-in-strain-rate tests also showed that from non-Newtonian to Newtonian flow, the flow strength of Vit 1 decreased in a gradual manner, while sudden drop could be noticed for that of Vit 4, which agreed with the conclusions from previous constant strain rate tests and strain rate drop tests. Though previous studies on the thermodynamical properties on these two alloys have indicated the different thermodynamic and kinetic mechanisms in their relaxation processes [1-5], such differences have not been taken into consideration to account for the effect on the mechanical behavior of the alloys, and it was generally believed that jump in strain rate was considered to have little or no influence on the flow stress of BMGs [6, 7]. This investigation performed mechanical tests on Vit 4 for the first time in its supercooled liquid state, and by a comparative study between Vit 1 and Vit 4, revealed yet another deformation mechanism existing in BMGs.

The deformation and viscosity of a new Vitreloy alloy in the supercooled liquid state, which has a slight composition variation from Vit 4, were characterized using constant strain rate uniaxial compression tests. The so-called Vit 4' alloy is more thermodynamically stable than Vit 1, and also proved to be a stronger alloy than Vit 4 in the supercooled liquid region. A new theoretical model, namely the Cooperative Shear Model (CSM) proposed recently by Johnson and Samwer [8] that correlates evolutions of the macroscopic mechanical/thermal variables such as shear modulus and viscosity with the inner states and configurations of atom clusters in amorphous alloys, was critically examined in this investigation. Both the non-Newtonian and Newtonian viscosities of Vit 4' could be modeled with the CSM. The shear moduli of deformed specimens measured directly with an ultrasonic technique and deduced from the measured shear viscosities using CSM were in good agreement with each other. The theory of CSM provides coherent explanation that links the mechanical properties of amorphous alloys with their microstructure at the atomic scale. This is the first work that has validated the applicability of CSM to bulk metallic glasses from the mechanical deformation perspective. It is recommended that further detailed study of the mechanical properties, *in-situ* study of atomic disordering and their correlation to CSM in BMGs be undertaken.

The flow behavior of β-Vit composite in the supercooled liquid region of the matrix glass was characterized in a systematic manner for the first time. A distinct flow mode other than Newtonian and non-Newtonian flow in the homogeneous flow region, the strain hardening mode, was discovered during uniaxial compression tests performed on the composite at very low strain rate and high temperature. The transition from non-hardening to hardening in deformation of the composite happens when the flow strength of the amorphous matrix changes dramatically with the strain rate and temperature change in the supercooled liquid region, while the strength of the crystalline dendrite phase remains more or less at the same level despite small changes brought about by the bcc phase stabilization and phase transformation. Therefore, the dual-phase composite transitions from hard-matrix-soft-inclusion type at room temperature to soft-matrix-hard-inclusion type with increasing temperature and decreasing strain rate. To quantitatively explain the hardening mechanism, the microstructural morphologies of the as-received, deformed, and annealed composite were studied and the volume fraction, size, and pattern of the distribution of the crystalline dendrites were obtained in each different scenario. It was discovered that the dendrites are smaller and more uniform in the specimens that underwent Newtonian and non-Newtonian flow, unlike those that underwent strain hardening flow in which the dendrites have a large variation in size at different regions of the specimen. The effects of dendrite volume fraction, size, and distribution were investigated with finite element numerical simulation of a unit cell model with periodic boundary conditions implemented in commercial finite element software, ABAQUS/Standard. A volume fraction of ~24.5% dendrites could model the stress-strain behavior of the hardening flow at high temperature and low strain rate in a satisfactory manner. The simulations revealed the following noteworthy results which were in agreement with the experimental observations: (i) dendrites in larger size contribute to an increase in the composite strength but also make the material more prone to localization during compression; (ii) small and uniform dendrites, as observed in the specimens that underwent Newtonian or non-Newtonian flow, help the composite achieve a more stable plastic flow and; also, (iii) a tree-shape dendrite structure, similar to that in the as-received β-Vit composite material, is superior to granular dendrites in terms of both flow strength and stable deformation. Even though the numerical model for the composite is rather elementary, with empirical material models at a certain temperature and strain rate and without considering the viscoelastic properties of the matrix and fully exploring the deformation behavior of the dendrite, it provided significant insight in understanding the hardening mechanism of the composite, and provided useful insights for designing and processing new composite materials with enhanced mechanical performance. The results discovered by high temperature compression tests on the β-Vit composite also revealed further structural benefit from the crystalline dendrite: at room temperature, it serves as a soft and ductile inclusion to enhance the ductility of the metallic glass, and at high temperature, it serves as a hard inclusion that helps in retaining the strength of the glass. This could lead future research in studying various aspects of metallic glass composites such as the dendrite crystallography, evolution of microstructures, and relevant mechanical response. Also, it is recommended that a complete simulation model for the composite that incorporates realistic geometries of the dendrite and user defined viscoplastic/viscoelastic) material models for the dendrite and the glassy matrix that are applicable over a wide range of strain rate and temperature.

References

[1] T. Waniuk, J. Schroers, and W. L. Johnson, "Timescales of crystallization and viscous flow of the bulk glass-forming Zr-Ti-Ni-Cu-Be alloys," *Physical Review B*, **67**, 184203, (2003).

[2] R. Busch, S. Schneider, A. Peker, and W. L. Johnson, "Decomposition and Primary Crystallization in Undercooled $Zr_{41.2}Ti_{13.8}Cu_{12.5}Ni_{10.0}Be_{22.5}$ Melts," *Applied Physics Letters*, **67**, 1544-1546 (1995).

[3] R. Busch, Y. J. Kim, and W. L. Johnson, "Thermodynamics and Kinetics of the Undercooled Liquid and the Glass-Transition of the $Zr_{41.2}Ti_{13.8}Cu_{12.5}Ni_{10.0}Be_{22.5}$ Alloy," *Journal of Applied Physics*, 77, 4039-4043 (1995).

[4] R. Busch, E. Bakke, and W. L. Johnson, "Viscosity of the supercooled liquid and relaxation at the glass transition of the $Zr_{46.75}Ti_{8.25}Cu_{7.5}Ni_{10}Be_{27.5}$ bulk metallic glass forming alloy," *Acta Materialia*, **46**, 4725-4732 (1998).

[5] E. Bakke, R. Busch, and W. L. Johnson, "The Viscosity of the $Zr_{46.75}Ti_{8.25}Cu_{7.5}Ni_{10}Be_{27.5}$ Bulk Metallic-Glass Forming Alloy in the Supercooled Liquid," *Applied Physics Letters*, **67**, 3260-3262 (1995).

[6] J. Lu, G. Ravichandran, and W. L. Johnson, "Deformation behavior of the $Zr_{41.2}Ti_{13.8}Cu_{12.5}Ni_{10.0}Be_{22.5}$ bulk metallic glass over a wide range of strain-rates and temperatures," *Acta Materialia*, **51**, 3429-3443 (2003).

[7] M. Heggen, F. Spaepen, and M. Feuerbacher, "Creation and annihilation of free volume during homogeneous flow of a metallic glass," *Journal of Applied Physics*, **97**, 033506 (2005).

[8] W. L. Johnson and K. Samwer, "A universal criterion for plastic yielding of metallic glasses with a $(T/T\text{-}g)^{(2/3)}$ temperature dependence," *Physical Review Letters*, **95**, 195501 (2005).